Performance of a new single sideband (SSB) continuous phase modulation (CPM)

Karim Kasan

DOCTORAT BRETAGNE LOIRE / MATHSTIC

CentraleSupélec

THÈSE DE DOCTORAT DE

CENTRALESUPÉLEC

ÉCOLE DOCTORALE N° 601
Mathématiques et Sciences et Technologies de l'Information et de la Communication
Spécialité : *«Télécommunication »*

Par

« Karim Kassan »

« Performance of a new single sideband (SSB) continuous phase modulation (CPM) »

Thèse présentée et soutenue à Rennes, le 6 décembre 2021
Unité de recherche : « UMR 6164 - IETR (Équipe SCEE)»
Thèse N° : « 2021CSUP0010 »

Rapporteurs avant soutenance :

FERRE Guillaume	Maître de Conférences, ENSEIRB-MATMECA, Laboratoire IMS (Bordeaux)
BOUCHERET Marie-Laure	Professeur des Universités, ENSEEIHT (Toulouse)

Composition du Jury :

Président :	AMIS Karine	Professeur, IMT-A, Laboratoire LabSTICC (Brest)
Examinateurs :	ROVIRAS Daniel	Professeur des Universités, CNAM (Paris)
	MANNONI Valérian	Ingénieur de Recherche, CEA LETI (Grenoble)
Dir. de thèse :	LOUËT Yves	Professeur de CentraleSupélec, Laboratoire IETR (Rennes)
Encadrants :	FARES Haïfa	Maître de Conférences, CentraleSupélec, Laboratoire IETR (Rennes)
	GLATTLI Christian	Directeur de Recherche, CEA Université Paris Saclay (Saclay)

Acknowledgement

First and foremost, I want to express my gratitude to my thesis director, Yves LOUËT, and my supervisors, Haifa FARES and Christian GLATTLI, for their invaluable assistance over the years. Without their tremendous support, patience, and motivating attitude toward their students, none of this would have been possible.
Thanks to everyone on the SCEE team for spending three years with me, particularly: Bassel, Amor, Georgios, Carlos, Rubin, Ali C, Rami, Hussein, Majed, Youssef, Yorgoss, Muhammad, Muhammad A, Muhammad Y, Jacques, Bastien, Rémi, Lilian, Esteban, Sami, Jeremy, Paul.
Finally, I would like to express my most profound appreciation to my parents: my mom **Rima** and my father **Nazih**, my brothers and sisters: Zeina, Sarah, Fouad, Abdallah, and my friends particularly: Alaa B, Abdallah, Omar, Maaruf, Baraa, Alaa A, for their encouragement and support.

Abstract

In this PhD thesis, we investigate the single-sideband frequency shift keying (SSB-FSK), a continuous phase modulation (CPM) scheme having, by essence, the original feature of the single-sideband (SSB) spectrum. First, we present the origin of the signal from quantum physics. Then, we propose a new simplified Maximum likelihood sequence detection (MLSD) detector for conventional CPM schemes based on the rearrangement shown in the SSB-FSK signal model. To fully exploit the SSB-FSK performance, we examine the signal error probability, bandwidth occupancy, and receiver complexity. Since different performance metrics are considered, we employed a multi-objective optimization to achieve new SSB-FSK schemes that outperform conventional CPM schemes. Moreover, we propose a solution to simplify the complexity of SSB-FSK signals using the pulse amplitude modulation (PAM) decomposition. The PAM pulses were achieved from an algorithm we developed. Furthermore, we offer an optimum generic training sequence for the joint estimation of symbol timing, frequency offset, and carrier phase for burst mode synchronization. The training sequence was obtained using the Cramér-Rao bounds.

Resumé des Travaux de Thèse

La communication est l'une des nécessités les plus fondamentales dès l'antiquité, et elle a considérablement progressé dès la fin du 18ième siècle avec le premier réseau de télécommunications codées d'envergure nationale avec le Télégraphe de Chappe. En raison du besoin croissant de communication de données, et parce que la transmission numérique offre des choix de traitement de données et une flexibilité non disponibles avec la transmission analogique, les systèmes de communications numériques sont devenus incontournables. Nous présentons ci-dessous certains des facteurs qui ont conduit à la révolution des communications numériques [13] :

- Les circuits numériques sont plus fiables et moins coûteux à fabriquer que les circuits analogiques.
- La technologie numérique permet une plus grande flexibilité dans la mise en œuvre que le matériel analogique.
- Les méthodes numériques sont bien adaptées aux fonctions de traitement du signal telles que la protection contre les interférences et le brouillage, ainsi que le cryptage et l'authentification.
- La numérisation d'images, de sons ou de documents, permet une duplication parfaite, car basée sur des signaux discrets autorisant détection et correction d'erreurs, ce que ne permet pas un signal analogique qui est un signal continu toujours entaché de bruit.

Un système de communication numérique implique la transmission d'information numériques d'une source vers une ou plusieurs destinations. La Fig. 1 illustre les éléments essentiels d'un système de communication numérique. Les messages (analogiques ou numériques) produits par la source d'information sont transformés en séquences binaires. Par souci d'efficacité, on cherche à représenter le message avec le moins de bits possible. Le processus de conversion de ces messages en séquences binaires efficaces est appelé *codeur de source* (compression des données). La séquence binaire produite par le codeur de source est ensuite transmise au codeur de canal. La tâche du codeur de canal est de créer assez de redondance pour protéger la séquence binaire. Cette redondance est ensuite utilisée au niveau du récepteur pour corriger des effet du bruit et des interférences présents dans le

canal. Enfin, la sortie du codeur de canal est transmise au modulateur, qui est le sujet principal de la thèse (surligné en rouge, voir Fig. 1). Le but du modulateur est de mettre en forme la séquence binaire avec les ondes de signal à transmettre sur le canal de communication. Selon les caractéristiques du canal de communication (espace libre, sans fil, optique...), le signal transmis peut subir différents types d'altérations (bruit, interférence, atténuation, évanouissement, distorsion). Par conséquent, pour transmettre le message de manière fiable, nous devons d'abord s'adapter aux caractéristiques du canal. Comme il existe différents types de canaux avec différentes dégradations, nous avons besoin de différents signaux modulés pour correspondre à ces canaux. Par conséquent, le bloc de modulation numérique joue un rôle essentiel dans la robustesse du message transmis.

Du côté du récepteur, nous avons le démodulateur, qui transforme le signal transmis en séquences binaires. Les séquences binaires reçues sont ensuite transmises au décodeur de canal qui essaie de récupérer le message d'information original à partir de la redondance contenue dans la séquence binaire. Le taux d'erreurs dans la séquence décodée permet d'évaluer le bon fonctionnement du démodulateur et du décodeur. La probabilité moyenne d'une erreur sur un bit à la sortie du décodeur mesure les performances de la combinaison démodulateur-décodeur. La probabilité d'erreur est une fonction des caractéristiques du code, des types de formes d'onde utilisées pour transmettre l'information sur le canal, de la puissance de l'émetteur, des caractéristiques du canal (c'est-à-dire le niveau de bruit, la nature de l'interférence), et du processus de démodulation et de décodage (la complexité du récepteur). Dans cette thèse, nous traitons de signaux non codés ; pour cette raison, nous nous concentrerons principalement sur les formes d'onde utilisées par le modulateur (démodulateur).

Enfin, la dernière étape du côté du récepteur est le décodeur de source. En connaissant la fonction d'encodage de la source, le décodeur de source tente d'estimer la redondance qui a été supprimée afin de de récupérer le message original (signal de sortie).

Dans cette thèse, nous considérons la modulation de phase continue *(CPM)*, car elle offre une haute efficacité énergétique tout en étant efficace spectralement. La CPM offre la possibilité d'utiliser des amplificateurs non linéaires efficaces en énergie grâce à leur enveloppe constante. De plus, le signal CPM présente une continuité de phase qui se traduit par un spectre avec un lobe principal plus étroit et des lobes secondaires plus faibles,

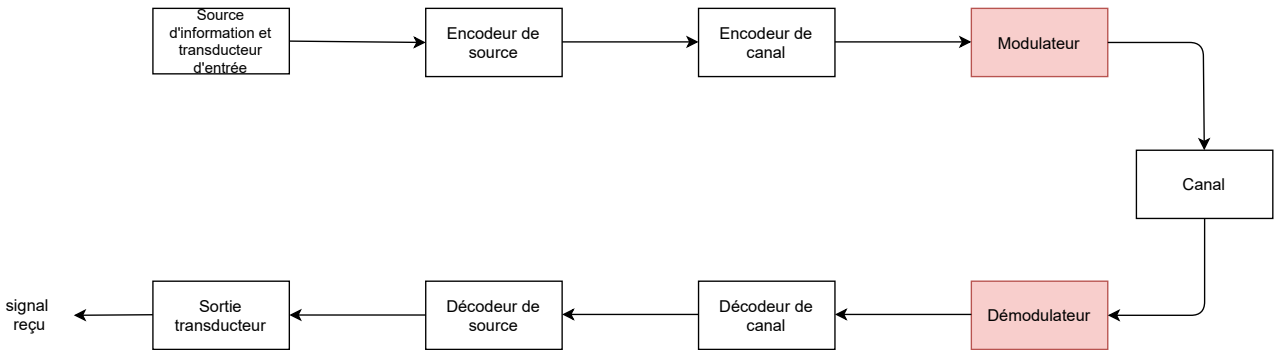

Figure 1 – Block diagram of digital communication system.

ce qui permet une utilisation plus efficace de la bande passante (modulation spectralement efficace). Les avantages des CPM sont donc : enveloppe constante, efficacité énergétique et efficacité spectrale permettent à la modulation CPM d'être largement utilisée dans différentes applications, telles que les communications mobiles [44], les communications millimétriques [12], les communications militaires [8]. De plus, les signaux CPM ont également été retenus dans des applications telles que considérés récemment pour les applications de télémétrie [58] et les communications de type machine (IOT) dans la 5ème génération (5G) de radiocommunication [10]. Par ailleurs, en raison de la mémoire introduite par la continuité de phase, une réception à l'aide d'une approche de type de détection de séquence au maximum de vraisemblance (MSLD) est nécessaire pour assurer une détection optimale. Ceci peut être réalisé par un algorithme de Viterbi (VA). Une mesure de la complexité de l'approche MLSD est le nombre de filtres et d'états appariés utilisés par le VA. Par conséquent, les avantages du CPM sont à mettre en balance avec son principal inconvénient, à savoir la complexité du récepteur.

Dans cette thèse, nous cherchons à aller au-delà de ce que les schémas CPM bien connus ont accompli. Par conséquent, nous présentons le *single side band frequency shift keying* (SSB-FSK), une nouvelle modulation à phase continue. Depuis le début des communications numériques, l'information est transmise sur la base de la modulation d'amplitude et/ou de phase d'une onde porteuse sinusoïdale, et tous ces signaux sont des signaux à double bande, c'est-à-dire un spectre centré autour de la fréquence porteuse et ayant des composantes de fréquence au-dessous et au-dessus de la fréquence porteuse. La bande latérale inférieure contient les mêmes informations que la bande latérale supérieure, donc l'une des solutions pour optimiser l'efficacité spectrale est de ne conserver qu'une seule de ces bandes en utilisant un filtre passe-bande ou la méthode de transformée de Hilbert

basée sur l'utilisation d'un déphaseur à large bande. La SSB-FSK est une forme d'onde qui génère directement un signal avec un spectre à bande latérale unique sans traitement supplémentaire, ce qui en fait un sujet passionnant pour les chercheurs. Le principe de la SSB-FSK a historiquement été découvert dans le contexte de la physique quantique [36]. Ce principe quantique a été transposée aux communications numériques permettant ainsi de définir cette modulation de la phase d'une onde électromagnétique [23]. Comme nous l'avons mentionné, la modulation SSB-FSK fait partie à la famille de la modulation de phase continue (CPM), ce qui implique que tous les avantages fournis par les schémas CPM sont également présents dans la SSB-FSK. Malgré tout, les schémas CPM actuels sont limités en termes de performance (BER, occupation de la bande passante) et de complexité du récepteur (VA et Synchronisation). Par conséquent, dans notre étude, nous nous concentrons sur la performance et la complexité de détection de la modulation SSB-FSK, avec l'objectif de surpasser ce qui a été réalisé avec les schémas CPM conventionnels.

Travaux relatifs à la SSB-FSK

Le premier système de transmission basé sur la SSB-FSK en tant que modulation CPM apparait dans les références [19, 18]. De plus, certaines propriétés, comme le schéma de démodulation cohérente symbole par symbole basé sur l'orthogonalité des signaux SSB-FSK, ont été démontrées. En raison de l'effet mémoire qui caractérise les signaux CPM, un détecteur à filtre adapté moyen a été développé, prenant des décisions en fonction d'une fenêtre d'observation donnée. De plus, une analyse de la densité spectrale de puissance (DSP) pour le cas binaire a également été fournie, ce qui nous a permis de démontrer que la DSP du signal SSB-FSK est unilatérale par rapport à la fréquence porteuse (f_c), et que presque toute la puissance est concentrée dans la première période de la bande de fréquence. Enfin, dans [20], des expressions analytiques de la densité spectrale de puissance (DSP) pour la SSB-FSK binaire et quaternaire a été présentée.

Contributions de cette these:

Faisant suite aux travaux cités précédemment, les contributions de la thèse sont les suivantes :

1. L'étude des performances du détecteur de séquences de maximum de vraisemblance (MLSD) sur les signaux SSB-FSK et les effets de tous les paramètres (indice de modulation h, largeur d'impulsion w, longueur de l'impulsion L et taille de

la modulation M) sur la probabilité d'erreur–principalement l'effet de la largeur d'impulsion w. En outre, nous apportons quelques éléments relatifs à la complexité de l'algorithme de Viterbi [22]. Nous donnons ici les performances de la probabilité d'erreur en terme d'approximation de la distance euclidienne minimale réalisable.

2. L'étude de l'effet de tous les paramètres (h, w, L, M) sur la densité spectrale de puissance (DSP) : cette étude est principalement réalisée pour $h \neq 1$, et ses résultats ont été comparés à ceux obtenus à partir du cas particulier avec $h = 1$ (associé à un véritable signal à bandes latérales uniques (BLU) pur et particulièrement pertinent pour la synchronisation) [19].

3. Une méthode pour sélectionner les meilleures combinaisons de paramètres afin d'obtenir les performances optimales du schéma SSB-FSK ; cette méthode est basée sur l'optimum de Pareto (*Pareto optimum*), qui est une méthode d'optimisation multi-objectifs. Cette étude est réalisée en deux étapes : premièrement, l'optimisation est effectuée sans contrainte sur la complexité du récepteur. Deuxièmement, la complexité est considérée comme la troisième fonction objectif, aux côtés de l'efficacité énergétique et de l'occupation de la bande passante.

4. Comparaisons énergie-bande passante pour les signaux SSB-FSK. Nous avons pu définir certaines configurations avec des compromis acceptables entre la consommation d'énergie, l'occupation de la bande passante et la complexité du détecteur permettant à la SSB-FSK de surpasser les schémas CPM classiques (par exemple, Gaussian Minimum Shift Keying (GMSK) et le Raised Cosine (RC)). Nous présentons également une nouvelle configuration SSB-FSK avec un indice de modulation entier h qui combine de bonnes performances et un avantage de synchronisation.

5. La dérivation d'une représentation PAM pour la SSB-FSK binaire non-antipodale, basée sur la décomposition PAM de Laurent [35] et Huang [30]. Cette représentation n'est pas limitée à une forme d'onde spécifique mais pourrait être utilisée pour n'importe quel schéma CPM binaire non-antipodal.

6. La conception d'un récepteur simplifié pour SSB-FSK binaire basé sur le récepteur suboptimal de Kaleh [32].

7. La proposition d'un algorithme calculant le nombre d'impulsions PAM requises par le récepteur suboptimal de Kaleh [32] pour atteindre une limite de performance spécifique. Cet algorithme est basé sur la limite de performance dérivée par Perrins et Rice [52] et l'approximation de la moyenne carrée de la PAM [40].

8. La proposition d'une nouvelle séquence d'apprentissage à partir de symboles pilotes pour la synchronisation de la SSB-FSK dans la transmission en mode burst.

Plan de thèse

Le plan de la thèse est structuré de la façon suivante :

Chapitre 1 : Dans ce chapitre, nous donnons une introduction aux modulations CPM comme base pour les chapitres suivants. Nous définissons les principaux paramètres des CPM et montrons leurs influences sur les performances. Les performances sont évaluées en termes de probabilité d'erreur, de largeur de bande et de complexité du récepteur. Le calcul de la probabilité d'erreur est basé sur l'approximation de la distance euclidienne minimale pour un canal à bruit blanc gaussien additif (BBAG). La largeur de bande a été mesurée à l'aide d'un calcul numérique de la densité spectrale de puissance en fonction de l'indice de modulation.

Chapitre 2 : Dans ce chapitre, nous présentons la SSB-FSK qui est, par sa dénomination, une modulation à bande latérale unique (SSB). Nous présentons le modèle du signal et montrons qu'elle a la caractéristique remarquable de fournir un spectre de type SSB pur très compact avec des lobes secondaires dont la puissance décroit exponentiellement. Tout d'abord, nous commençons par rappeler le principe original, inspiré de la physique quantique (lévitons). Ensuite, nous présentons les expressions analytiques utilisées pour générer le spectre SSB. De plus, nous fournissons une comparaison entre les performances de la GMSK et de la SSB-FSK (BER, bande passante et complexité du récepteur) basée sur l'analyse de l'état de l'art du schéma SSB-FSK. Nous présentons également une nouvelle méthode pour réduire la complexité du récepteur MLSD optimal pour le CPM conventionnel. Cette méthode s'inspire des singularités du schéma SSB-FSK.

Chapter 3 : Dans ce chapitre, nous faisons l'étude générale des performances du schéma SSB-FSK. Ce signal est analysé en termes d'indices de modulation, de longueurs d'impulsion et de largeurs d'impulsion, qui, tous, affectent la probabilité d'erreur, la bande passante, la propriété SSB et la complexité du récepteur. Des compromis raisonnables dans la conception des schémas de modulation sont proposés à l'aide d'une optimisation multi-objectifs afin de garantir des améliorations considérables du taux d'erreurs binaire (TEB), de l'efficacité spectrale et de la complexité sans perdre la propriété d'être un signal BLU.

Des comparaisons de performances sont effectuées avec des schémas CPM connus, par exemple la modulation GMSK et le RC.

Chapitre 4 : Dans ce chapitre, nous étudions la décomposition de la SSB-FSK en un ensemble fini de modulations d'impulsions d'amplitude (PAM). Nous utilisons la décomposition PAM comme une solution pratique pour fournir une détection en treillis à complexité réduite afin d'approcher la performance optimale théorique. De plus, nous avons développé un algorithme permettant d'obtenir les impulsions PAM nécessaires pour se rapprocher de la limite de performance optimale en utilisant des récepteurs sous-optimaux. L'algorithme est générique ; il peut fournir les résultats pour n'importe quelle combinaison de paramètres. Le système de démodulation proposé présente d'excellentes performances avec une complexité minimale par rapport au récepteur optimal de détection de séquence à vraisemblance maximale (MLSD).

Chapitre 5 : Dans ce chapitre, nous étudions la limite de Cramér-Rao (CRB) pour la synchronisation de la transmission en mode burst de la modulation SSB-FSK. Sur la base des calculs de la CRB de la CPM en mode burst, pour les schémas conventionnels à modulation de phase antipodale et spectre à double bande latérale, il a été démontré qu'il est possible d'obtenir une séquence de motifs binaires optimale qui minimise les CRBs simultanément pour l'estimation conjointe de la synchronisation des symboles, du décalage de fréquence et de la phase de la porteuse. Cependant, en raison de l'alphabet nonantipodal SSB-FSK, il est impossible d'utiliser la même séquence optimale pour minimiser les CRBs pour tous les paramètres simultanément. Dans ce chapitre, nous proposons une nouvelle séquence de motifs binaires générale qui peut minimiser la somme de tous les CRBs pour n'importe quelle modulation SSB-FSK binaire. Les résultats dérivés peuvent être utiles pour la synchronisation assistée par les données (DA) de la modulation SSB-FSK.

List of Figures

List of Tables

List of Publications

International Journals

[**IJ-2**] K. Kassan, H. Farès, D. C. Glattli, Y. Louet, « Simplified Receivers for Generic Binary Single Side Band CPM Using PAM Decomposition », in: *IEEE Access (2021)* pp. 115962-115971

[**IJ-1**] K. Kassan, H. Farès, D. C. Glattli, Y. Louet, « Performance vs. Spectral Properties For Single-Sideband Continuous Phase Modulation », in: *IEEE Transactions on Communications (2021)*, pp. 4402-4416

International Conferences

[**IC-3**] K. Kassan, H. Farès, D. C. Glattli, Y. Louet, « Single Sideband-Inspired CPM Signal Formulation For Optimal Detector Complexity Reduction», in: *2021 VTC-Fall*, (To be submitted)

[**IC-2**] K. Kassan, H. Farès, D. C. Glattli, Y. Louet, « Training Sequence Design For Burst Mode Single Side Band CPM Synchronization », in: *2021 International Symposium on Networks, Computers and Communications* pp. 1-5

[**IC-1**] K. Kassan, H. Farès, D. C. Glattli, Y. Louet, « Preamble Design for Data-Aided Synchronization of Single Side Band Continuous Phase Modulation » in: *2020 XXXIIIrd General Assembly and Scientific Symposium of the International Union of Radio Science*, pp. 1-4

National Communications

[**NC-2**] K. Kassan, H. Farès, D. C. Glattli, Y. Louet, « Performance of a single-sideband (SSB) continuous phase modulation » in: *Journée Des Doctorants de l'IETR, Rennes, 25 june 2019*

[**NC-1**] K. Kassan, H. Farès, D. C. Glattli, Y. Louet, « From quantum physics to digital communications: Application of a new waveform for high speed and low consumption transmissions at very low frequencies », in: *GDR ISIS, Rennes, 11 june 2019*

Acronyms

BER	Bit error rate
CPM	Continuous phase modulation
5G	5th generation
MLD	Maximum likelihood detection
MLSD	Maximum likelihood sequence detection
VA	Viterbi algorithm
SSB	Single side band
SSB-FSK	Single side band frequency shift keying
PSD	Power spectral density
BW	Bandwidth
GMSK	Gaussian minimum shift keying
LRC	Raised cosine frequency pulse
LREC	Rectangular frequency pulse
PAM	Pulse amplitude modulation
AWGN	Additive white Gaussian noise
ASK	Amplitude shift keying
PSK	Phase shift keying
FSK	Frequency shift keying
QAM	Quadrature amplitude modulation
PAPR	Peak-to-average powerratio
GFSK	Gaussian Frequency Shift Keying
ULE	Ultra Low Energy
DECT	Digital Enhanced Cordless Telecommunication
AIS	Automatic Identification System
GSM	Global System for Mobile communication
DVB	Digital video broadcasting

IRIG	Inter-Range Instrumentation Group
MAP	Maximum a posteriori
MF	Matched filter
FDM	Frequency-division multiplexing
FDMA	Frequency division multiple acces
AM	Amplitude modulation
ISI	Inter-symbol interference
SSB-LOSS	Single-Sideband Loss
DA	Data Aided
CRB	Cramér-Rao bound
FIM	Fisher information matrix
GA	Genetic Algorithm
UCRB	Unconditional CRB
OOK	on-off keying

SYMBOLS

M	Amplitude levels
E_s	Energy per transmitted symbol
T_s	Duration of the symbol
$s(t)$	Transmitted signal
$\phi(t)$	Information-carrying phase
α_i	Transmitted symbol
h	Modulation index
$q(t)$	Phase response
$g(t)$	Frequency pulse
L	Pulse length
BT	GMSK bandwidth parameter
$Q(.)$	Gaussian error function
$r(t)$	Received signal
$\theta(t, \alpha_n)$	Correlative state vectors
θ_n	Phase state
N_s	Number of states
$n(t)$	Complex baseband AWGN
N_0	Power spectral density of the AWGN
E_b	Mean energy per information bit
d^2_{min}	Normalized minimum squared Euclidean distance
d^2_B	Upper bound on the minimum squared Euclidean distance
$\boldsymbol{\gamma}$	Difference data sequence
N	Number of symboles
κ	Merger point index
P_k	priori probability of the data symbol k
$\phi_0(t)$	SSB-FSK phase response

$\varphi_0(t)$	Levitonic phase-shift function
w	SSB-FSK pulse width
μ	Phase correcting factor
P_{opt}	Pareto optimum
v_k	PAM pulse
ρ_k	PAM pseudo symbol
ℓ_k	PAM pulse duration
p_k	Optimum MSE PAM pulse
$\mathcal{N}$	Number of PAM main pulses
d'	Modified minimum Euclidean distance
L_0	Length of the training sequence

Table of Contents

INTRODUCTION

General context

Communication is one of the most fundamental necessities for humans, and it has progressed significantly from the end of the 18th century with the first national coded telecommunications network with the Optical telegraph. Due to the growing need for data communication, and because digital transmission supports complex signal conditioning and processing methods with simpler designs not straightforward with analog transmission, digital communication systems become more and more appealing. Below, we present some of the factors that drive to the digital communication revolution [13]:

— Digital circuits are more dependable and less expensive to manufacture than analog circuits.

— Digital technology allows for more flexibility in implementation than analog hardware.

— Digital methods are well suited to signal processing functions such as interference and jamming protection, as well as encryption and privacy protection.

— The digitization of images, sounds or documents, allows a perfect duplication because they are based on discrete signals, which enables the detection and correction of errors. However, an analog signal is a continuous signal which will always be tainted by noise.

A digital communication system involves the transmission of digital information from a source to one or more destinations. In Fig. 2, we illustrate the basic parts of a digital communication chain. The messages (analog or digital) produced by the information source are turned into binary sequences. For efficiency, we search to represent the message with the fewest possible number of bits. The process of converting these messages into efficient binary sequences is entitled *source encoding* (data compression). The binary sequence produced by the source encoder is then passed to the channel encoder. The task of the channel encoder is to create some redundancy in the binary sequence. This redundancy is used afterward at the receiver side to overcome the effect of the noise and the interference produced by the channel, in order to recover the message with the fewest

number of errors able to satisfy the target quality of transmission. Finally, the output of the channel encoder is passed toward the modulator, which is the main subject of the thesis (highlighted in red, see Fig. 2). The purpose of the modulator is to map the binary sequence to signal waves to be transmitted through the physical channel. Depending on the physical channel characteristics (free space, wireless, optical...), the transmitted signal can experience different types of impairments (noise, interference, attenuation, fading, distortion). Therefore, to reliably transmit the message, we need first to match the channel characteristics. Since there are different channel types with different impairments, we need different modulated signals to match these channels. Consequently, the digital modulation part plays an essential role in the robustness of the transmitted message.

At the receiver side, we have the demodulator, which remaps the transmitted signal to binary sequences. The received binary sequences are then passed to the channel decoder whose role is to try to recover the original information from the redundancy contained in the binary sequence. An evaluation of how well the demodulator and decoder operate is the frequency with which errors appear in the decoded sequence. The average likelihood of a bit error rate (BER) at the output of the decoder measures the joint performance of the demodulator and the decoder. The occurrence of error is a function of the code features, the types of waveforms used to transmit the information across the channel, the transmitter power, the channel characteristics (i.e., the level of noise, the nature of the interference), and the demodulation and decoding process (the receiver complexity). In this thesis, we deal with non-encoded signals; for that reason, the main focus will be on the waveforms used by the modulator (and detection functions to be implemented at the demodulator). Finally, the last step at the receiver side is the source decoder. Assuming that source encoding function is perfectly known, the source decoder carries the output of the channel decoder and tries to recover the original message (output signal).

In this thesis, we consider Continuous phase modulation *(CPM)*, because it offers a lot of power and spectrum efficiency potential. CPM provides the possibility to use nonlinear cost-effective, and power-efficient amplifiers due to their constant envelope. Moreover, CPM exhibits the phase continuity results in a spectrum with a narrow main lobe and lower sidelobes [5], allowing for more efficient bandwidth usage (Spectral efficient modulation). These advantages: constant envelope, power efficiency, and spectral efficiency allow CPM to be widely utilized in different applications, such as mobile communications [44],

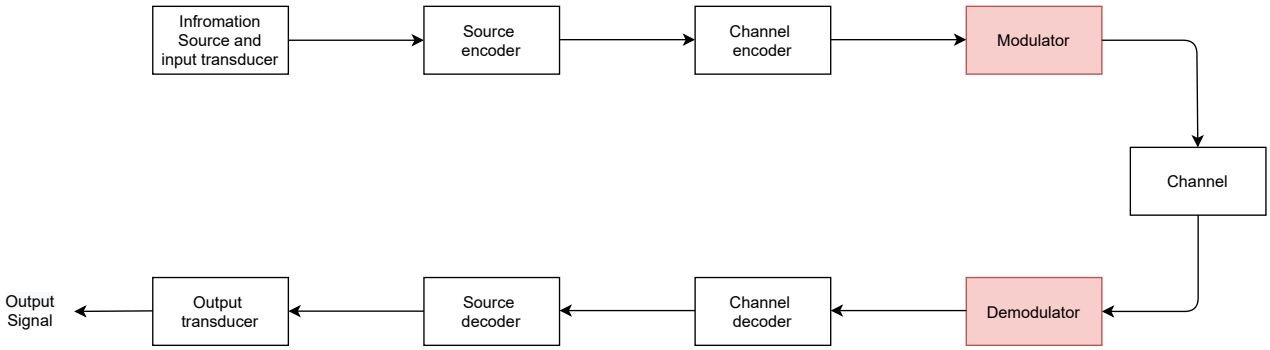

Figure 2 – Block diagram of digital communication system.

millimeter communications [12], military communications [8]. Moreover, the CPM signals are also recently considered for telemetry applications [58] and machine type communication in the 5th generation (5G) of radio communication [10]. Besides, due to the memory introduced by phase continuity, CPM signals require reliable reception using the maximum likelihood sequence detection (MLSD) approach, which can be applied using the Viterbi algorithm (VA). A measure of the MLSD complexity is the number of matched filters and states employed by the VA. As a result, these many advantages of CPM face a major drawback, which is the complexity of the receiver.

In this thesis, we aim to go beyond what well-known regular CPM schemes have accomplished. Therefore, we present the *single side band frequency shift keying* (SSB-FSK), a new continuous phase modulation originated from quantum physics [19]. From the beginning of digital communication, the information is transmitted based on the amplitude or/and phase modulation of a sinusoidal carrier wave, and all of these signals is a two-sided signal, which means a spectrum centered around the carrier frequency and having frequency components below and above the carrier frequency. The lower sideband contains the same information as the upper sideband, so one of the solutions to optimize spectrum efficiency is to keep only one of these bands by using a bandpass filter or by using a simpler method, the Hilbert transforms based on using a wide-band phase shifter. SSB-FSK is a waveform that directly generates a signal with a single sideband spectrum without any need of bandpass filtering, making it an exciting subject for researchers. The principle of SSB-FSK was historically discovered in the context of quantum physics, where a single sideband modulation of the quantum phase of an electron had an important advantage [36]. It is the principle of this modulation that is transposed here to the

(classical) phase of an electromagnetic wave [23]. As we mentioned, the SSB-FSK modulation is part of the CPM family, which implies that all the advantages provided by CPM schemes are also presented in SSB-FSK. Current CPM schemes are limited in performance (BER, bandwidth occupancy) and receiver complexity (VA and Synchronization). Therefore, in our study, we focus on the performance and detection complexity of the SSB-FSK modulation, with the objective to surpass what was achieved with conventional CPM schemes.

Related works on SSB-FSK

The first system model for SSB-FSK as a CPM modulation was provided in [19, 18]. Additionally, some properties, such as the symbol-by-symbol coherent demodulation scheme based on the orthogonality between SSB-FSK signals was shown. Due to the memory effect characterizing the CPM signals, an average matched filter detector was developed, making decisions according to a given observation window. Moreover, an analysis of the power spectral density (PSD) for the binary case was also provided, leading us to demonstrate that the PSD of the SSB-FSK signal is unilateral with respect to the carrier frequency (f_c), and almost all of the power is concentrated in the first period of the frequency band. Finally, in [20], an analytical expression of the power spectral density (PSD) for binary and quaternary SSB-FSK was presented.

Contribution of this PhD thesis

The thesis contributions are the following:

1. The study of the Maximum Likelihood Sequence Detector (MLSD) performance on the SSB-FSK signals and the effects of all parameters (modulation index h, pulse width w, pulse length L, and modulation level M) on the error probability performance—mainly the effect of pulse width. Additionally, we highlight some points related to memory performed by the Viterbi algorithm [22]. We gave the error probability performance in terms of an approximation of the achievable minimum Euclidean distance.
2. The study of the effect of all parameters,modulation index, pulse width, pulse length, and modulation level on the PSD: this study is mainly performed for modulation index different then one, and its results have been compared to those ob-

tained from the particular case of modulation index equal to one (responsible of pure SSB signal and particularly relevant for synchronization purpose) [19].

3. A method to select the best parameter combinations to obtain the optimal performance of the SSB-FSK scheme; this method is based on the *Pareto optimum*, which is a multi-objective optimization method. This study is done in two steps: first, the optimization is performed without any constraint on the receiver complexity. Second, the complexity is considered as the third objective function, alongside energy efficiency and bandwidth (BW) occupancy.

4. Energy-bandwidth comparisons for SSB-FSK signals. We were able to define some configurations with acceptable tradeoffs between energy consumption, BW occupancy, and complexity for SSB-FSK, which outperform popular CPM schemes (e.g., Gaussian Minimum Shift Keying (GMSK) and Raised Cosine (RC)). We also present a new SSB-FSK configuration with an integer modulation index h that combines good performance and synchronization advantage.

5. The derivation of a pulse amplitude modulation (PAM) representation for binary non-antipodal SSB-FSK, based on Laurent [35] and Huang [30] PAM decomposition. This representation is not restricted to a specific waveform but could be used for any binary non-antipodal CPM scheme.

6. The design of a simplified receiver for binary SSB-FSK based on Kaleh's [32] suboptimal receiver.

7. The proposal of a generic algorithm computing the number of PAM pulses required by Kaleh's [32] suboptimal receiver to attain a specific performance bound. This algorithm is based on the performance bound derived by Perrins and Rice [52] and the PAM mean-square approximation [40].

8. The design of new data-aided training sequence for the synchronization of SSB-FSK in burst-mode transmission.

Dissertation outline

The dissertation outline is structured as follows:

Chapter 1: In this chapter, we gave an introduction to CPM modulation as a fundamental background needed for the following chapters. We defined the CPM main parameters and showed their impacts on the performance. The performance was evaluated based on error probability, bandwidth, and receiver complexity. The error probability performance is given in terms of an approximation of the minimum Euclidean distance for an additive white Gaussian noise (AWGN) channel. The bandwidth was measured using a numerical power spectral density calculation in terms of the modulation index.

Chapter 2: In this chapter, we presented the SSB-FSK, which is, by its denomination, a single-sideband modulation (SSB). We presented the signal model and showed that it has the remarkable characteristic of giving a very compact pure SSB spectrum with lobes whose power decreases exponentially. First, we started with the original principle, inspired by quantum physics (levitons). Then, we presented the analytical expressions used to gave the SSB spectrum. Moreover, we provided a comparison between GMSK and SSB-FSK performance (BER, bandwidth, and receiver complexity) based on the state-of-the-art analysis of the SSB-FSK scheme. Besides, we also showed a novel method to reduce the complexity of the optimal MLSD receiver for conventional CPM. The method was inspired from the SSB-FSK scheme singularities.

Chapter 3: In this chapter, we revoked the performance of the SSB-FSK scheme. This signal is analyzed in terms of modulation indices, pulse lengths, and pulse widths, all of which affect error probability, bandwidth, SSB property, and receiver complexity. Reasonable tradeoffs in designing modulation schemes have been proposed using multi-objective optimization to ensure sizable improvements in BER, spectral efficiencies, and complexity without losing the property of being a SSB signal. Performance comparisons are made with known CPM schemes, e.g., Gaussian Minimum Shift Keying (GMSK) and Raised Cosine based CPM (RC).

Chapter 4: In this chapter, we investigated the pulse amplitude modulation (PAM) decomposition of the SSB-FSK modulation. We used the PAM decomposition as a convenient solution to provide a large reduced complexity trellis detection to approach the theo-

retical optimal performance. Moreover, we developed an algorithm to obtain the necessary PAM pulses to approach the optimal performance bound using suboptimal receivers. The algorithm is generic; it can provide the results for any parameter combinations. The proposed demodulation system exhibits excellent performance with minimal complexity with respect to the maximum likelihood sequence detection (MLSD) optimal receiver.

Chapter 5: In this chapter, we derived the Cramér-Rao bound (CRB) for data-aided (DA) burst-mode transmission synchronization of the SSB-FSK modulation. Based on the CRB computations of burst-mode CPM, for conventional double sided schemes, it was shown that it is possible to obtain an optimum training sequence that minimizes the CRBs simultaneously for the joint estimation of symbol timing, frequency offset, and carrier phase. However, due to the SSB-FSK non-antipodal alphabet, it is impossible to use the same optimum sequence to minimize the CRBs for all parameters simultaneously. Meanwhile, in this chapter, we proposed a new general training sequence that can minimize the sum of all CRBs for any binary SSB-FSK. The derived results can be helpful for DA synchronization of SSB-FSK modulation.

Chapter 1

Continuous Phase Modulation

Contents

1.1 Introduction

Digital data are represented by a sequence of zeros and ones, and the goal of digital communication is to reliably transmit this data to the destination over a given transmission channel. The basic concept behind digital communications is to find efficient schemes taking M different symbols in a specified digital alphabet and converting them into waveforms that can effectively transmit the data over the communication channel. Digital modulation schemes can change based on the characteristics of the propagation channel, which means that the binary data represented by the signal can resist to different types of impairments introduced by the channels. Since different channels cause different types of impairments, signals considered for these channels can be highly different. The method of mapping a digital sequence of signals for a transmission over a communication channel is called a digital modulation or digital signaling. Digital modulation adapts the signals to the transmission channel using frequency, amplitude, or/and phase modulation of a sinusoidal carrier wave. Depending on which degree of freedom of the wave is used to map the information bits, we distinguish between linear and non-linear modulations. [1] [53]. Therefore, this section introduces some well-known linear, and non-linear modulation and their advantages and drawbacks.

1.1.1 Linear modulations

Before addressing CPM signaling, the primary purpose of the thesis, we need to start with a brief review of the main well-known linear digital modulation. We present two well-known linear digital modulations: The Phase shift keying (PSK) and the Quadrature amplitude modulation (QAM) [53]. The PSK was first developed to be used in deep-space communication, but now it is widely used in military and commercial applications [21]. One of the forms used in the PSK is called the binary PSK, where a pair of signals represents the binary symbols 1 and 0. The signals are 180 degrees out of phase with each other. It can be easily created by using two sinusoids signals and multiplying one of them by -1. More bandwidth efficient forms of the PSK modulation are called the M-ary PSK or the M-PSK modulation. In this form, instead of using just one bit in a single symbol, in M-PSK, the symbol can deal with $m = log_2(M)$ data bits. However, using this form will increase the bit error rate. The main advantage that makes the PSK modulation attractive is the slight envelope variation (not constant) introduced by this scheme, making it a good candidate for non-linear amplifiers. Many communications systems take advantage of this

modulation scheme, including satellite phones and international positioning systems. Quadrature amplitude modulations (QAM) have very high bandwidth efficiency, making it widely used in communications systems, mobile cell phone systems, and wireless networks. The QAM modulation can send two different signals simultaneously on the same carrier frequency by taking advantage of the orthogonality of the sinusoidal signals ($cos(2\pi f_c t)$ and $sin(2\pi f_c t)$) to represent the information. The more efficient structure of the QAM, called M-QAM, allows the increasing number of discrete amplitude levels to M, which permits a symbol to contain more than one bit of data. One drawback of the QAM signal is that it has a non-constant envelope, introducing a high peak-to-average power ratio (PAPR) [37]. Systems with high PAPR cannot be used with a non-linear amplifier. With QAM signaling, both amplitude and phase carry information, whereas, in the PSK, only the phase carries the information. One more important aspect of linear modulation schemes is that they belong to memoryless modulations, which can be detected using a simple receiver based on Maximum Likelihood detection (MLD). For instance, symbol-by-symbol detection is the optimal way to perform an efficient detection.

1.1.2 Non linear modulations

One of the most popular non-linear modulations is frequency shift keying (FSK). A typical M-ary frequency-shift keying (FSK) signal is generated by shifting the carrier frequency by an amount $f_n = \frac{1}{2}\Delta f I_n$, where $I_n = \pm 1, \pm 3, \ldots, \pm(M-1)$, and Δf is the amount of frequency shifted [53]. Switching from one frequency to another can be done using $M = 2^k$ separate oscillators, where k is the number of bits per symbol. These oscillators are tuned to the desired frequencies and select one of the M frequencies according to the particular k-bit symbol to be transmitted in a signal interval of duration $T_s = kT_b$ seconds, where $R_b = 1/T_b$ is the source bit-rate. The disadvantage of this approach is that it necessitates a large frequency band for the transmission of the signal due to the relatively sizeable spectral side lobes beyond main spectral band of the signal. This is caused by the discontinuity in the phase due to the sudden switching from one oscillator to another during consecutive signaling cycles. Consequently, this approach exhibits a large band occupancy. To avoid such a problem, we can modulate the signal with a single carrier whose frequency is changing continuously, hence the term continuous phase modulation (CPM). However, due to the constraint of having a continuous phase, the CPM signals introduce a memory effect, which imposes a high complexity on the receiver side. Due to this complexity, the CPM signals are less prevalent in the literature. However, the

CPM signals are very high-power efficiency signals with a constant envelope. Therefore, this type of modulation is often more preferred than linear modulation.
The CPM [1] [53] [48] has been widely used in telecommunication systems. For example, the gaussian minimum shift keying (GMSK) is a CPM signal that is extensively used in satellite links because it can introduce a very high spectral efficiency (higher than the M-PSK) it is very robust to amplifier non-linearities.

1.1.3 Non-linear vs linear modulations

In this part, we present the limitations of non-linear modulations like FSK,CPM,$\cdots$, by comparing them to linear modulation signals such as ASK, PSK, QAM,$\cdot$, [11, 54, 41]. The restriction of CPM signals data to a unit circle leads to many advantages, such as the resistance to the variations created from interference and fading and enabling cheaper amplifier components in modems, since non-linear amplifier are utilized. From one side, linear modulations transmit the data into the amplitude and the phase of the signal. As a consequence, the linear modulations are more vulnerable to variations caused by interference and fading. Moreover, linear modulations demand linear amplifier, which leads to higher receiver cost. From the other side, the linear modulations usually have better spectrum properties due to the CPM data restriction. Therefore, spectral efficiency is one of the CPM limitations.
Besides, the phase continuity of CPM signals introduce a memory effect. Due to this effect, the CPM receiver requires the detection of the signal using the maximum likelihood sequence detection (MLSD) approach, where the complexity of the MLSD highly depends on the number of states and matched filters required in the Viterbi Algorithm (VA) [22]. Unlikely, linear modulations use a less complex detection algorithm, where they can be optimally detected using symbol-by-symbol detection techniques (MLD). Hence, complexity can also be noted as a limitation of CPM schemes. Moreover, to achieve an optimal detection of the CPM signals, the MLSD required the exact knowledge of the modulation index h. Any imprecision on the modulation index h can lead to errors in the CPM signals phase tree, which consecutively yields to catastrophic errors performance at the receiver side. Therefore, the CPM modulation index h mismatch is also one of the CPM limitations. In this chapter, we are interested in CPM signals. Therefore, in Section 1.2 CPM signal model is introduced. In Section 1.3, we describe the MLSD optimal receiver. In Section 1.4, we evaluate the performance of CPM signals using the union bound for the error probability, and a numerical method to compute the PSD using the autocorrelation

approach for the bandwidth occupancy. Moreover, we also present the effect of the CPM parameters on the performance. Finally, conclusions are drawn in Section 1.5.

1.2 CPM Signal Model

In this section, we will use the complex baseband notation to represent the various signals, with the understanding that the results are applicable to a carrier modulated wave-form.
The whole class of CPM signals can be expressed as [1]

$$s(t,\alpha) = \sqrt{\frac{E_s}{T_s}} \exp\Big\{ j\phi(t;\alpha) \Big\}, \tag{1.1}$$

where E_s is the energy per transmitted symbol and T_s is the duration of the symbol. The information-carrying phase is defined as

$$\phi(t,\alpha) = 2\pi h \sum_{i=-\infty}^{+\infty} \alpha_i q(t - iT_s) \tag{1.2}$$

where α_i is the transmitted symbol that takes values from the M-ary alphabet (modulation level) $\{\pm 1, \pm 3, \ldots, \pm(M-1)\}$. Furthermore, h is the modulation index, and $q(t)$ is the phase response represented as:

$$q(t) = \begin{cases} 0 & t < 0 \\ \int_{-\infty}^{t} g(\tau) d\tau & 0 \le t < LT_s \\ \frac{1}{2} & t \ge LT_s \end{cases} \tag{1.3}$$

where $g(t)$ is a frequency pulse with a pulse length L. When $L = 1$, the signal is indicated as *full response* (no memory effect), and when $L > 1$, it is indicated as a *partial response*. Below we give some examples of several popular CPM frequency pulses:

Rectangular frequency pulse (LREC) [1]:

$$g(t) = \begin{cases} \frac{1}{2LT_s}, & 0 \le t \le LT_s \\ 0 & \text{otherwise} \end{cases} \tag{1.4}$$

1. LRC: LRC presents the pulse length L of RC signal pulse, e.g., 3RC is the RC modulation for pulse length $L = 3$.

Raised Cosine frequency pulse (LRC) :

$$g(t) = \begin{cases} \frac{1}{2LT_s}\left(1 - \cos\left(\frac{2\pi t}{LT_s}\right)\right), & 0 \leq t \leq LT_s \\ 0 \quad \text{otherwise} \end{cases} \tag{1.5}$$

Gaussian minimum-shift keying (GMSK):

$$g(t) = \frac{Q\left(2\pi BT\left(t - \frac{T_s}{2}\right)\right) - Q\left(2\pi BT\left(t + \frac{T_s}{2}\right)\right)}{\sqrt{\ln 2}} \tag{1.6}$$

with bandwidth parameter BT, which represents the -3 dB bandwidth of the Gaussian pulse. The function $Q(.)$ is the Gaussian error function defined by

$$Q(x) = \int_x^{+\infty} \frac{1}{\sqrt{2\pi}} e^{-v^2/2} dv. \tag{1.7}$$

Figures 1.1 and 1.2 show the frequency pulse $g(t)$ and the corresponding phase pulse $q(t)$ for the different waveforms.

1.2.1 CPM signals applications

In this part, we present some of the applications that use mainly CPM signals in their systems:

- **Bluetooth systems:** it uses Gaussian Frequency Shift Keying (GFSK) with $BT = 0.5$. The modulation index is between 0.28 and 0.35 [6].
- **Ultra Low Energy (ULE) mode of the Digital Enhanced Cordless Telecommunication (DECT):** it uses GFSK with $BT = 0.5$ and modulation index between 0.35 and 0.7 [16].
- **Automatic Identification System (AIS):** it uses GMSK with $BT = 0.4$ and modulation index $h = 1/2$. Due to the imperfect equipment of the low-cost AIS systems, the actual modulation index can be different ($\pm 10\%$ variation) [7].
- **Global System for Mobile communication (GSM):** it uses GMSK with $BT = 0.3$ and modulation index $h = 1/2$ [15].
- **Digital video broadcasting standard DVB-RCS2:** it uses a quaternary alphabet $M \in \{-3, -1, +1, +3\}$ CPM signals with rational modulation index. The frequency pulse is a weighted average linear combination of the RC and the REC with pulse length $L = 2$ [17].

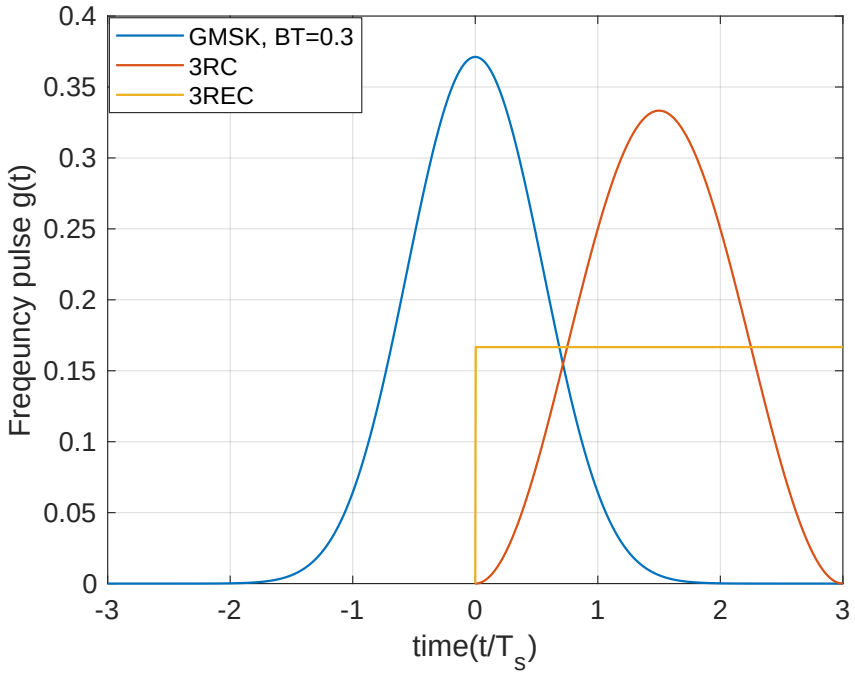

Figure 1.1 – Frequency pulses of GMSK (BT=0.3), 3RC, and 3REC.

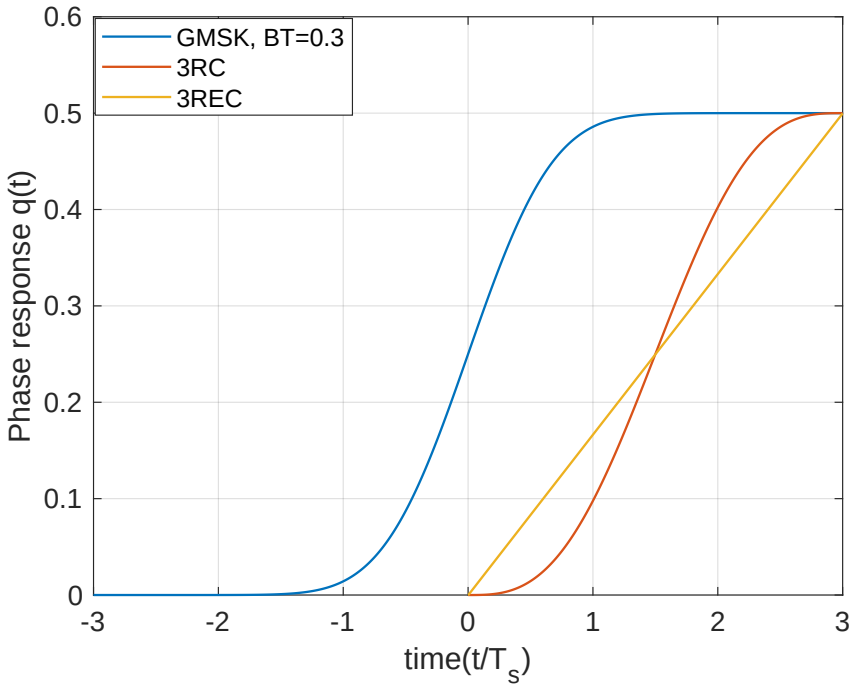

Figure 1.2 – Phase responses of GMSK (BT=0.3), 3RC, and 3REC.

— **Inter-Range Instrumentation Group (IRIG):** it uses two types of CPM signal: the aeronautical telemetry shaped-offset quadrature phase-shift keying (SOQPSK-TG) with ternary symbols $M \in \{-1, 0, +1\}$, and Advanced Range Telemetry Continuous Phase Modulation (ARTM) with quaternary alphabet $M \in \{-3, -1, +1, +3\}$. The SOQPSK-TG uses modulation index $h = 1/2$ and a frequency pulse composed of an RC filter and a windowing function with pulse length $L = 8$. The ARTM alternates between two modulation indices, $h_1 = 4/16$ and $h_2 = 5/16$. It uses RC as frequency pulse with pulse length $L = 3$ [58].

1.3 Optimum maximum likelihood sequence estimation (MLSE)

In this section, the optimal reception for signals with memory known as MLSE is given. A MLSE receiver is a receiver which selects the most likely path (sequence) corresponding to the received signal $r(t)$ over a set of possible signal intervals. The receiver is optimum if it chooses the transmitted signal with the highest probability of being sent after observing the whole sequence of the received signal $r(t)$[1].
The decision rule for optimal MLSE reception is presented in the following part of this section. The decision rule is adapted for an additive white Gaussian noise (AWGN) channel, where the MLSE correlation receiver is defined as an equivalent receiver.
If we assume that $s_i(t)$, for $i = 1, 2, \ldots, M$, represents a set of all possible transmitted sequences and that $r(t)$ represents the observed signal at the receiver, an optimal receiver estimates a received signal $s_k(t)$ if for $i = 1, 2, \ldots, M$, the following rule is satisfied:

$$f\left(s_k(t) \mid r(t)\right) > f\left(s_i(t) \mid r(t)\right) \quad i \neq k \tag{1.8}$$

where f denotes a probability density function. Equation (1.8) defines the decision rule for the optimal receiver. The probabilities presented are called *a posteriori* because the transmitted sequences probabilities are conditioned to the received sequence. Hence, a receiver depending on equation (1.8) is known as a *maximum a posteriori* (MAP) receiver [53].
Using the **Bayes'** rule we can express the conditional probability in equation (1.8) as

$$f\left(s_i(t) \mid r(t)\right) = \frac{f_R\left(r(t) \mid s_i(t)\right) \Pr\left(s_i(t)\right)}{f_R(r(t))} \tag{1.9}$$

where $f_R\left(r(t) \mid s_i(t)\right)$ is the conditional probability density of the received signal $r(t)$. The denominator in (1.9) is the unconditioned probability of receiving $r(t)$, and $\Pr\left(s_i(t)\right)$ is the source probability. By substituting (1.9) into (1.8), the MAP decision rule turns into

$$f_R(r(t) \mid s_k(t)) \Pr(s_k(t)) > f_R(r(t) \mid s_i(t)) \Pr(s_i(t)). \tag{1.10}$$

When thinking about the maximum likelihood detection, we assume that all messages $s_i(t)$ are equiprobable — $\Pr(s_k(t))$ and $\Pr(s_i(t))$ can be ignored from equation (1.10) to end up with:

$$f_R(r(t) \mid s_k(t)) > f_R(r(t) \mid s_i(t)). \tag{1.11}$$

A receiver based on (1.11) is called a MLSE receiver. For AWGN channel, it was shown in [1] that the right part of (1.11) can be expressed as a multivariate density function of $r_1, r_2, \ldots, r_{J_s}$ conditioned on the transmitted signal $s_i(t)$, where J_s is the expansion of $r(t)$ and $s_i(t)$ to J_s-dimensional signal space. The detailed analysis is not given, but the final expression of (1.11) is [1] :

$$\begin{aligned} f_R\left(r_1, \ldots, r_{J_s} | s_i(t)\right) &= \prod_{j=1}^{J_s} \frac{\exp\left[-\left(r_j - s_{ij}\right)^2 / N_0\right]}{\left(\pi N_0\right)^{1/2}} \\ &= \frac{\exp\left[-\sum_{j=1}^{J_s}\left(r_j - s_{ij}\right)^2 / N_0\right]}{\left(\pi N_0\right)^{J_s/2}}, \end{aligned} \tag{1.12}$$

where N_0 is the power spectral density of the AWGN channel. It can be observed from (1.12) that the value of the density depends on only one quantity that relates to the signal set, $\sum_j \left(r_j - s_{ij}\right)^2$. Using the **Parseval's identity** [1] and the J_s-dimensional normed vector space that was setup, we can show that $\sum_j \left(r_j - s_{ij}\right)^2 = \int \left[r(t) - s_i(t)\right]^2 dt$, which is the square norm of the difference $r(t) - s_i(t)$ (square Euclidean distance). It is now apparent from this expression that the density function f_R (1.12) is maximized by selecting $s_i(t)$ such that the Euclidean distance between $s_i(t)$ and $r(t)$ is minimized. This can be accomplished by getting the minimum of

$$\int \left[r(t) - s_i(t)\right]^2 dt = \int r^2(t) dt + \int s_i^2(t) dt - 2 \int r(t) s_i(t) dt \tag{1.13}$$

for each i. It is evident from the expression (1.13), that the distance and the correlation are equivalent, because the first term is constant with respect to i and the second one is

constant because all s_i are constant envelope. [1].
In conclusion, the objective of the optimal MLSE receiver is: **find the index k of the signal $s_k(t)$ that maximize the correlation with the received signal** $r(t)$. A receiver based on these calculations is known as a correlation receiver.

1.3.1 CPM optimum receiver

As we aforementioned, the CPM signals introduce memory due to the phase continuity. Therefore, an optimum receiver for CPM signals consists of a cross correlator followed by a MLSE detector. The task of a MLSE detector is to select a path from the CPM trellis such that the Euclidean distance between that path and the received signal $r(t)$ is minimized. An effective way to achieve such kind of search is performed by the Viterbi algorithm (VA) [22].
In the following subsection, we present the state trellis of CPM signals, which simplify the implementation of the MLSE detection and the Viterbi algorithm.

1.3.1.1 CPM recursive form

Based on $q(t)$ and $g(t)$ properties and considering that the modulation index h takes only positive rational values, the phase signal $\phi(t,\alpha)$ can be expressed as [1]

$$\begin{aligned}\phi(t,\alpha) = &\underbrace{h\pi \sum_{i=-\infty}^{n-L} \alpha_i}_{\theta_n} + \underbrace{2\pi h \sum_{i=n-L+1}^{n} \alpha_i q(t-iT_\mathrm{s})}_{\theta(t,\alpha_n)}, \\ &nT_\mathrm{s} \leq t \leq (n+1)T_\mathrm{s},\end{aligned} \tag{1.14}$$

where the right side $\theta(t,\alpha_n)$ presents the correlative state vectors $(\alpha_{n-1}, \alpha_{n-2}, \ldots, \alpha_{n-L+1})$. The number of all possible correlative state vectors is M^{L-1}. The left side θ_n is the phase state, where the number of phase states takes only p unique values modulo-2π. The number of phase states p is obtained from the modulation index $h = 2v/p$ [55] (v and p are relatively prime integer), and takes the values

$$\Theta_s = \left\{0, \frac{2\pi}{p}, \frac{2\cdot 2\pi}{p}, \ldots, \frac{(p-1)2\pi}{p}\right\}. \tag{1.15}$$

Based on (1.14), it is now possible to present the CPM signal in the form of a trellis with a finite number of states, where each branch of the trellis is presented with a starting

state (S_n), and ending state (E_n), and the $(L+1)$-tuple (σ_n) defined as

$$\begin{aligned} S_n &= (\theta_{n-L}, \alpha_{n-1}, \alpha_{n-2}, \ldots, \alpha_{n-L+1}), \\ \sigma_n &= (\theta_{n-L}, \alpha_n, \alpha_{n-1}, \ldots, \alpha_{n-L+1}), \\ E_n &= (\theta_{n-L+1}, \alpha_n, \alpha_{n-1}, \ldots, \alpha_{n-L+2}). \end{aligned} \tag{1.16}$$

The total number of states in the trellis is given by [1, 55]

$$N_{\mathrm{s}} = pM^{L-1}. \tag{1.17}$$

Fig. 1.3 presents the phase tree diagram for binary 3RC over the interval $[0, 6T_s]$. By viewing the phase modulo 2π in Fig. 1.3, we can derive the phase tree diagram. The 16-state trellis is illustrated in Fig. 1.4.

1.3.1.2 Viterbi algorithm

We assume that the signal is transmitted over a Gaussian channel. The complex-baseband received signal model is

$$r(t) = s(t, \alpha) + n(t), \tag{1.18}$$

where $n(t)$ is a complex baseband AWGN with zero mean and power spectral density N_0. Based on the previous derivation in Section 1.3, the objective of the MLSE detector is to maximize the log-likelihood function given by [1]:

$$\Lambda(\hat{\alpha}) = -\int_{-\infty}^{\infty} |r(t) - s(t, \hat{\alpha})|^2 dt. \tag{1.19}$$

Since $s(t)$ has a constant envelope, minimizing (1.19) is equivalent to maximizing the correlation function [1]

$$\lambda(\hat{\alpha}) = \mathrm{Re}\left\{ \int_{-\infty}^{\infty} r(t) s^*(t, \hat{\alpha}) dt \right\}, \tag{1.20}$$

where $(\cdot)^*$ is the complex conjugate. The operation (1.20) serves as the foundation for a correlation receiver, in which all possible transmitted signals $s(t, \alpha)$ are correlated with the received signal $r(t)$, and the data sequence $\hat{\alpha}$ maximizing the correlation is chosen as the received data. Even with sufficiently short data bursts, this is not a practicable

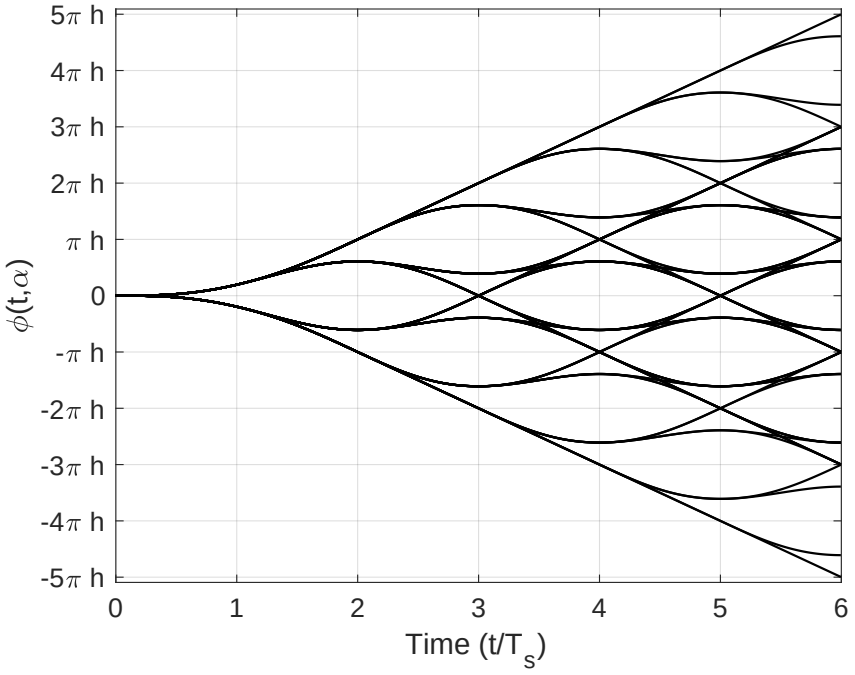

Figure 1.3 – Phase tree diagram for the binary 3RC.

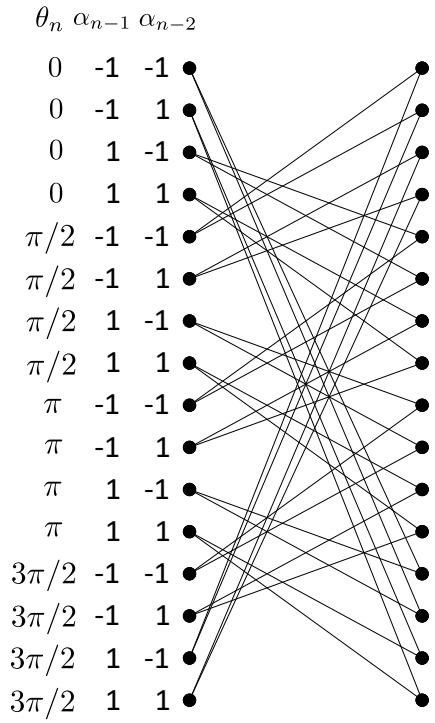

Figure 1.4 – The state trellis diagram for the binary 3RC with $h = 1/2$.

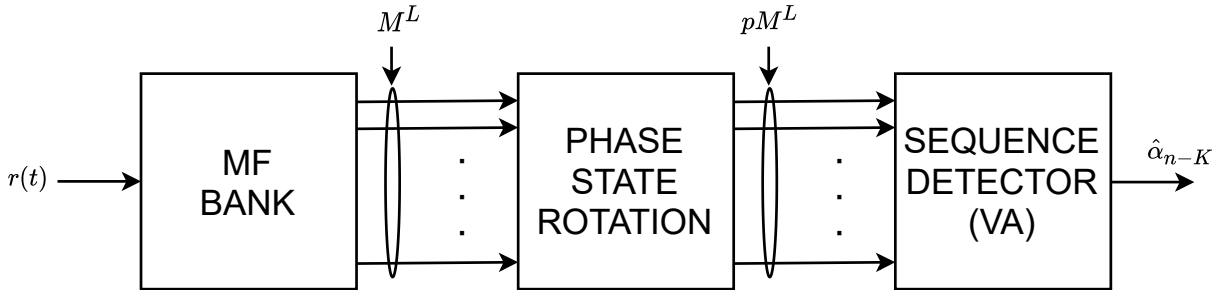

Figure 1.5 – Optimal MLSE detector for CPM

structure.

An efficient method of computing (1.20) is to use the Viterbi Algorithm (VA) [22].

Due to the trellis-like structure of the CPM modulation (1.14), and the definition of the starting states, ending states, and the $(L+1)$-tuple (S_n, E_n, σ_n) (1.16). Equation (1.20) can be computed recursively with

$$\lambda_{n+1}(\hat{E}_n) = \lambda_n(\hat{S}_n) + \mathrm{Re}\left\{e^{-j\theta_{n-L}} Z_n(\hat{\alpha}_n, \hat{\theta}_n)\right\}, \tag{1.21}$$

where $\lambda_n(\cdot)$ and $e^{-j\theta_{n-L}}$ are the cumulative metric and the cumulative phase for a given state at index n, respectively. The sampled matched filter output $Z_n(\cdot)$ is given by:

$$Z_n(\hat{\alpha}_n, \hat{\theta}_n) = \int_{nT_s}^{(n+1)T_s} r(t) e^{-j(\hat{\theta}_n + \theta(t, \hat{\alpha}_n))} dt. \tag{1.22}$$

Figure 1.5 shows the receiver implementation. The received signal $r(t)$ is fed into a bank of matched filters (MFs). The MFs are based on the correlative phase $\theta(\cdot)$, which generates M^L complex-valued outputs, one for each correlative state vector value. The outputs of the MFs are then rotated by the p phase states, resulting in pM^L real-valued inputs to the VA. After that, it is the matter of implementing the VA; each ending state E_n has M possible merging metrics. The one with the highest value is declared as the survivor and is saved for the next iteration. After some delay K, the VA traces back along the path of local survivors and outputs the survived branch symbol $\hat{\alpha}_{n-K}$ associated with this path.

1.4 CPM performance

Two metrics often assess the performance of CPM signals: the symbol error probability (error performance) and the bandwidth that a CPM signal occupies (spectral efficiency). Based on these two metrics, we can define some rules to select a CPM scheme from another. For a full comprehension of CPM performance, it is necessary to make a detailed study of the effect of each CPM parameter (h, L, M, $g(t)$) on these two metrics.

1.4.1 Error performance

In this part, we consider the error performance of a CPM signal when transmitted over an additive white Gaussian noise (AWGN) channel, assuming there is no channel coding. To evaluate the signal's error performance, we used the same method shown in [1, Ch. 3]. We consider the union bound of the error probability as the asymptotic performance for high values of E_b/N_0, where E_b is the mean energy per information bit. The union bound is defined as in [1, Ch. 3, p. 55]

$$P_e \sim Q\left(\sqrt{d^2_{\min}\frac{E_b}{N_0}}\right), \tag{1.23}$$

where d^2_{min} is the normalized minimum squared Euclidean distance.

The normalized squared Euclidean distance (d^2) is the Euclidean difference between any two transmitted CPM data sequences $\boldsymbol{\alpha}$ and $\boldsymbol{\alpha}'$. The general form of the normalized squared Euclidean distance for any set of signals is given by

$$d^2(\alpha,\alpha') = \frac{1}{2E_b}\int_0^{NT_\mathrm{s}} |s(t,\alpha) - s(t,\alpha')|^2 dt, \tag{1.24}$$

where NT_s is the observation symbol interval length. The normalized squared Euclidean distance $d^2(\alpha,\alpha')$ can be represented as a function of a single difference data sequence $\boldsymbol{\gamma}$, where $\boldsymbol{\gamma} = \alpha - \alpha'$. Therefore, (1.24) can be rewritten as (see appendix A for the derivation details)[1, ch.2]

$$d^2(\gamma) = \log_2 M.\Big\{N - \frac{1}{T_\mathrm{s}}\int_0^{NT_\mathrm{s}} \cos[\phi(t,\gamma_N)]dt\Big\}, \tag{1.25}$$

where $\phi(t,\gamma_N)$ is the phase difference trajectories.

To calculate the minimum normalized squared Euclidean distance ($d^2_{\min}$) for N observation symbols, we need to find pairs of γ that minimize (1.25). It is clear that (1.25)

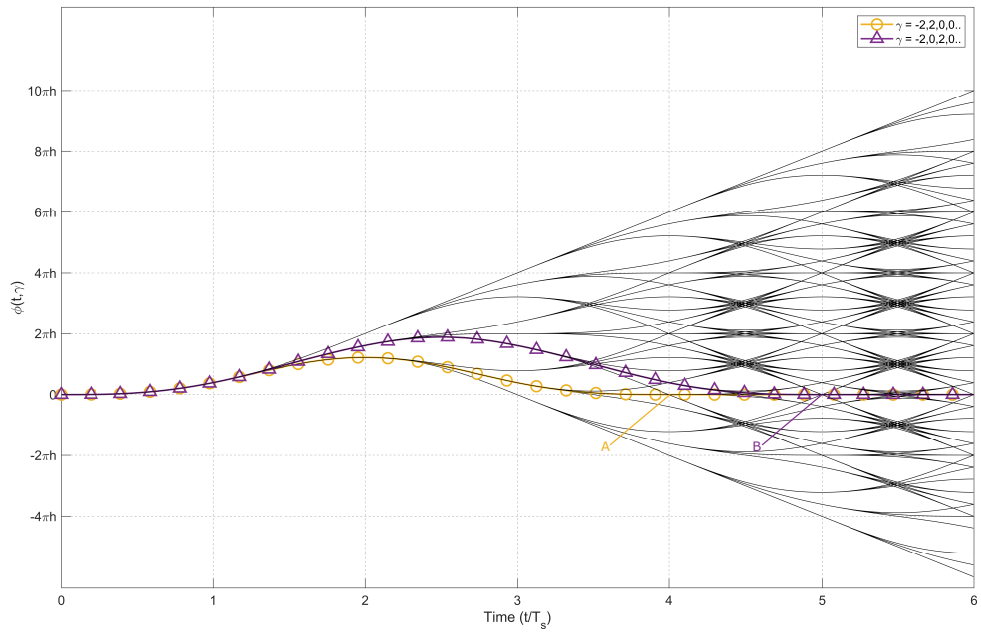

Figure 1.6 – Phase difference tree for binary 3RC. A and B indicate merges.

has a positive integral, which means that the higher the N we observe, the higher the Euclidean distance we obtain. Consequently, if we obtain an upper bound for N converging to infinity, we obtain an upper bound for any defined N. This suggests the search for the difference phase trajectories $\phi(t,\gamma)$ with the shortest duration time τ, where $\phi(t,\gamma)$ is equal to zero for all times $t \geq \tau$. Hence, an upper bound (d_{B}^2) of the Euclidean distance $d^2(\gamma)$ can be obtained using only $\phi(t,\gamma)$ with the shortest length τ. To better clarify the idea, we plotted in Fig. 1.6 the difference phase tree for any modulation index h to illustrate the method we used to obtain the boundary. Since we are presenting different phase trees, the first symbol γ_0 cannot be zero where α_0 and α_0' must not be the same. Using the difference phase tree, we can evaluate γ with the shortest length of τ. We search for the merger points between two different paths using the different phase trajectories ($\phi(t,\gamma)$) that start at $t = 0$, and coincide with the x-axis at a certain time $t = t_\kappa$, and coincide after for $t > t_\kappa$. The variable κ is the merger point index. In Fig. 1.6, we showed two of the merger points A and B, and two of the best γ combinations with the shortest τ (presented as marked lines). As a result, we can directly see that the difference phase tree with the best γ combinations (presented as marked lines) coincide at t equal to 4 and 5 with the x-axis, respectively, at the points A and B, and continue to be aligned with the x-axis from these points to the end. Usually, the time instant of the first merger point is

obtained at $t = (L+1)T_s$, for non-weak modulation schemes [1, Ch. 3, p. 73]. The phase difference tree, with the best difference sequence γ, is defined by

$$\gamma_i = \begin{cases} 0 & i < 0 \\ 2, 4, 6 \ldots, 2(M-1), & i = 0 \\ 0, \pm 2, \pm 4, \ldots, \pm 2(M-1), & 0 < i < \kappa + 1 \\ 0 & i \geq \kappa + 1 \end{cases}, \tag{1.26}$$

given that

$$\sum_{i=0}^{\kappa} \gamma_i = 0. \tag{1.27}$$

The higher the number of mergers we select, the tighter the upper bound d_{B}^2 we obtain (in Fig. 1.6, we showed only the first and the second merger points A and B, which corresponds to $\kappa = 1$ and $\kappa = 2$ respectively). As the exact number of mergers is not known [1, Ch. 3, p. 74], the number of mergers is selected by trial and is increased until there is no change in the upper bound d_B^2, given that there is no case where mergers later than the $L^{\mathbf{th}}$ needed [1, Ch. 3, p. 74].

The calculation of $d_{\min}^2$ is given using the sequential search algorithm proposed in [4]. The search algorithm requires the upper bound d_B^2; the main objective of the upper bound d_B^2 is to accelerate the algorithm search. For instance, any pair of phase trajectories with the corresponding γ_N for specific h and w values, having a distance value defined in (1.25) larger than d_B^2, will not be used again. The steps to obtain the minimum normalized squared Euclidean distance ($d_{\min}^2$) are summarized below:

- **Step 1**: select the merger point index κ.
- **Step 2**: use exhaustive search to calculate the set S_γ of difference sequences γ according to (1.26) and (2.19).
- **Step 3**: compute $d^2(\gamma)$ based on (1.25) for each difference sequence given in the set S_γ.
- **Step 4**: the upper bound of the minimum distance d_{B}^2 is equal to the minimum bound of all normalized squared Euclidean distance provided from **step 3** ($d_{\mathrm{B}}^2 = \underset{\gamma \in S_\gamma}{min}\, d^2(\gamma)$).
- **Step 5**: calculate $d_{\min}^2$ from the algorithm presented in [4], using d_{B}^2 provided from **step 4**.

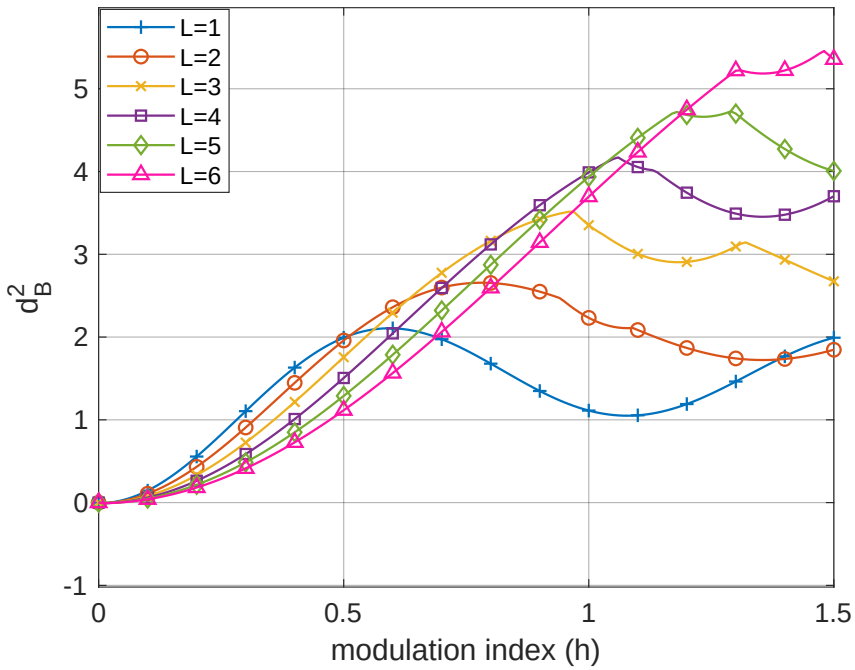

Figure 1.7 – Effect of the pulse length L on the upper bound (d_B^2) as a function of modulation index h for binary RC.

1.4.1.1 Simulation results

Several simulations on the upper bound d_B^2 and the minimum normalized Euclidean distance d_{min}^2 are shown to fully illustrate the effects of the CPM parameters on the error performance.

Fig. 1.8 depicts the variations of the upper bound d_{B}^2 as a function of modulation index h for 3RC, for M-ary alphabet $M = \{2, 4, 8, 16\}$. We can observe an increase in the upper bound d_{B}^2 for a fixed modulation index h and that the bound can approach infinity for M increases to infinity.

Fig. 1.7 illustrates the fluctuations of the upper bound d_{B}^2 as a function of the modulation index h for RC, for pulse length $L = \{1, 2, 3, 4, 5, 6\}$. Obviously, increasing the pulse length L decreases the upper bound d_{B}^2 for low modulation indices h, but increases for high modulation indices h.

Fig. 1.9 shows the performance of the minimum normalized squared Euclidean distance d_{min}^2 as a function of h for binary 3RC. The results are illustrated for different observation symbol intervals $N = 1, 2, 3, \ldots, 10$. Moreover, the minimum normalized squared Euclidean distance d_{min}^2 of the GMSK is also shown as a "x" mark. It is seen that for most

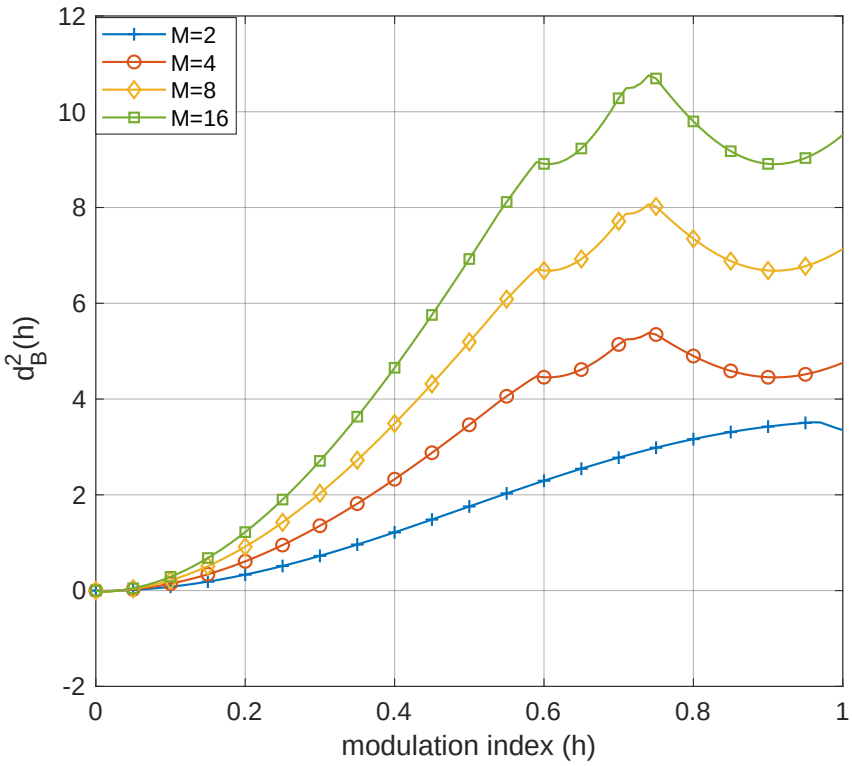

Figure 1.8 – Effect of the M-ary alphabet on the upper bound (d_B^2) as a function of modulation index h for 3RC.

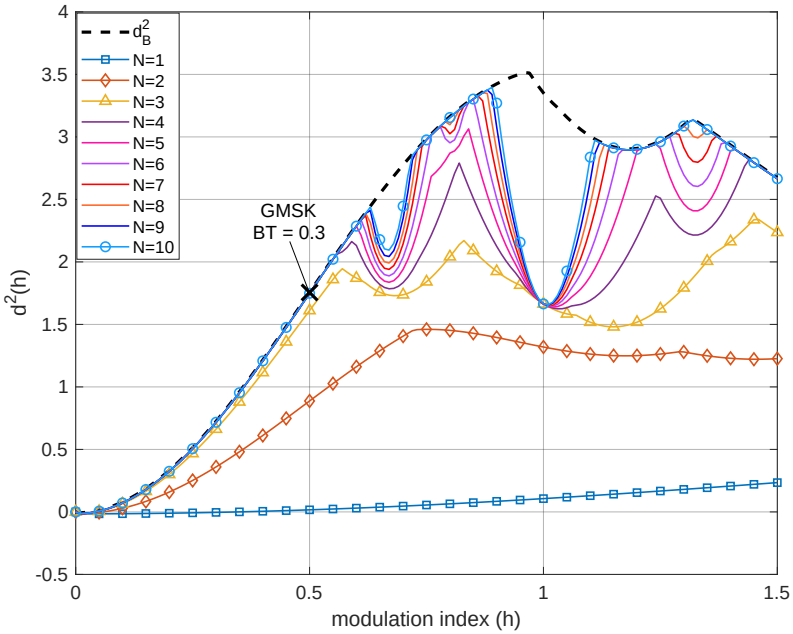

Figure 1.9 – Minimum normalized squared Euclidean distance d_{min}^2 as a function of modulation index h for binary 3RC.

h values, $d^2_{\min}$ converges to the upper bound d^2_{B} with N, but not for the weak modulation indices h_{w}. We can recognize that for $h_{\mathrm{w}} = \{0.67, 1\}$, the increase of N does not affect the increase of $d^2_{\min}$. This behavior is visible for all CPM schemes. The indices and the number of the weak modulation indices h_{w} vary with the change of the CPM scheme parameters.

1.4.2 Spectral performance

The spectrum occupancy plays an essential role in the overall performance of the transmitted signal, as the spectrum is a limited resource. Therefore, it is important to minimize the usage of this resource as much as possible. In this section, we apply a numerical method to compute the power spectral density (PSD) and, consequently, analyze the spectral efficiency of the CPM signals for different parameters $(h, L, M, g(t))$. The method is based on [1, Ch. 4] [3] and [53, Ch. 3], which is a generalization of the solution developed by Greenstein for time-limited phase response CPM signals [24].

1.4.2.1 Non-integer modulation index

The method used in [1, Ch. 4] [3] and [53, Ch. 3] for the power spectrum calculation is based on the evaluation of the autocorrelation of the Fourier transform function, given that $s(t, \alpha)$ is cyclostationary. Therefore, we first introduce the autocorrelation function, where we assume a baseband signal, given by

$$\begin{aligned} R(\tau) &= R(\tau' + mT_{\mathrm{s}}) \\ &= \frac{1}{T_{\mathrm{s}}} \int_0^{T_{\mathrm{s}}} \prod_{i=1-L}^{m+1} \left\{ \sum_{k=0}^{M-1} P_k \exp(j2\pi hk \quad [q(t+\tau'-(i-m)T_{\mathrm{s}}) - q(t-iT_{\mathrm{s}})]) \right\} dt. \end{aligned} \tag{1.28}$$

The variable $\tau = \tau' + mT_{\mathrm{s}}$ is the time difference over the interval $[0, (L+1)T_{\mathrm{s}}]$, with $0 \leq \tau' < T_{\mathrm{s}}$ and $m = 0, 1, 2, \ldots$. The variable P_k is a priori probability of the data symbol k. The PSD is achieved by using the Fourier transform of (1.28), given by

$$S(f) = 2\,\Re\left\{ \int_0^{LT_{\mathrm{s}}} R(\tau) e^{-j2\pi f\tau} d\tau + e^{-j2\pi fLT_{\mathrm{s}}} \sum_{m=0}^{\infty} C_\alpha^m e^{-j2\pi fmT_{\mathrm{s}}} \int_0^{T_{\mathrm{s}}} R(\tau + LT_{\mathrm{s}}) e^{-j2\pi f\tau} d\tau \right\}, \tag{1.29}$$

where

$$C_\alpha = \sum_{k=0}^{M-1} P_k e^{jh\pi k} \tag{1.30}$$

for h values for which $|C_\alpha| < 1$. The summation in (1.29) converges, leading to

$$\sum_{m=0}^{\infty} C_\alpha^m e^{-j2\pi f m T_\mathrm{s}} = \frac{1}{1 - C_\alpha e^{-j2\pi f T_\mathrm{s}}}. \tag{1.31}$$

Inserting (1.31) into (1.29), we obtain the PSD expression given by

$$S(f) = 2\Re\left\{\int_0^{LT_\mathrm{s}} R(\tau) e^{-j2\pi f\tau} d\tau \quad + \frac{e^{-j2\pi f L T_\mathrm{s}}}{1 - C_\alpha e^{-j2\pi f T_\mathrm{s}}} \int_0^{T_\mathrm{s}} R(\tau + LT_\mathrm{s}) e^{-j2\pi f\tau} d\tau\right\}. \tag{1.32}$$

However, equation (1.32) is only valid for $|C_\alpha| < 1$, i.e., for non-integer h. Therefore, in the next part, we apply certain modifications to obtain the PSD for integer h.

1.4.2.2 Integer modulation index

For $|C_\alpha| = 1$ (integer h), (1.31) is not valid anymore. However, with $|C_\alpha| = 1$, we can set

$$C_\alpha = e^{j2\pi v}, \quad 0 \le v < 1. \tag{1.33}$$

Based on (1.33), the summation in (1.31) can be rewritten as [53, Ch. 3, p. 141]

$$\begin{aligned} &\sum_{m=0}^{\infty} e^{-j2\pi T_\mathrm{s}(f - v/T_\mathrm{s})m} = \frac{1}{2} \\ &+ \frac{1}{2T_\mathrm{s}} \sum_{m=-\infty}^{\infty} \delta(f - \frac{v}{T_\mathrm{s}} - \frac{m}{T_\mathrm{s}}) - j\frac{1}{2}\cot \pi T_\mathrm{s}(f - \frac{v}{T_\mathrm{s}}). \end{aligned} \tag{1.34}$$

Inserting (1.34) into (1.29) leads to the complete PSD expression for integer h, which contains discrete and continuous components. Moreover, based on (1.34), the discrete spectrum spikes are located at frequencies

$$f_m = \frac{m + v}{T_\mathrm{s}}, \quad 0 \le v < 1. \quad m = 0, 1, 2... \tag{1.35}$$

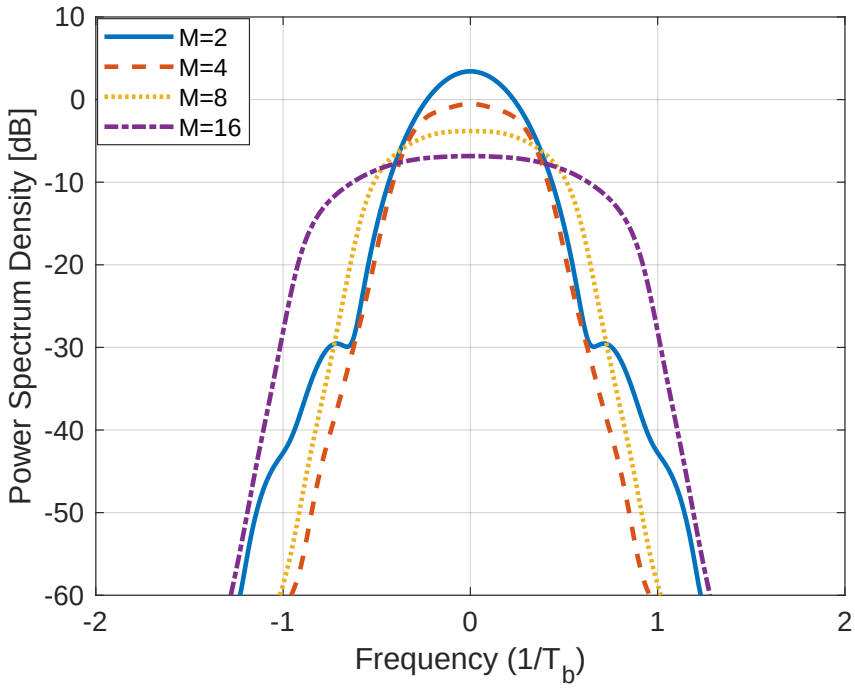

Figure 1.10 – Power spectral density of 3RC with $h = 0.5$ and for $M = \{2, 4, 8, 16\}$.

1.4.2.3 Simulation results

In this part, an evaluation of the PSD is performed in order to show the effects of the CPM parameters on the bandwidth occupancy. All PSDs are normalized, so they can be represented independently from M. The relationship between the symbol rate $1/T_s$ and the bit rate $1/T_b$ is:

$$T_\mathrm{b} = T_\mathrm{s}/\log_2 M. \tag{1.36}$$

Fig. 1.10 illustrates the PSD of 3RC for M-ary alphabet $M = \{2, 4, 8, 16\}$ with $h = 0.5$. We can notice that increasing the M-ary alphabet leads to a more compact PSD with side lobes that fall off more smoothly. This is especially identified between $M = 2$ and $M = 4$. However, increasing M also has a significant fallout, where after $M = 4$, the bandwidth occupancy starts to expand.

Fig. 1.11 shows the PSD of binary RC for $L = \{1, 2, 3, 4, 5, 6\}$ with $h = 0.5$. For 1RC, the first two side lobes are quite large; for $L = 2$, these sides lobes fall considerably, and for $L = 6$, they almost disappear. Therefore, the larger the pulse length L, the more compact

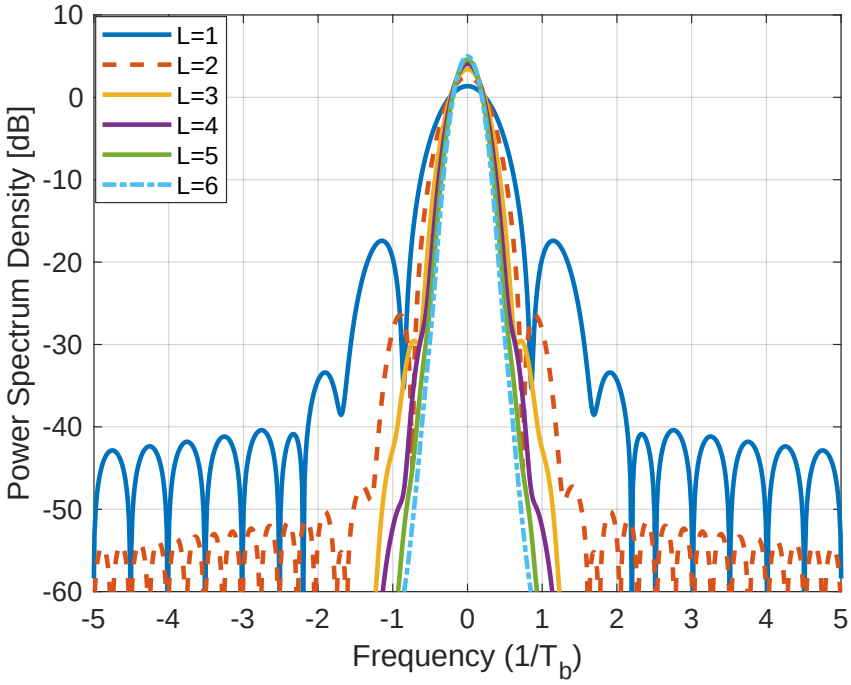

Figure 1.11 – Power spectral density of binary RC with $h = 0.5$ and for $L = \{1, 2, 3, 4, 5, 6\}$.

PSD we achieve. Indeed, the smoother the pulse, the less high frequency components in the spectrum.

Fig. 1.12 presents the PSD of binary 3RC for $h = \{1/5, 2/5, 3/5, 4/5\}$ as a function of the frequency. It is visible that we obtain a narrower bandwidth occupancy for low modulation index and oppositely for higher values. Besides, when $h = 1/5$ and $h = 4/5$, we can observe some peaking in the spectrum. This occurs when approaching integer modulation indices.

Fig. 1.13 shows the effect of the frequency pulses on the PSD. We note that the 3RC has a slightly narrower main lobe, which leads to a better bandwidth occupancy. On the other hand, the GMSK has lower side lobes and out-of-band leakage, and consequently, a lower level of interference. This means the GMSK has an advantage for applications like the frequency division multiple access (FDMA).

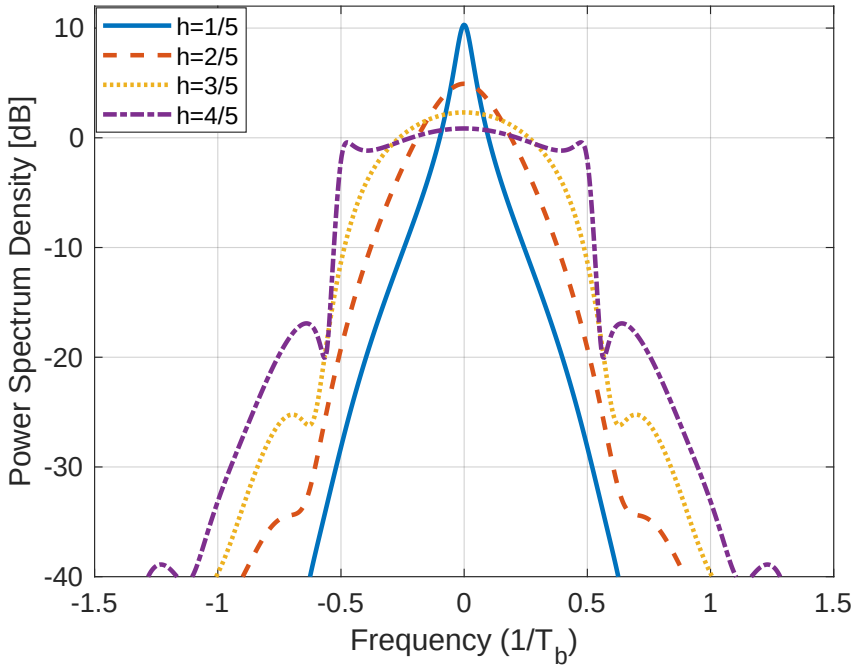

Figure 1.12 – Power spectral density of binary 3RC for $h = \{1/5, 2/5, 3/5, 4/5\}$.

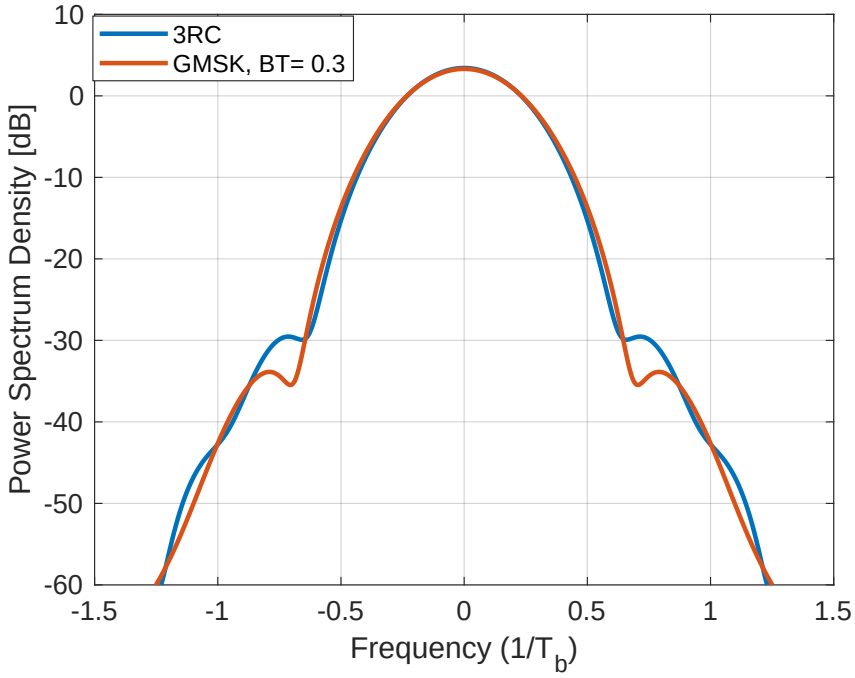

Figure 1.13 – Power spectral density of binary 3RC with $h = 0.5$ and GMSK.

1.4.3 CPM parameters analysis summary

In this part, we summarize the effects of the parameters on the CPM performance regarding error probability and bandwidth occupancy.

- Modulation index h: even if increasing h consistently increases the bandwidth (BW) occupancy, it does not carry a monotonic impact on the error probability performance.
- Pulse length L: increasing L results in a complete response of the frequency pulse filter and will introduce a better BW occupancy and lower side lobes. Based on the modulation index h values, the error probability performance can increase or decrease with L.
- Modulation alphabet M: an increase in M produces a gain in error probability performance for fixed modulation index h, while sometimes degrading the BW occupancy.
- Frequency response $g(t)$: the frequency response has a huge effect on the CPM performance, where a modification in the frequency response can lead to advantages in both the bandwidth occupancy and the error probability.

1.5 Conclusion

In this chapter, we introduced the CPM modulation. We first presented the signal model of the CPM signal with some of the popular applications for such modulation. Then, we showed the MLSD optimal detector for the CPM signal and the effect of the CPM parameters on the complexity of the MLSD receiver. To evaluate the performance of the CPM signal, we investigated the error probability based on the derivation of the minimum Euclidean distance and the bandwidth occupancy using numerical method. Moreover, we also showed the impact of CPM parameters (modulation index, pulse length, symbol alphabet) on the performance. The next chapter presents a CPM scheme inspired by quantum physics that can directly generate a single sideband spectrum. This newly introduced CPM scheme will be the main subject of this thesis.

Chapter 2

Single Side Band Frequency Shift Keying (SSB-FSK)

Contents

2.1 Introduction

In the previous chapter, a general analysis of different CPM signals was presented. We showed that CPM signals could be exploited to obtain good spectral and power efficient modulations alongside the constant envelope advantage. Due to these advantageous characteristics, several applications use CPM modulations extensively, e.g., satellite, deep-space, and wireless communication systems. The present chapter is dedicated to present a particular CPM scheme that directly generates a single side-band (SSB) spectrum which provides an excellent frequency occupation. This SSB property can be exploited to achieve high rates at low-frequency carriers without caring about the image frequency interference, typical of ordinary double side-band signals. We refer to this particular CPM scheme with *single side band frequency shift keying* (SSB-FSK). This chapter is structured as follows. Section 2.2 presents the SSB-signals and their history. The origin of the modulation derived from quantum physics is introduced in Section 2.3. Section 2.4 presents the system model and the analytical power spectrum density (PSD) of the binary SSB-FSK with an integer modulation index. Then, several simulations illustrating the bandwidth occupancy (BW) and the bit error rate performance of SSB-FSK compared to GMSK are given in Section 2.5. Finally, some conclusions are shown in Section 2.7.

2.2 Single side band modulation

Single side band (SSB) modulation [46] is used in radio communication for more efficient bandwidth and power transmission. The SSB modulation first appeared before the first World War, and then it was used for long-distance telephone lines as part of a technique known as frequency-division multiplexing (FDM). In particular, it was first used for amplitude modulation (AM) as a refinement for more efficient transmission. AM is inefficient from two points. The first is that it uses twice the bandwidth of the maximum audio frequency, and the second is that it is inefficient in terms of the power used. Single sideband modulation improves the efficiency of the transmission by removing some unnecessary elements. In the first instance, one sideband is removed, as we know that both sidebands contain the same information. We keeps only one sideband, hence the name Single Sideband (SSB). As only one sideband is transmitted, the single sideband signal shows several advantages. First, there is a reduction by one half of the transmitted power in the transmitter power. Second, the receiver bandwidth (BW) can be reduced by

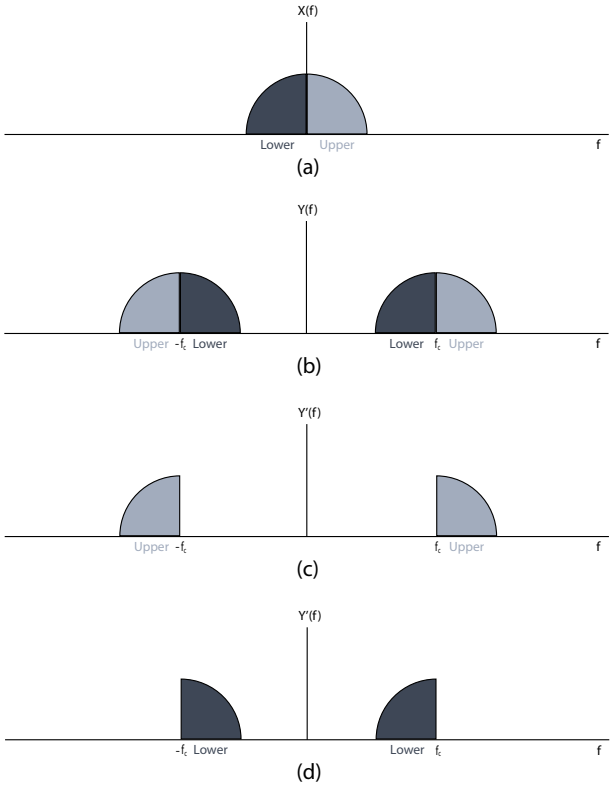

Figure 2.1 – Double and single side band: (a) spectrum of the base band signal, (b) spectrum of modulated signal with sinusoidal carrier, (c) spectrum with only upper side bands, (d) spectrum with only lower side bands.

half; this improves the signal to noise ratio because the narrower BW used will allow less noise and interference. The SSB modulation offers a far more effective solution for radio communication because it offers a significant improvement in spectrum efficiency. Beside, the only drawback of the ssb modulation is: adding more complexity to the transmitter and the receiver.

Below we present some of the methods used to create SSB signals. Fig 2.1 (a) presents the spectrum of a base band signal $x(t)$. With a sinusoidal carrier at frequency f_c (Fig 2.1 (b)), we notice that the spectrum of the signal is shifted to $-f_c$ and f_c, and that the bandwidth occupancy is doubled. This indicates that there is a redundancy in the transmitted information, where it is clear from Fig 2.1 (b), that we can recover all the information $X(f)$ from only the upper/lower side bands at positive and negative frequencies. The resulting spectrum if only the upper/lower side bands are saved are shown in Fig 2.1 (c) and Fig 2.1 (d), respectively. The transformation of $x(t)$ to the forms presented in

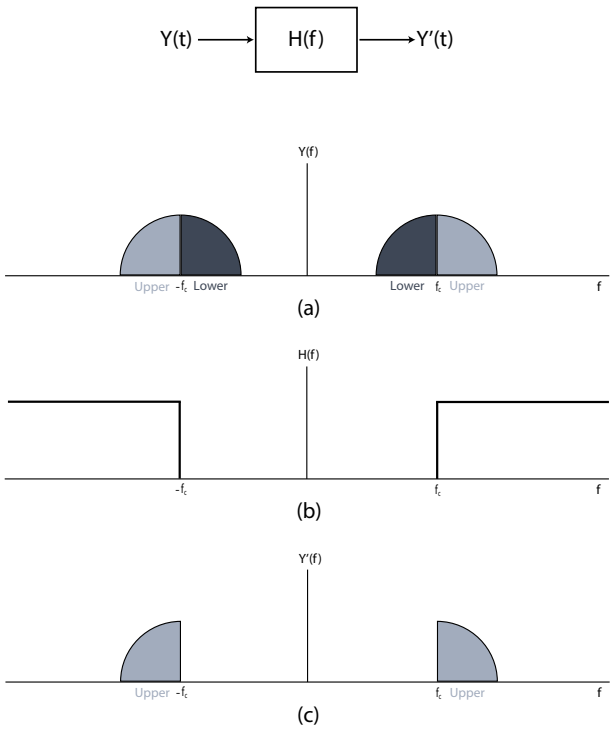

Figure 2.2 – Removing unwanted side bands with bandpass filter: (a) spectrum of the modulated signal with sinusoidal carrier, (b) ideal bandpass filter, (c) spectrum with only upper side bands.

Fig 2.1 (c) and (d) is referred to as *single side band modulation*. This transformation can be achieved using different methods. One is to apply a bandpass filter to sharply cut the unwanted side bands as showed in Fig. 2.2. Another method is to use a phase shifting. Fig. 2.3 depicts the system used to remove the upper side bands. The system $H(f)$ is a phase shifter (Hilbert transform) used to delay every component of $x(t)$ by $\pi/2$. The resulting signal is $\hat{x}(t)$, the Hilbert transform of $x(t)$. The spectrum of $x(t)$, $y_1(t) = x(t)\cos(2\pi f_c t)$, $y_2(t) = \hat{x}(t)\sin(2\pi f_c t)$, and $y(t) = x(t)\cos(2\pi f_c t) - \hat{x}(t)\sin(2\pi f_c t)$ are illustrated in Fig. 2.4.

In this study, we are interested in a unique waveform that directly generates a signal with an SSB spectrum. This waveform is able to generate a SSB signal *directly* without any additional treatment (Filtering, Hilbert transforms) [19][18]. We present the origin of this SSB modulation in the next section.

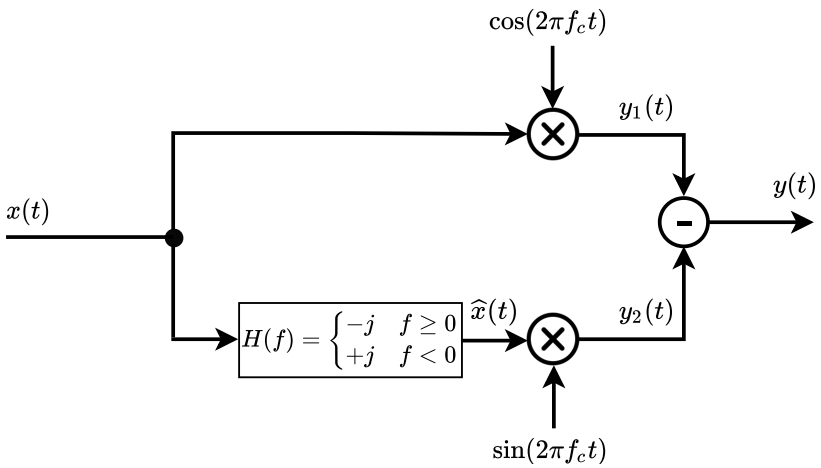

Figure 2.3 – Scheme for single side band modulation, using $\pi/2$ phase shifter to remove the upper side bands.

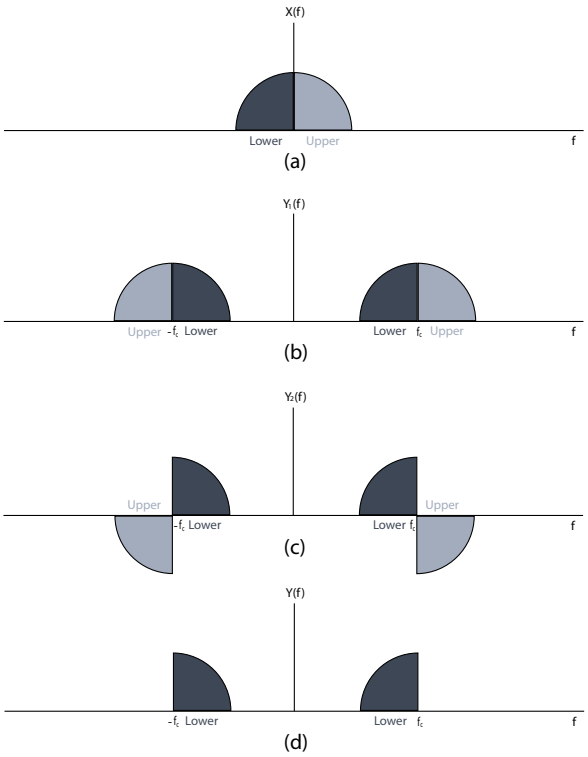

Figure 2.4 – Spectrum of the modulated signal associated to the system presented in Fig. 2.3. (a) spectrum of the baseband signal, (b) spectrum of the modulated signal with sinusoidal carrier, (c) spectrum of the filtered modulated signal using Hilbert transform, (d) spectrum with only lower side bands.

2.3 Origin of SSB signals from quantum physics

SSB-FSK originates from the theoretical proposal of Levitov *et al.* [36], who demonstrated how to create a pure single electron quantum state by applying a voltage pulse on a quantum conductor without creating any extra perturbation in the conductor. It is widely accepted that a quantum conductor is full of many free-moving electrons. When one electron is excited by an elementary pulse, other electrons tend to move to fill the hole created, generating undesirable neutral plasmonic waves. To overcome this issue, Levitov *et al.* predicted that one could inject an electron without causing any disturbance *if and only if* the Faraday flux $\int eV(t)dt$ is an exact multiple of the planck constant h_0, and the voltage pulse follows a Lorentzian time shape. Using the Lorentzian pulse, we can generate a pure single electron state, called a "Leviton", a new quasi-particle with minimal excitation. As a consequence, it has been shown in [14], and [31], that the electron energy distribution become SSB, i.e., its left part is removed. Based on this experimentation and remarking that the effect of the voltage pulse was to modulate the phase of the electron wave-function with Lorentzian phase pulses, the authors in [23] proposed a new CPM modulation scheme, which directly provides a SSB signal.

Fig. 2.5 presents how to generate a pure single electron without any disturbance in the quantum conductor. An elementary current pulse $I(t) = e^2V(t)/h_0$ is formed when a short voltage pulse $V(t)$ is applied to a contact of a quantum conductor carrying a single electronic mode, where e is the charge of an electron and h_0 is the Planck constant. A single electron is injected from the contact to the conductor after adjusting the amplitude and length of the pulse to create the charge $Q = \int I(t)dt = e$. In Fig. 2.5(a) we showed that a single electron was generated after applying the voltage pulse. However, in reality using arbitrary voltage pulse agitates all of the electrons contained in the conductor, resulting in a number of undesired excitations in the form of electrons and holes as presented in Fig. 2.5(b). Yet, when applying a voltage pulse with Lorentzian shape, the quantum conductor excites a single electron without any unwanted excitations as shown in Fig. 2.5(c). Fig. 2.6 presents the energy domain of the quantum conductor presented in Fig. 2.5. When an arbitrary voltage pulse is applied, unwanted excitation is generated with energy above (below) the Fermi energy of the conductor (see Fig. 2.6 (a)), therefore we obtained a double side band spectrum. In contrary, when applying Lorentzian pulse voltage, we obtained only single electron above the Fermi energy (see Fig. 2.6 (b)) — a SSB spectrum is achieved.

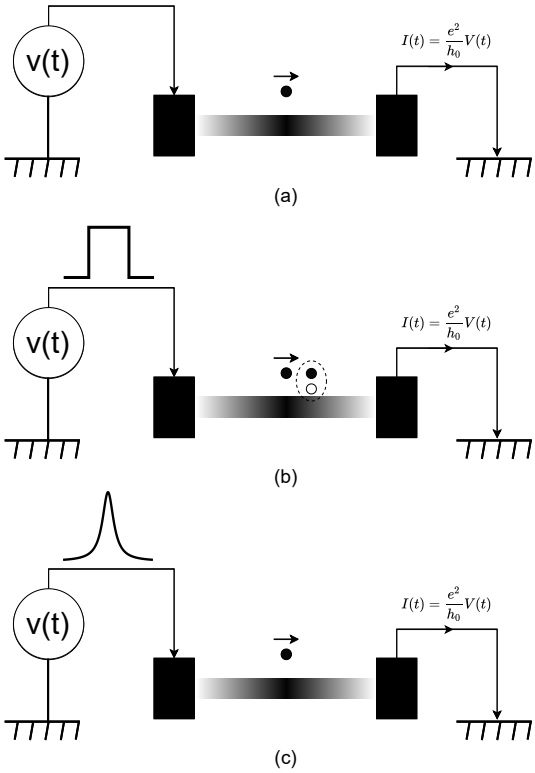

Figure 2.5 – Creating a pure single electron without any perturbation in the quantum conductor: (a) resolve current to an individual charge, (b) arbitrary voltage pulse creates unwanted excitation, (c) Lorentzian pulses provide clean injection without unwanted excitation.

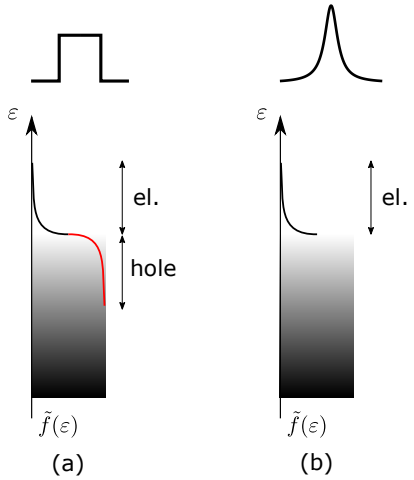

Figure 2.6 – Energy domain: (a) arbitrary pulse, double side band, (b) Lorentzian pulse, single side band.

2.4 Single side band CPM

In this part, we introduced the principle of single side band CPM (SSB-FSK), and its analytical computation of the spectrum. In [23], we can find the first proposition of the SSB-FSK CPM scheme, which directly provides a SSB signal. Then in [19] and [18], we provided the first system model of SSB-FSK as a CPM modulation.
Additionally, we introduced some properties, such as the symbol-by-symbol coherent demodulation scheme, based on SSB-FSK signals' orthogonality. Due to the memory effect characterizing the CPM signals, we developed an average matched filter detector, making decisions according to a given observation window. We then analyzed the power spectral density (PSD) for the binary case, leading us to demonstrate that the PSD of the SSB-FSK signal is unilateral with respect to the carrier frequency (f_c), and almost all of the power is concentrated in the first period of the frequency band. Finally, in [20], we presented an analytical expression of the power spectral density (PSD) for binary and quaternary SSB-FSK.
In this section, we presented a brief review of some of the aforementioned state of the art studies on SSB-FSK.

2.4.1 The essential of SSB-FSK modulation

The Fourier transform of the complex signal $x(t) = e^{-j\phi(t)}$ is defined by

$$X(f) = \int_{-\infty}^{+\infty} e^{-j\phi(t)} e^{j2\pi ft} dt. \tag{2.1}$$

The necessary condition to obtain a single side-band spectrum is to have a finite value for $f > 0$ and zero value for $f < 0$. Accordingly, $x(t)$ should at least have one pole in the upper and no poles in the lower complex plane. The simplest mathematical form of $x(t)$ respecting these conditions is given by [20]

$$x(t) = e^{-j\phi(t)} = \frac{t - t_0 + jw_0}{t - t_0 - jw_0}, \tag{2.2}$$

where the pole has been arbitrarily chosen at $t = t_0 + jw_0$, with w_0 is the pulse width at a pulse time t_0. As a result, the general *levitonic* phase term $\phi(t) = \varphi_0(t) = 2\arctan\left(\frac{t-t_0}{w_0}\right)$

is formed, and the elementary frequency pulse is given by its derivative

$$g(t) = \frac{2w_0}{(t-t_0)^2 + w_0^2}. \tag{2.3}$$

This results on the Fourier transform $X(f) = e^{-4\pi w_0 f}$ for $f > 0$ and zero otherwise. The extension of this idea is to add more poles only in the upper complex plane, allowing $X(f)$ to keep the original SSB property. Precisely, this extension entails producing more complex phases, which are the sum of N elementary phases $\varphi_i(t)$ of type $\varphi_0(t)$ that occur at time t_i and width w_i ($w_i > 0$). As a result, the general form of $x(t)$ is

$$x(t) = e^{-j\phi(t)} = \prod_{i=0}^{N-1} \frac{t - t_i + jw_i}{t - t_i - jw_i}, \tag{2.4}$$

and the general form of the phase shift function $\phi(t)$ is

$$\phi(t) = \sum_{i=0}^{N-1} h_i \varphi_i(t) \tag{2.5}$$

where h_i are integers with the same sign. If $h_i > 0 \ \forall i$, $X(f)$ has zero values for $f < 0$, and similar if $h_i > 0 \ \forall i$, $X(f)$ has zero values for $f > 0$. This explains why no antipodal coding is used on the modulated information bits.

2.4.2 Analytical derivation of the power spectral density for integer modulation index

Let us introduce b_i a return to zero (RZ) binary sequence of bits ($b_i = \{0, 1\}$). Based on equations (2.4) and (2.5), the phase shift function is [20]

$$\phi(t) = h \sum_{i=0}^{N-1} b_i \varphi_0(t - iT_s), \tag{2.6}$$

and the base band modulated signal is, for $L = \infty$

$$x(t) = \exp(-j\phi(t)) = \prod_{i=1}^{N} \left(\frac{t - iT_s + jw}{t - iT_s - jw} \right)^{b_i}. \tag{2.7}$$

The Fourier transform of the correlation function $C(\tau) = \frac{1}{T_s} \int_0^{T_s} E\left[x(t)^* x(t+\tau)\right] dt$

provides the PSD $P(f) = \int_{-\infty}^{\infty} C(\tau)\exp(-j2\pi\tau)d\tau$.
Let $T_s = 1$ and consider b_i as an uncorrelated Bernouilli random variable with probability $P[b_i = 1] = p$ and $P[b_i = 0] = 1 - p$. The two-time correlation function is given by [20]

$$C\left(t - \frac{\tau}{2}, t + \frac{\tau}{2}\right) = \prod_{i=-\infty}^{\infty} \left(\frac{t_i - \frac{\tau}{2} - jw}{t_i - \frac{\tau}{2} + jw} \cdot \frac{t_i + \frac{\tau}{2} + jw}{t_i + \frac{\tau}{2} - jw}\right)^{b_i} \tag{2.8}$$

where $t_i = t - iT_s$. We get the following result after averaging (2.8) across statistically equivalent bit sequences

$$\begin{aligned} E\left[C\left(t - \frac{\tau}{2}, t + \frac{\tau}{2}\right)\right] &= \prod_i \left(1 - p + p\frac{t_i^2 - \left(jw + \frac{\tau}{2}\right)^2}{t_i^2 - \left(jw - \frac{\tau}{2}\right)^2}\right) \\ &= \frac{\sin\left(\pi(t - \theta_p(\tau))\sin\left(\pi\left(t + \theta_p(\tau)\right)\right)\right.}{\sin\left(\pi(t - jw + \frac{\tau}{2})\sin\left(\pi\left(t + jw - \frac{\tau}{2}\right)\right)\right.}, \end{aligned} \tag{2.9}$$

where $\theta_p(\tau) = \sqrt{\frac{\tau^2}{4} - w^2 - (1 - 2p)jw\tau}$. The time average of equation 2.9 gives the required correlation function $C(\tau)$ to computes the PSD. The analytical PSD expression for $p = 1/2$ is given by

$$C(\tau) = 1 + \frac{\cos\left(\pi\sqrt{\tau^2 - 4w^2}\right) - \cos(\pi(\tau - 2jw))}{\sin(\pi(\tau - j2w))}. \tag{2.10}$$

The first term in the numerator characterizes the continuous spectrum anticipated from the random symbol transmission. The second term, when paired with the denominator, is periodic and is responsible for producing the narrow peaks in the spectrum (see Fig. 2.7). The appearance of the narrow peaks is expected, due to the presence of integer modulation index h in (2.6) [1].

Fig. 2.7 illustrates the theoretical PSD of SSB-FSK modulation with integer modulation index h, and pulse width $w = 0.37$. The frequencies are in units of $1/T_b$. The PSD of the SSB-PSK modulated signal is definitely unilateral, where almost all of the power is concentrated in the $1/T_b$ frequency band. Moreover, the PSD starts to decreases steeply with 20 dB decreases with each $1/T_b$ frequency band step. This exponential decrease is equal to $e^{-4\pi wf}$ for integer modulation index h (Section 2.4.1), where for $w = 0.37$ the decreases is equal to 20 dB.
Spectral lines (Spikes) are observed at frequencies $1/T_b, 2/T_b$, etc. They appeared due to

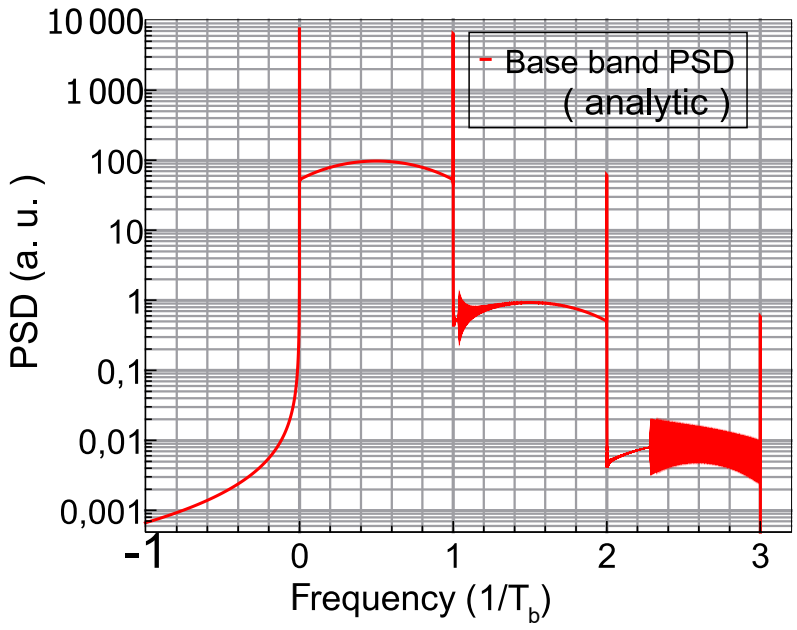

Figure 2.7 – PSD derived from the analytical numerical Fourier transform expression's (2.10) for pulse width $w = 0.37$. The rapid amplitude oscillations of the PSD for $1.1 < f < 1.2$ and $2.3 < f < 3.4$ are numerical artifacts of the FFT computation.

the periodic component present in (2.10).

Fig. 2.8 presents a comparison between regular CPM scheme and SSB-FSK. In Fig. 2.8 (a), we can observe the different spectrums of SSB-FSK (SSB) and the regular CPM (double side band) at a carrier frequency f_c. If we decrease the carrier to a very low frequency f'_c, we can observe that for regular CPM scheme an overlap with the image spectrum occur (see Fig. 2.8 (b)). However, for SSB-FSK the total absence of power in the lower sideband remarkably prevents from any image frequency and spectrum overlap (see Fig. 2.8 (c)). As a consequence, designing SSB-FSK based communication systems opens the door to low carrier frequency transmissions with higher data rate compared to non SSB schemes.

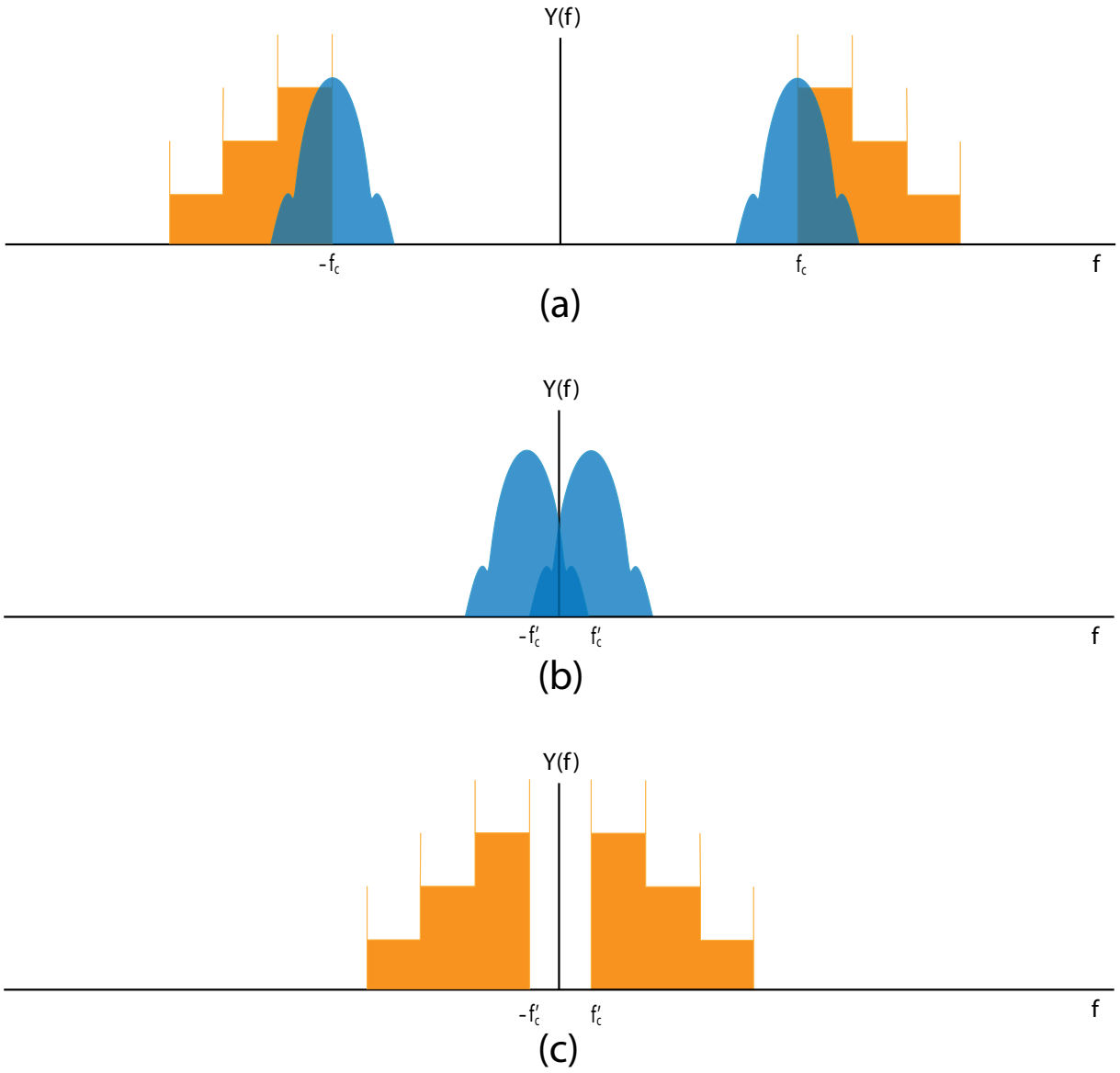

Figure 2.8 – Spectrums of SSB-FSK and regular CPM scheme at very low carrier frequency. (a) spectrum of SSB-FSK versus regular CPM. (b) overlap in the spectrum for regular CPM scheme. (c) no overlap in the spectrum for the SSB-FSK.

2.4.3 SSB-FSK signal model

The SSB-FSK is also a CPM signal (1.1), with information-carrying phase defined as

$$\phi(t,\alpha) = 2\pi\tilde{h}\sum_{i=-\infty}^{+\infty}\alpha_i\phi_0(t-iT_\mathrm{s}) \tag{2.11}$$

where α_i is the transmitted symbol that takes values from the M-ary alphabet $\{0,1,\ldots,(M-1)\}$. In order to preserve the SSB property, we have to consider positive symbols α_i, responsible of the right side band spectrum. The negative values would introduce a lower side in the spectrum. Therefore, no antipodal coding is allowed [19, 18]. Furthermore, $\tilde{h}=2h$, where h is the modulation index used to ensure a 2π phase increment. The phase response $\phi_0(t)$ is represented as

$$\phi_0(t) = \begin{cases} 0 & t<0 \\ \frac{1}{4\pi}\int_{-\infty}^{t} g(\tau)d\tau & 0\le t<LT_\mathrm{s} \\ \frac{1}{2} & t\ge LT_\mathrm{s} \end{cases} \tag{2.12}$$

where $g(t)$ is a Lorentzian frequency pulse truncated to a symbol duration $L>1$ (*partial-response*), defined as

$$g(t) = \frac{d\varphi_0(t)}{dt} = \mu\frac{2w^2}{t^2+w^2},\ t\in[-LT_\mathrm{s}/2, LT_\mathrm{s}/2]. \tag{2.13}$$

where $\varphi_0(t)$ is a Levitonic phase-shift function, given by

$$\varphi_0(t) = 2\mu\arctan\left(\frac{t}{w}\right). \tag{2.14}$$

The variable w is the pulse width, a key tuning parameter that significantly impacts the performance, mainly the spectral efficiency of the transmitted signal $s(t,\alpha)$ [19, 18].
Fig. 2.9 shows the constant envelope of the SSB-FSK modulated signal in the time domain. Furthermore, Fig. 2.10 depicts the continuity of SSB-FSK phase. As a slow decrease characterizes the Lorentzian pulse, a pulse truncation is needed to get acceptable pulse lengths (regarding especially receiver complexity). As a consequence a correcting factor μ is introduced to keep a 2π phase increment to sustain the SSB property. The correcting factor μ is defined as the ratio between the total phase increment without any truncation

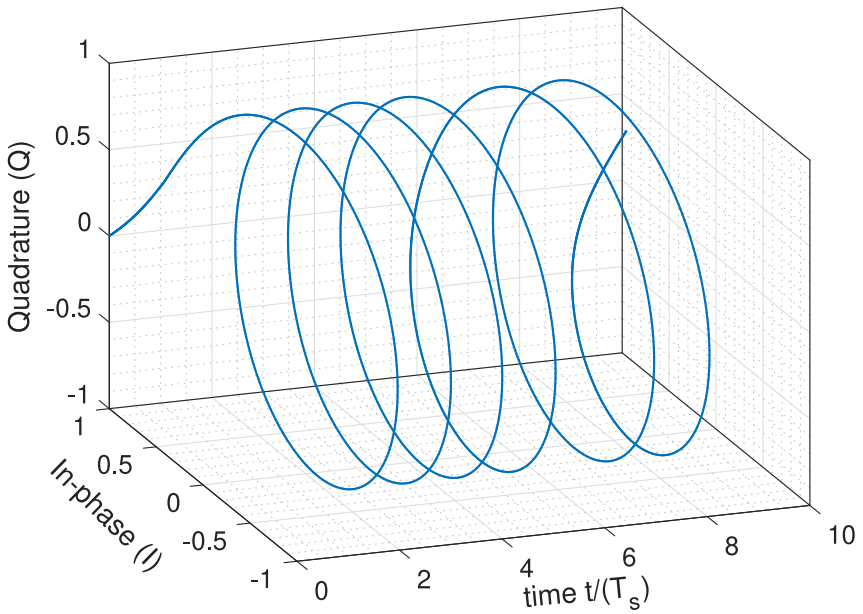

Figure 2.9 – Generated SSB-FSK signal with $L = 4$, $w = 0.3$ and $h = 1$ of the bits sequence $\{1, 1, 1, 1, 0, 1, 1, 0, 0, 1\}$.

and the one obtained after Lorentzian truncation

$$\mu(L) = \frac{2\pi}{\int_{-LT_s/2}^{LT_s/2} \frac{2w^2}{t^2+w^2} dt} = \frac{\pi}{2\arctan(\frac{LT_s}{2w})}. \tag{2.15}$$

The effect of w on the frequency pulse $g(t)$ for $L = 4$ is presented in Fig. 2.11, for different values of $w = 0.3, 0.7, 1.3$. As shown in Fig. 2.11, it is evident that increasing w brings up the tails of frequency pulse $g(t)$, which consequently increases the inter-symbol interference (ISI).

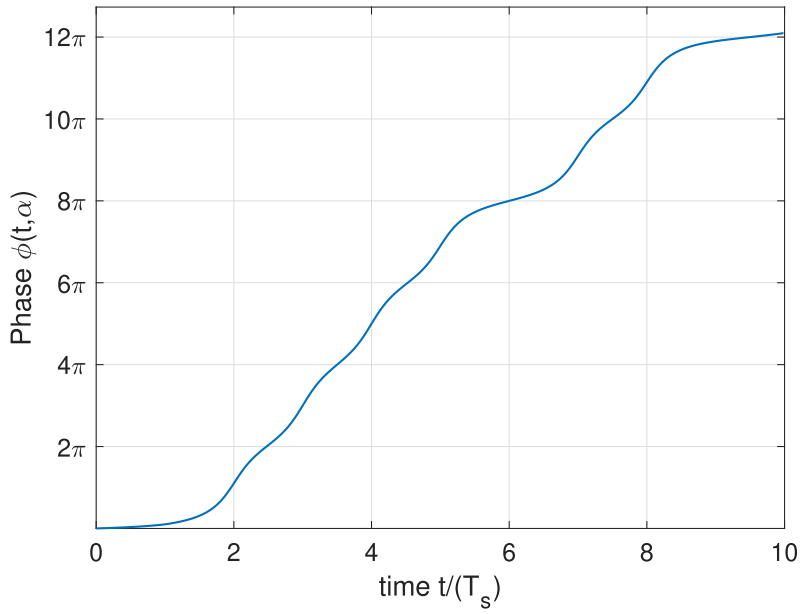

Figure 2.10 – Evolution of the phase $\phi(t, \alpha)$ with $L = 4$, $w = 0.3$ and $h = 1$ of the bits sequence $\{1, 1, 1, 1, 0, 1, 1, 0, 0, 1\}$.

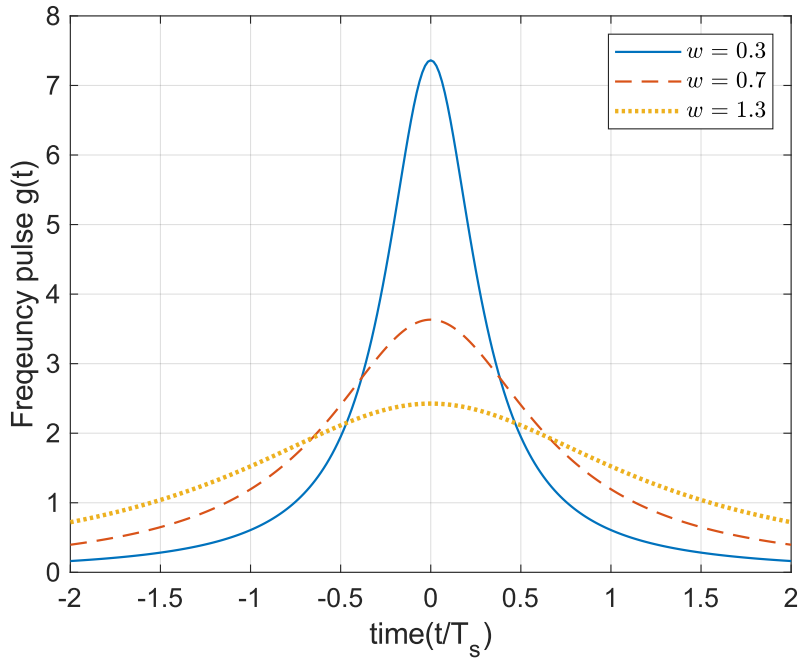

Figure 2.11 – Lorentzian pulse (L=4) for different width values, $w = 0.3, 0.7, 1.3$.

2.5 SSB-FSK numerical results and comparisons

2.5.1 SSB-FSK spectral performance

A comparison between the PSD of the SSB-FSK and the GMSK is presented in Fig. 2.12. The computation of the PSD was achieved using the numerical method presented in Section 1.4.2. The PSD of the SSB-FSK is indeed SSB compared to the GMSK, where the PSD is symmetrical (double side band).
In Table 2.5.1, we present the 99% bandwidth occupancy of the SSB-FSK with $w = 0.37$ and $h = 1$ for different pulse lengths L. We can observe that when L is increasing, the bandwidth occupancy is decreasing, which means the less truncated the Lorentzian pulse, the better spectrum we maintain. For comparison, we also gave the bandwidth occupancy of the GMSK. For $BT = 0.3$, the bandwidth occupancy is equal to 0.91. We can clearly note that for these selected parameters for the SSB-FSK, the GMSK achieved a better bandwidth occupancy.

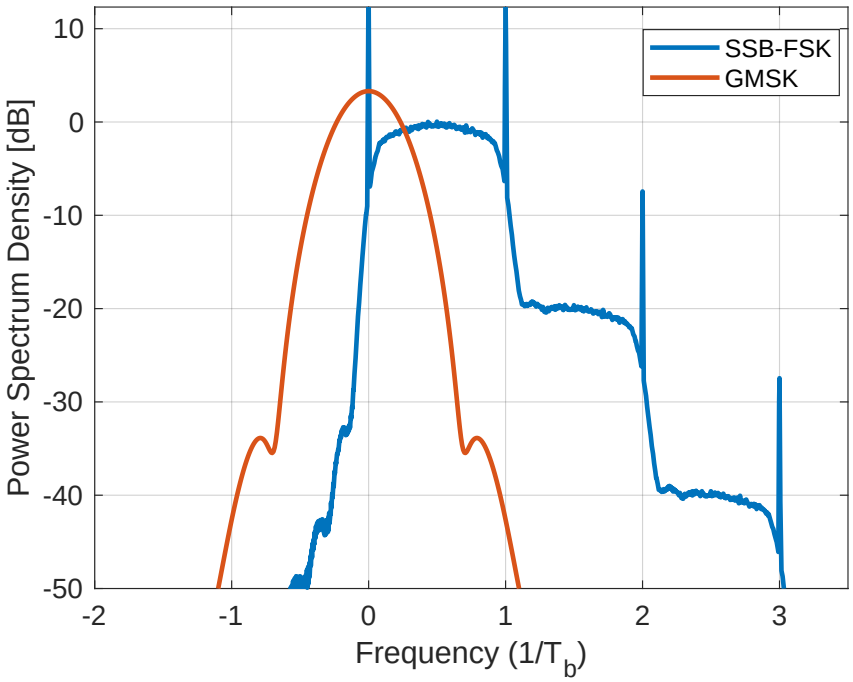

Figure 2.12 – PSD comparison between SSB-FSK with $L = 12$, $w = 0.37$ and $h = 1$ and GMSK with $BT = 0.3$.

Table 2.1 – Bandwidth occupancy (99%).

SSB-FSK			
L	2	4	12
BW	1.92	1.7	1.52

2.5.2 SSB-FSK bit error rate (BER) performance

Since SSB-FSK is also a CPM signal (1.2), it can also be represented in recursive form with the phase signal $\phi(t,\alpha)$ expressed as

$$\begin{aligned}\phi(t,\alpha) = &\underbrace{\tilde{h}\pi \sum_{i=-\infty}^{n-L} \alpha_i}_{\theta_n} + \underbrace{2\pi\tilde{h} \sum_{i=n-L+1}^{n} \alpha_i \phi_0(t - iT_\mathrm{s})}_{\theta(t,\alpha_n)}, \\ &nT_\mathrm{s} \leq t \leq (n+1)T_\mathrm{s}.\end{aligned} \tag{2.16}$$

Similar to Section 1.3.1.1, $\theta(t,\alpha_n)$ and θ_n are the $M^{(L-1)}$ correlative state vectors and the $\tilde{p}$ phase states, respectively. The number of phase states $\tilde{p}$ is computed from the modified modulation index $\tilde{h} = 2v/\tilde{p}$. Accordingly, the total number of states in the trellis for SSB-FSK modulation is given by

$$N_\mathrm{s} = \tilde{p}M^{L-1}. \tag{2.17}$$

Fig. 2.13 presents the phase tree diagram for the binary SSB-FSK with $L = 4$, $w = 0.37$, and $h = 1$ over the interval $[0, 6T_s]$. Due to the use of only positive symbols, the negative phase part is absent. The 8-state trellis is illustrated in Fig. 2.14. Since $\tilde{h} = 2$, the number of phase states $\tilde{p}$ is equal to one. Therefore, the phase states θ_n is always equal to zero.

In Fig. 2.15, we present the BER curves for SSB-FSK with $w = 0.37$ and $h = 1$ for different pulse lengths $L = 4, 12$. Moreover, the BER curve for GMSK is also plotted for comparison. The BER curves for the SSB-FSK were obtained using the MLSE optimum receiver explained in Section 1.3 using the SSB-FSK recursive form (2.16). The SSB-FSK bounds were obtained using the union bound and the minimum Euclidean distance from the method presented in Section 1.4.1. Due to the use of only positive (negative) symbols

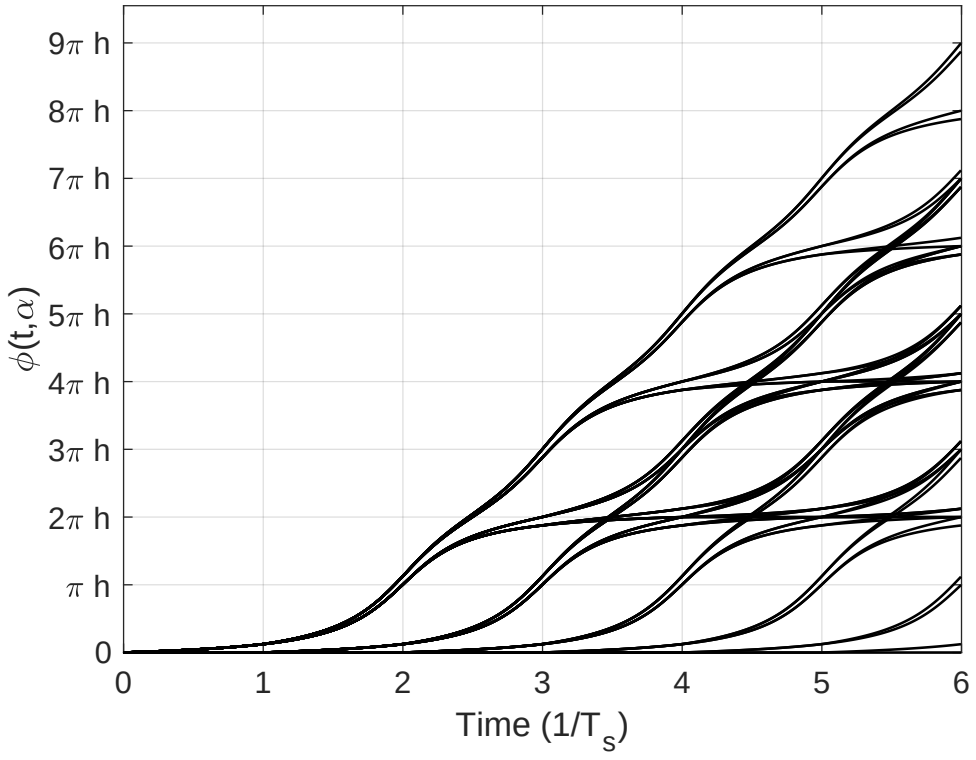

Figure 2.13 – Phase tree diagram for the binary SSB-FSK with $L = 4$, and $w = 0.37$.

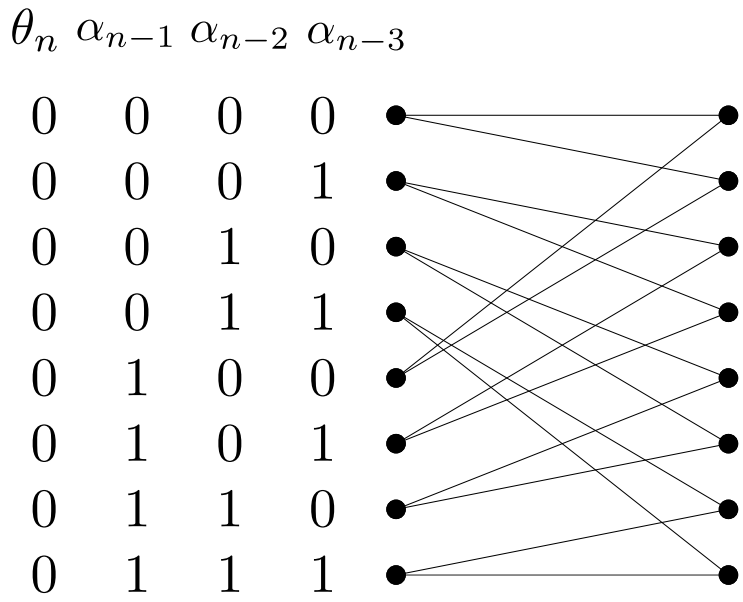

Figure 2.14 – The state trellis diagram for the binary SSB-FSK with $L = 4$, $w = 0.37$, and $h = 1$.

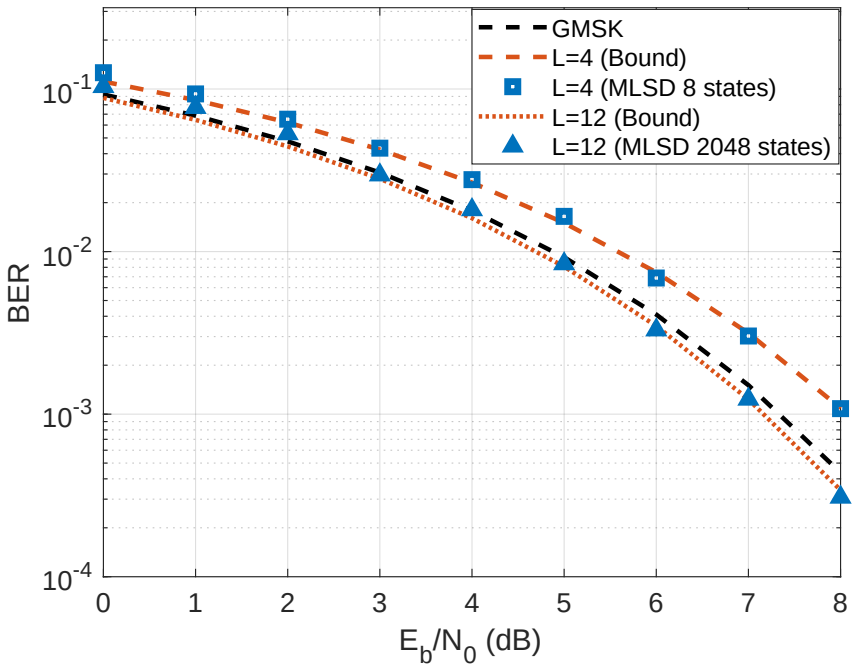

Figure 2.15 – BER comparison of binary SSB-FSK ($w = 0.37$, $h = 1$ and for $L = 4, 12$) and GMSK.

α_i, the best difference sequence γ is modified to [33]

$$\gamma_i = \begin{cases} 0 & i < 0 \\ 1, 2, \ldots, (M-1), & i = 0 \\ 0, \pm 1, \pm 2, \ldots, \pm(M-1), & 0 < i < m+1 \\ 0 & i \geq m+1 \end{cases}, \tag{2.18}$$

given that

$$\sum_{i=0}^{m} \gamma_i = 0. \tag{2.19}$$

We can observe that increasing the pulse length L decreases the BER, where for $L = 12$, we achieved a better BER performance in comparison to $L = 4$. We can explain this performance difference from Fig. 1.7, where we showed that increasing the L will increase the minimum Euclidean distance for some modulation indices, and consequently, we obtained a better performance bound. For the two different simulated SSB-FSK schemes,

the MLSD optimal receiver curves and the bound are quite similar for all different SNRs. Therefore, we can claim that the minimum Euclidean distance is the right metric to adopt in order to depict the bit error probability performance for the SSB-FSK. The GMSK and the SSB-FSK with $L = 12$ have a similar BER performance, but with $L = 12$ performing VA requires 2048 states for SSB-FSK compared to only 16 for GMSK [57]. The SSB-FSK with $L = 4$ has the lowest number of states (ie 8), but also the highest BER.

2.6 Single sideband-inspired CPM signal formulation for optimal detector complexity reduction

In this section we show that when a regular CPM signal is formatted in the same way as the SSB-FSK with respect to its particularities, two significant consequences follow:

1. the number of states needed to perform the Viterbi [22] algorithm ensuring ML detection is divided by 2,
2. the spectrum occupied by the modified signal is shifted by a frequency deviation, which is predictable and quantifiable.

First, let us introduce $s_b(t, \alpha)$ a rewriting of any conventional CPM signal in a way that we could retrieve the same initial assumptions considered for the SSB-FSK signal representation (2.11). Hence, the signal $s_b(t, \alpha)$ is given by

$$\begin{aligned} s_b(t, \alpha) &= e^{j2\pi\tilde{h}\sum_{i=-\infty}^{+\infty}\alpha_i q(t-iT_\mathrm{s})} \\ &= \underbrace{e^{j2\pi h\sum_i \tilde{\alpha}_\mathrm{i} q(t-iT_\mathrm{s})}}_{s_1(t,\tilde{\alpha})}\underbrace{e^{j2\pi h\sum_i (M-1)q(t-iT_\mathrm{s})}}_{s_2(t)}, \end{aligned} \tag{2.20}$$

where $\tilde{\alpha}_i = 2\alpha_\mathrm{i} - (M-1)$ (e.g., for binary case $\tilde{\alpha}_i \in \{-1, 1\}$), and $q(t)$ is the phase response (see Chapter 1). According to (2.20), the new baseband expression $s_b(t, \alpha)$ of any regular CPM signal could be viewed as a product of two independent signals: $s_1(t, \tilde{\alpha}_i)$, directly depending on the antipodal information bits $\tilde{\alpha}_i$, which can be seen as any regular CPM signal (Chapter 1, equation (1.1)), and $s_2(t)$ a *deterministic* signal that does not carry any information.

2.6.1 Consequence on the optimal ML detector complexity

Assuming an additive white Gaussian noise (AWGN) channel, the complex baseband representation of the received signal is

$$r(t) = s_b(t, \alpha) + n(t), \tag{2.21}$$

where $n(t)$ is a complex baseband AWGN with zero mean and power spectral density N_0. Since $s_b(t, \alpha)$ is rewritten in the same way as a SSB-FSK signal, we can apply the same recursive representation of the phase signal utilized for the SSB-FSK modulation (2.16). Accordingly the total number of states in the trellis is given by

$$\tilde{N}_\mathrm{s} = \tilde{p} M^{L-1}, \tag{2.22}$$

which is the same number of states obtained for the SSB-FSK modulation (2.17).
Now, to notice the difference between the complexity of regular CPM schemes and the SSB-inspired signal, we need to compare the number of states of each representation. First, we have to recall that for regular CPM signals, the modulation index is given by $h = 2v/p$ (see Chapter 1, Section 1.3.1.1). Due to that, the complexity of the optimal detector, when considering all possible p phase states, is then given by the number of states

$$N_\mathrm{s} = p M^{L-1}. \tag{2.23}$$

Now, when considering the SSB-inspired signal representation, the equivalent modulation index is given by $\tilde{h} = 2h = 2 \times 2\frac{v}{p} = \frac{2v}{\tilde{p}}$, with $\tilde{p} = p/2$. Consequently, thanks to this reformulation, the equivalent complexity of the optimal ML detector is now a function of the parameter $\tilde{p}$, hence it is divided by 2 as given by the equivalent number of states $\tilde{N}_\mathrm{s}$ (2.22).
Fig. 2.16 presents the trellis diagram of GMSK for regular ($s_1(t, \tilde{\alpha})$) and SSB-inspired ($s_b(t, \alpha)$) CPM. With the new representation, we can observe a fewer states (8 in comparison to 16), hence a lower receiver complexity.

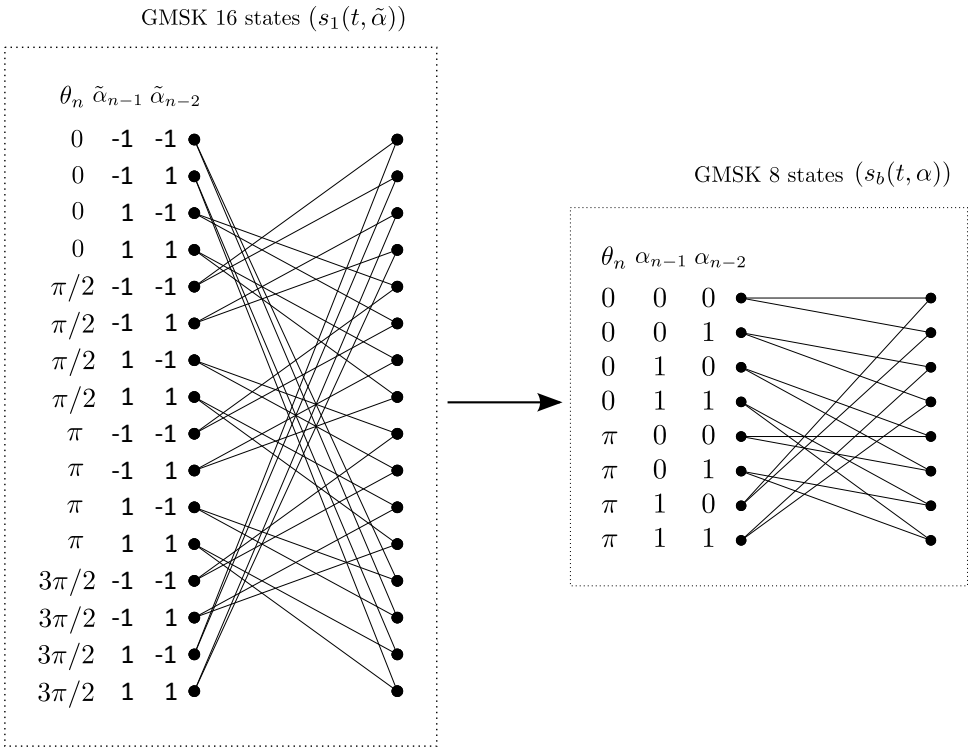

Figure 2.16 – Trellis diagrams for regular and SSB-inspired GMSK.

2.6.2 Consequences on the spectrum

In this section, we apply the same numerical method established in Section 1.4.2, to compute the power spectral density (PSD) and, consequently, analyze the CPM signals' spectrum. The original SSB spectrum of the SSB-FSK scheme, as illustrated by the PSD given in Fig. 2.7 ($h = 1$, $w = 0.37$ and $L = 12$) , follows from three primary assumptions:

— the Lorentzian frequency pulse,
— the non antipodal coding at the symbol level,
— the integer value of the modulation index h.

Therefore, the immediate side effect of SSB-inspired signal representation of any regular CPM scheme is a frequency shift of the signal spectrum at the right side with respect to the carrier frequency, since one or more of the assumptions requested for an SSB spectrum is not respected (see Fig. 2.20 and Fig. 2.21).
To better understand from where this frequency shift appears, we need first to look into (4.1). We can notice that the deterministic signal $s_2(t)$ can be rewritten as a carrier

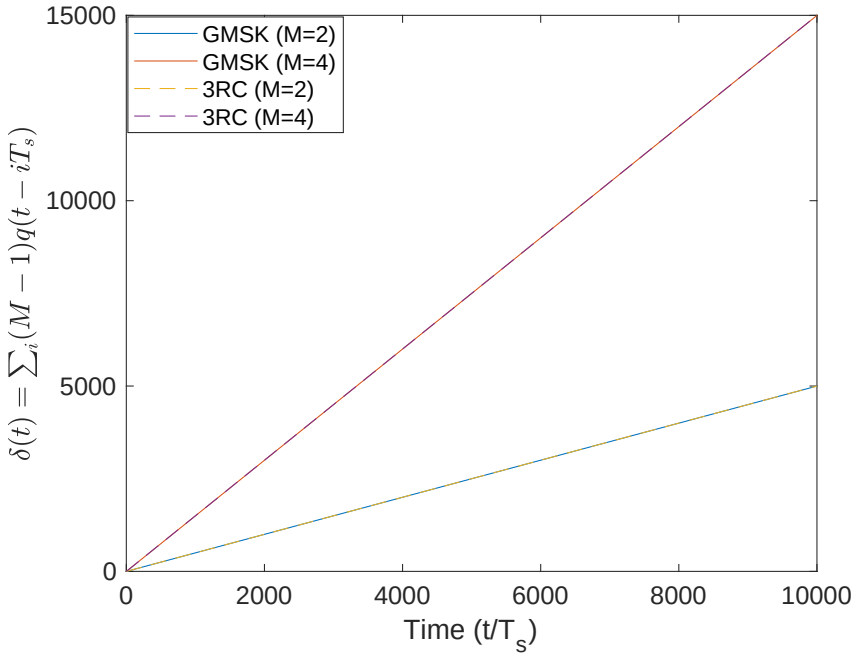

Figure 2.17 – The illustration of $\delta(t)$ for different CPM schemes (GMSK, 3RC), with different modulation levels $M = \{2, 4\}$.

frequency, with a frequency equal to Δ:

$$s_2(t) = e^{j2\pi h \overbrace{\sum_i (M-1)q(t-iT_s)}^{\delta(t)}} = e^{j2\pi\Delta t}. \tag{2.24}$$

In Fig. 2.17, we present the plot of the function $\delta(t)$ form (2.24) for different CPM schemes (GMSK, 3RC), with different modulation levels $M = \{2, 4\}$. It is evident that $\delta(t)$ is always a linear function passing through the origin. Therefore, we can represent $\delta(t)$ in the form :

$$\delta(t) = at, \tag{2.25}$$

where a is the slope. Consequently, $s_2(t)$ can be represented in the form $e^{j2\pi\Delta t}$, where $\Delta = 2\pi\tilde{h}a$.

2.6.3 Simulation results

The main objective of the present section is twofold: i) to validate the principle of optimal ML detector complexity reduction, based on the Viterbi algorithm presented in Section 2.6.1, and ii) to illustrate the side effect consisting of a frequency shift in the spectrum of the transmitted signal. In both figures 2.18 and 2.19, we evaluate the performance of the reduced complexity ML detector based on the SSB-inspired signal representation in terms of Bit Error Rate (BER) with respect to the original ML detector, for both GMSK and 3RC ($h = 3/4$) schemes, respectively. The principle of ML detection complexity reduction using the SSB-inspired representation is fully validated through both figures since the simulation curves of both original and reduced complexity detectors are identical. Each time, the optimal ML detection bound is given as a reference to verify the accuracy of our simulations. The boundary are obtained using the same method used to compute the bound for the SSB-FSK (see Section 2.5.2). In both figures 2.20 and 2.21, we plot the PSD illustrations of the transmitted signals using either the SSB-inspired representation or the original one for both GMSK and 3RC schemes, respectively. Through these figures, the frequency shift of the spectrum of the modified signal is clearly visible. However, we recall that this is not inconvenient since it is totally predictable at the receiver side from the analytical expression Δ.

Remark:

In [55], Rimoldi presented the tilted-phase CPM similar to the reformulation we presented in (2.20). The tilted-phase CPM provides an equivalent complexity reduction to the method we showed. However, the study inspired by the SSB-FSK scheme shows a more straightforward explanation of the effect of such reformulation on the receiver complexity. Besides, we can deduce that the SSB-FSK scheme is a tilted-phase CPM that does not require any additional treatment in contrary to regular CPM schemes.

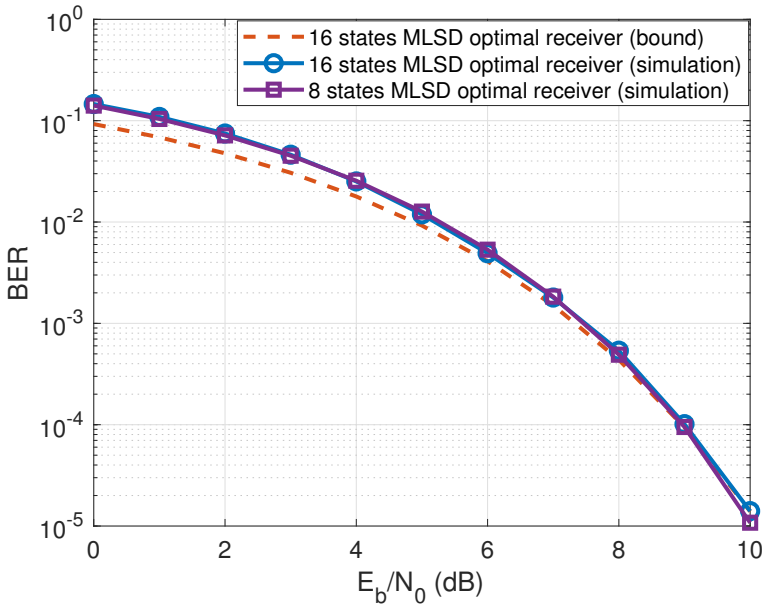

Figure 2.18 – BER performance of the reduced complexity ML detector compared to the original one for GMSK scheme.

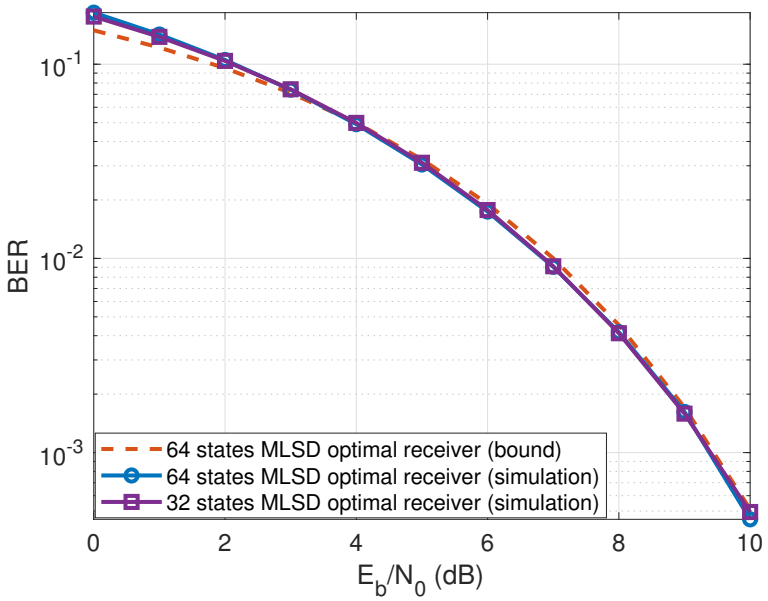

Figure 2.19 – BER performance of the reduced complexity ML detector compared to the original one for 3RC scheme.

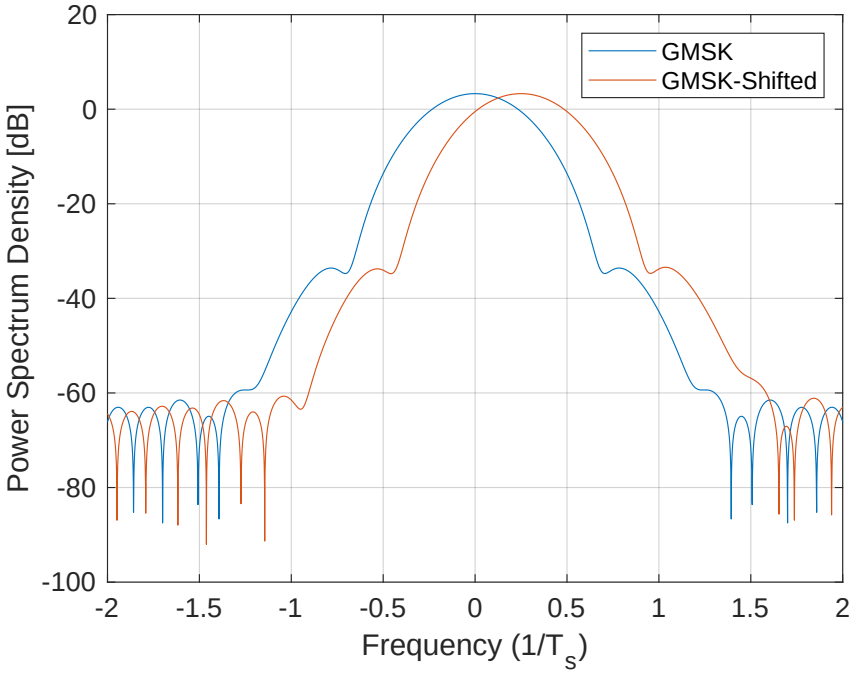

Figure 2.20 – PSD illustration of the transmitted signal using the SSB-inspired representation compared to the original one for GMSK scheme.

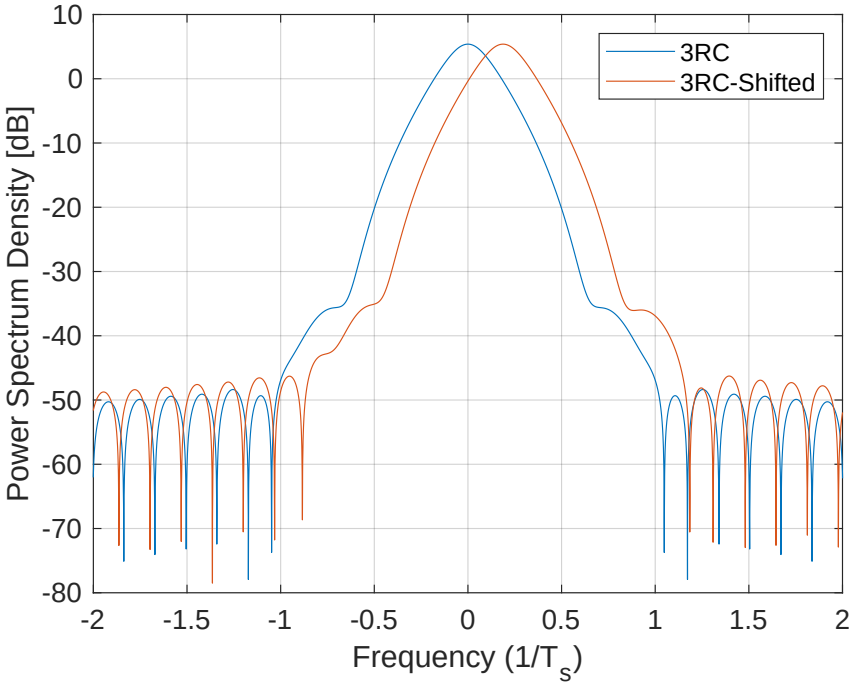

Figure 2.21 – PSD illustration of the transmitted signal using the SSB-inspired representation compared to the original one for 3RC scheme.

2.7 Conclusion

In this chapter, we presented a single side band waveform which remains a CPM modulation. We explained the origin of the idea derived from quantum physics, and we provided the signal model followed by the analytical expression of the signal spectrum for the specific integer modulation index case. In addition, spectrum and BER comparisons between SSB-FSK and GMSK are also presented. The MLSD optimum receiver used to obtain the BER was investigated using different SSB-FSK pulse lengths L values to evaluate its potential. In this chapter, the parameters for the SSB-FSK were already fixed from the state of the art. However, thus parameters were not selected based on any optimization study, where the state of the art focuses on the SSB-FSK spectrum property and not on the performance (BER, bandwidth occupancy). Therefore, we observed that the GMSK provides better performance compared to SSB-FSK. To fully exploit the potential of the SSB-FSK signals, in the next chapter, we will focus on designing SSB-FSK modulation with reasonable tradeoffs between performance and complexity while trying to maintain the SSB property. Separately, in the last section we also presented a method to reduce the complexity of the ML detector of regular CPM schemes through rearranging the transmitted signal in the same way used to define the SSB-FSK signal. Alongside the effect on the ML detector complexity, we showed the side effect impacting the signal spectrum and explained the non-inconvenient nature of this side effect, which it can be entirely predictable at the receiver side.

Chapter 3

SSB-FSK Performance Optimization

Contents

3.1 Introduction

The previous chapter presented the principle, the origins and the mathematical justification of a CPM modulation with the original feature of directly generating a SSB spectrum. However, we did not provide any result about the interplay between error probability performance, bandwidth, and SSB property. Therefore, we obtained a poor performance compared to GMSK since we only focused on the spectrum properties. Besides, CPM signals suffer from receiver complexity due to the memory property introduced by the phase continuity, which should also be considered alongside the error probability, bandwidth, and SSB property. Therefore, in this chapter, we report a complete study of the SSB-FSK performance regarding error probability, spectral efficiency, complexity, and SSB property depending on the parameters h, L, M, w, respectively. The pulse width w is a tuning parameter introduced especially for SSB-FSK, which plays an essential role in error probability and BW occupancy performance, as we will highlight in this chapter. It is worth emphasizing that we need to find a functional interplay between all these parameters, since they are leading to opposite effects on the error probability, spectral efficiency, complexity, and SSB property. Therefore, we must define practical tradeoffs between these parameters as long as an optimal scheme considering all performance metrics is impossible.
The rest of the chapter is organized as follows. In Section 3.2, we present the *Pareto optimum*, a multi-objective optimization method, which is used alongside a *brute force* method to obtain the best possible tradeoffs for the SSB-FSK scheme. In Section 3.3, we illustrate several simulation results for error probability performance, power spectrum performance, energy-bandwidth comparison, and synchronization advantage, respectively. Finally, the main outcomes of this study in terms of concluding remarks and design directives are summarized in Section 3.4. Conclusions are drawn in Section 3.5.

3.2 Multi-objective optimization

SSB-FSK has several conflicting objectives that need to be optimized, where the major challenge is to find tradeoffs for designing a competitive SSB CPM-based system. We have thus divided this section into three parts:

– Objective functions: in this part, we summarize the performance metrics considered in the optimization analysis.

– Design space: a massive number of configurations have to be tested due to the variety of parameters. Therefore, it is interesting to reduce this number of combinations by excluding situations that cannot be envisaged, i.e., by defining a feasible region of the optimization problem variables.
– Optimization method: as we have several objectives to optimize, different methodologies are possible. One solution is to optimize one performance metric when considering others constrained to a certain threshold (drawn from well-known other CPM schemes). Using this methodology, we define plenty of optimization problems (as many as possible combinations between considered objective functions and fixed thresholds for constrained performance metrics). Therefore, the best course of action is to jointly optimize all performance metrics by defining several intermediate configurations leading to different tradeoffs depending on the order of priority given for these objective functions.

3.2.1 Objective functions

— *Minimum Normalized Squared Euclidean Distance* ($d^2_{\min}$): it measures the energy consumption of the signals, based on the error probability bound given in (1.23). It is clear that an increase of $d^2_{\min}$ can be seen as a reduction in the mean energy per information bit E_b for the same targeted probability error.
— *Bandwidth Occupancy* (BW): it estimates the BW occupancy of the signal. We divided the BW occupancy into two measurements; the first one computes 99% of the signal power inside BT_b, where B represents the total bandwidth occupancy and not half of it due to the unsymmetrical spectrum shape form of the SSB-FSK modulation. The second measurement computes 99.9% of the power inside BT_b. With the second measurement, we obtain a better idea about the out-of-band leakage. We noted these two measurements B_{99} and B_{999}, respectively. The objective of both measurements is to estimate the BW occupancy of BT_b. We note that the bandwidth BT_b is normalized to the data rate in terms of bits carried per second so that schemes with different modulation levels M can be compared.
— *Complexity* (N_s): it is given by the number of states used to implement the MLSD receiver. The number of states N_s is computed from the equation (2.17).
— *Single-Sideband Loss* (SSB-LOSS): the SSB-LOSS is a specific objective function defined only for SSB-FSK signals (as they are the only CPM signals having this spectral feature). SSB-LOSS estimates the percentage of power loss in the lower

band (the respectively upper band for negative modulation indices h) of the PSD.

Due to the enormous computational complexity of all of these metrics, we had to establish a priority order between them. Therefore, we provided the highest priority degree to the signal energy consumption, normalized BW occupancy, and complexity, where we tried to find certain tradeoffs between these three objective functions. Based on these tradeoffs, we sequentially tried to reduce the SSB-LOSS.

3.2.2 Space design

The initial step for solving a multi-objective function is to define a feasible region for the problem. In this study, we are mainly interested in three objective functions: energy consumption, normalized BW occupancy, and complexity. Therefore, the feasible region for the constraints is discussed hereafter :

1. *Modulation index* h: it is important to keep a small h, where large h has a significant impact on the occupied BW [1, Ch. 4] [62, 42] (1.12) . Therefore, we define the modulation index range $0.01 \leq h \leq 2$, with an increment step size $h_\mathrm{s} = 0.01$. More information about the effect of h on the spectrum of SSB-FSK signals, are presented in 3.3.2.
2. *Pulse length* L: an increase in L will produce an increase in complexity (1.17) [53, ch. 4, p. 248]. Therefore, considering the values taken from the literature, L will be less than 8. [1, 57][51], where $L = 8$ is already a complex system. However, in [19], constrained by the specific slow decrease of the Lorentzian pulse, we allowed a pulse length $L = 12$ (Section 2.5). Therefore, we defined the pulse length range as $1 \leq L \leq 12$ with an increment step size $L_\mathrm{s} = 1$. We will not exceed this maximum value of $L = 12$ to not explode the receiver complexity gaining very little on the SSB property.
3. *Modulation level* M: an increase in M will create an increase in complexity (1.17) [53, ch. 4, p. 248], and a degradation in normalized BW occupancy BT_b for the same modulation index (h) [1] (Fig. 1.10). Therefore we selected M to take only discrete values $\{2, 4, 8\}$.
4. *Pulse width* w: w is a new parameter introduced by SSB-FSK. Based on [19], increasing w will impact the SSB-FSK PSD exponential decrease, which can be quantified to $\exp(-4\pi w/T_b)$ for the particular case $h = 1$ (Section 2.4.2). There-

Table 3.1 – Pulse width limit w_{lim} with respect to pulse length L for SSB-FSK.

L	2	4	6	8	10	12
w_{lim}	1.6	3.2	4.8	6.4	7.9	9.5

fore, it is worth studying the effects of the pulse width w more deeply on energy computation and normalized BW occupancy BT_{b}. To fully cover the effects of the pulse width w, we also need to define a numerical range that covers the *useful* region (a reduced set of the *feasible* region). The pulse width w can only be found in the frequency pulse expression given by (2.13). It is clear from this expression that no restriction are found to delimit the possible values of w (except that it has to be a non-zero positive real). Therefore, to cover the entire *feasible* region, we need to consider all pulses width w values, i.e., $w \in]0, \infty[$.
Consequently, we define w_{lim} as a new limit of the pulse width w, where for $w_{\text{lim}} \leq w \leq \infty$, we obtain approximately the same frequency pulse $g(t)$. Hence, it will be possible to reduce the study to $w \in]0, w_{\text{lim}}]$, which is now the *useful* region. The calculation of w_{lim} is straightforward using the *2-norm* defined as

$$||x||_2 = \sqrt{\sum_i |x_i|^2}. \tag{3.1}$$

The error is then calculated using

$$\epsilon = \frac{||\hat{x} - x||_2}{||x||_2}, \tag{3.2}$$

where x is the frequency pulse $g_\infty(t)$, for $w = \infty$ (in numerical simulation, we take $w = 1000$). Furthermore, $\hat{x}$ is the estimated frequency pulse $g_{\text{lim}}(t)$, for $w = w_{\text{lim}}$. We calculate w_{lim} for each L in the defined interval. The criteria to obtain w_{lim} from (3.2) is to maintain an error $\epsilon \leq 10^{-1}$. In Table 3.1, we present w_{lim} with respect to the pulse length L for binary SSB-FSK. Finally, we define the pulse width range $0.1 \leq w \leq w_{\text{lim}}$. It is worth noting that w_{lim} is increasing with respect to the pulse length L. Therefore, more configurations have to be considered when increasing L as the defined range of w is getting wider. Moreover, the increment step size is $w_{\text{s}} = 0.1$.

3.2.3 Optimization method (without complexity)

In multi-objective problems, there is no single global optimal solution. Therefore, *Pareto optimum* is used to find all optimal points. A solution is said to be the *Pareto optimum* (P_{opt}) if there is no other solution that can improve at least one objective function without reducing the other objective functions. The objective functions in our case are

$$F(x) = [F_1(x), F_2(x)], \tag{3.3}$$

where

$$F(x_1) > F(x_2) \iff \forall_i \, F_i(x_1) > F_i(x_2). \tag{3.4}$$

$F_1(x)$ and $F_2(x)$ are the $10\log_{10}(d^2_{\text{min}}/2)$ and the inverse of the normalized bandwidth occupancy ($1/BT_{\text{b}}$), respectively. The constraints variables (h, L, M, w) are denoted here by $x \in \mathbb{R}^4$. The definition of *Pareto optimum* is given by (we present the weak *Pareto optimum*) :

$$x^* = P_{\text{opt}} \iff \nexists \, y \text{ such that } F(y) > F(x^*). \tag{3.5}$$

For more information about the *Pareto optimum*, please refer to [38, 45]. We used a *Brute Force* method to obtain all the values of $F_1(x)$ and $F_2(x)$ for the space Z, where Z is constrained by the parameters h, L, M, w and their defined ranges. Based on this *Brute Force*, we apply the *Pareto optimum* optimization to obtain all the optimum solutions for Z.

Remarks:

— We calculate the minimum normalized squared Euclidean distance (d^2_{min}) using the algorithm introduced in Section 1.4.1. We consider all the mergers for merger index $\kappa = 3$ (the number of mergers is found by trials). Moreover, we also consider $N_{\text{max}} = 30$, where N is the number of observation symbols.

— We calculate B_{99} and B_{999} normalized BW occupancy (BT_{b}) using the method presented in Section 1.4.2. Hence, we obtain different P_{opt} for each normalized bandwidth BW occupancy BT_{b} measure.

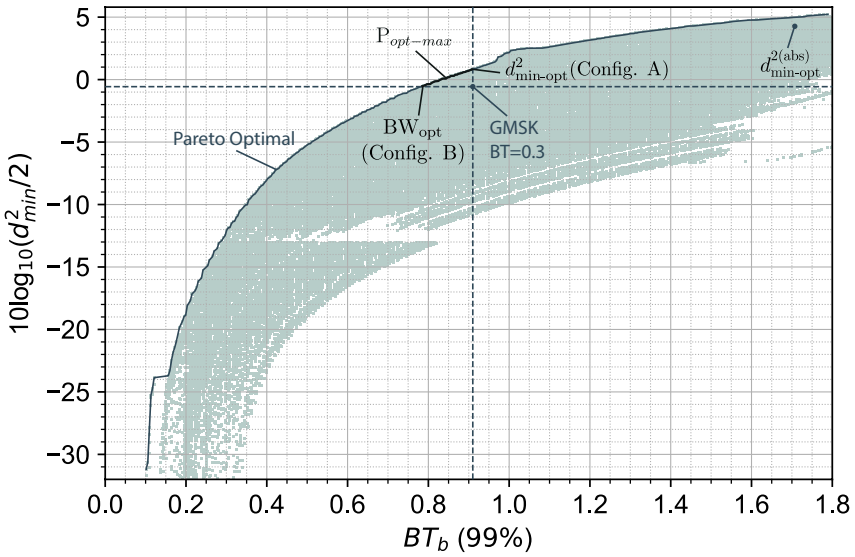

Figure 3.1 – Two objective functions Pareto optimum plot for binary LSSB-FSK using B_{99}. GMSK for $BT = 0.3$ is presented as a reference point.

Table 3.2 – SSB-FSK optimum minimum normalized squared Euclidean distance $d^2_{\text{min}-\text{opt}}$ and optimum normalized bandwidth occupancy BW_{opt} for 99% bandwidth BW occupancy, for different modulation levels M.

$\boldsymbol{d^2_{\text{min}-\text{opt}}}$ - Config. A							
M	L	w	h	d^2_{min}	BW	SSB-LOSS (%)	N
2	5	1.3	0.78	2.4	0.906	1.764	15
4	2	0.7	0.49	3.53	0.906	2.561	25
8	2	0.6	0.36	3.25	0.904	1	8
$\boldsymbol{BW}_{\text{opt}}$ - Config. B							
M	L	w	h	d^2_{min}	BW	SSB-LOSS (%)	N
2	5	1.2	0.65	1.774	0.785	2	14
4	2	0.8	0.33	1.773	0.65	2.732	10
8	2	0.6	0.26	1.8	0.677	1.21	8

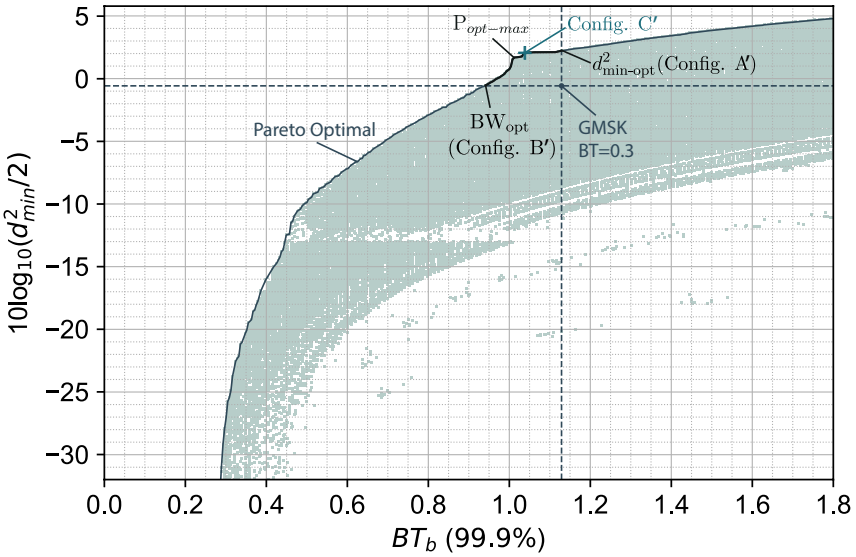

Figure 3.2 – Two objective functions Pareto optimum plot for binary LSSB-FSK using B_{999}. GMSK for $BT = 0.3$ is presented as a reference point.

Table 3.3 – SSB-FSK optimum minimum normalized squared Euclidean distance $d^2_{\text{min}-\text{opt}}$ and optimum normalized bandwidth occupancy BW_{opt} for 99.9% bandwidth BW occupancy, for different modulation levels M.

$\boldsymbol{d^2_{\text{min}-\text{opt}}}$ - Config. A′							
M	L	w	h	d^2_{min}	BW	SSB-LOSS (%)	N
2	12	0.8	1.04	3.346	1.129	0.366	18
4	2	0.7	0.44	2.98	1.25	2.611	7
8	2	0.7	0.35	3.025	1.114	0.955	8
$\boldsymbol{BW}_{\text{opt}}$ - Config. B′							
M	L	w	h	d^2_{min}	BW	SSB-LOSS (%)	N
2	6	1.1	0.67	1.773	0.941	1.683	14
4	2	0.7	0.33	1.814	0.902	2.930	8
8	2	0.6	0.26	1.8	0.902	1.214	8

Fig. 3.1 and Fig. 3.2 present the *Pareto optimum* for binary LSSB-FSK using B_{99} and B_{999}, respectively. Moreover, the GMSK performance for $BT = 0.3$ is considered here as

a reference point. Hence, for this part, we consider only the Pareto front values which have a normalized bandwidth BW occupancy that is less than or equal to the GMSK bandwidth BW occupancy and a minimum normalized squared Euclidean distance d^2_{min} greater than or equal to the GMSK distance d^2_{min}. These values are illustrated in the upper left quarter of the plane delimited by the GMSK reference point's axis in Fig. 3.1 and Fig. 3.2. We will refer to these values as $P_{\text{opt}-\text{max}}$. In Fig. 3.1, $P_{\text{opt}-\text{max}}$ is achieved with 26 different configurations (parameter combinations). In Fig. 3.2, $P_{\text{opt}-\text{max}}$ is achieved with 29 different configurations. Note that each point of $P_{\text{opt}-\text{max}}$ corresponds to a particular configuration, and the number of configurations depends on the parameters step used in the search $(L_{\text{s},W_\text{s}}, h_\text{s})$.

Table 3.2 and Table 3.3 present the optimum minimum normalized squared Euclidean distance $d^2_{\text{min}-\text{opt}}$ and optimum normalized bandwidth occupancy BW_{opt} for 99% and 99.9% occupancies, respectively, as a function of the SSB-FSK parameters for different modulation levels M. Considering only the $P_{\text{opt}-\text{max}}$ configurations, we have $d^2_{\text{min}-\text{opt}}$ and BW_{opt} as the highest minimum normalized squared Euclidean distance d^2_{min} (higher d^2_{min} means lower energy consumption), and the lowest normalized bandwidth (BW) occupancy values obtained respectively. These points are denoted by Config. A (for $d^2_{\text{min}-\text{opt}}$) and Config. B (for BW_{opt}) for B_{99} (Config. A' and Config. B' according to B_{999}). Besides, we also show the number of observation symbol intervals N needed (the Viterbi algorithm memory highly depends on N) and the SSB-LOSS generated. The *Pareto optimum* analysis (Fig. 3.1 and Fig. 3.2) gives all possible tradeoffs combining both normalized minimum Euclidean distance d^2_{min} (y-axis, $10\log_{10}(d^2_{\text{min}}/2)$) and normalized bandwidth occupancy metrics (x-axis). Table 3.2 and Table 3.3 give absolute optimum values, performing better than the GMSK, for each performance metric *alone* and the resulting effect on the other one. Furthermore, in Fig. 3.2, we can see that the normalized minimum Euclidean distance d^2_{min} performance has a small variation between Config. A$'$ and Config. C$'$ (the line is quite horizontal). Therefore, Config. C$'$ seems an interesting point (another good tradeoff) since it offers almost the same normalized minimum Euclidean distance d^2_{min} while significantly decreasing the normalized bandwidth BW occupancy. Config. C$'$ corresponds to the following parameters combination ($L = 12$, $w = 0.7$, $h = 0.99$); leading to $d^2_{\text{min-C'}} = 3.216$, $BW_{\text{C'}} = 1.043$.

3.2.4 Optimization method (with complexity)

In this part, we consider three objective functions for optimization: $10\log_{10}(d^2_{\min}/2)$, the inverse of the normalized bandwidth occupancy ($1/BT_{\mathrm{b}}$), and the number of states (N_{s}), which represents the complexity. Similar to Section 3.2.3, we apply the *Pareto optimum* optimization with the three selected objective functions to obtain all the optimum solutions for the space S. Unlike Z, the space S presents only the configurations with a number of states $N_{\mathrm{s}} \leq 64$ (a system with $N_{\mathrm{s}} > 64$ is considered to be very complex). Moreover, in order to ensure better performance than GMSK, the configurations in space S can have energy ($10\log_{10}(d^2_{\min}/2)$) values higher or equal to the GMSK energy minus "0.1", and a normalized bandwidth occupancy BW lower or equal to GMSK BW plus "0.1".

In Fig. 3.3 and Fig. 3.4, we illustrate the configurations obtained from the three objectives *Pareto Optimum* optimization, respectively, for B_{99} and B_{999}. Each configuration is presented by the x-axis (the normalized BW occupancy), the y-axis (the energy ($10\log_{10}(d^2_{\min}/2)$)), and the z-axis (the complexity (N_s)). The z-axis is illustrated using markers, where each different marker presents a particular N_{s} value. Since we have many configurations (25 for B_{99} and 22 for B_{999}) and some of the configurations have similar performance (energy and BW), we decided to divide the configurations into clusters based on their performance similarity. And then from each cluster, we selected only one configuration. To obtain the clusters, we applied the *k-means* algorithm [25, ch.14, p.509] with Euclidean distance as cost function on the configurations obtained, taking into consideration only the energy and normalized BW occupancy of each configuration. Using the *k-means*, we obtained four and five different clusters, respectively, for B_{99} and B_{999}. Based on the clusters obtained, we selected one configuration representing the cluster based on two conditions:

1. Since all configurations in the same cluster have approximately similar performance, we prioritized the complexity (N_s). Therefore, we selected the configuration with the lowest complexity as the cluster representative.

2. Suppose two or more configurations in the same cluster have the same minimum complexity (N_s). In that case, we select the configuration with the maximum performance, measured as $10\log_{10}(d^2_{\min}/2) - BT_b$, giving the same weight to bandwidth occupancy BW and energy performance.

In figures 3.3 and 3.4, the selected configurations are presented with an index number.

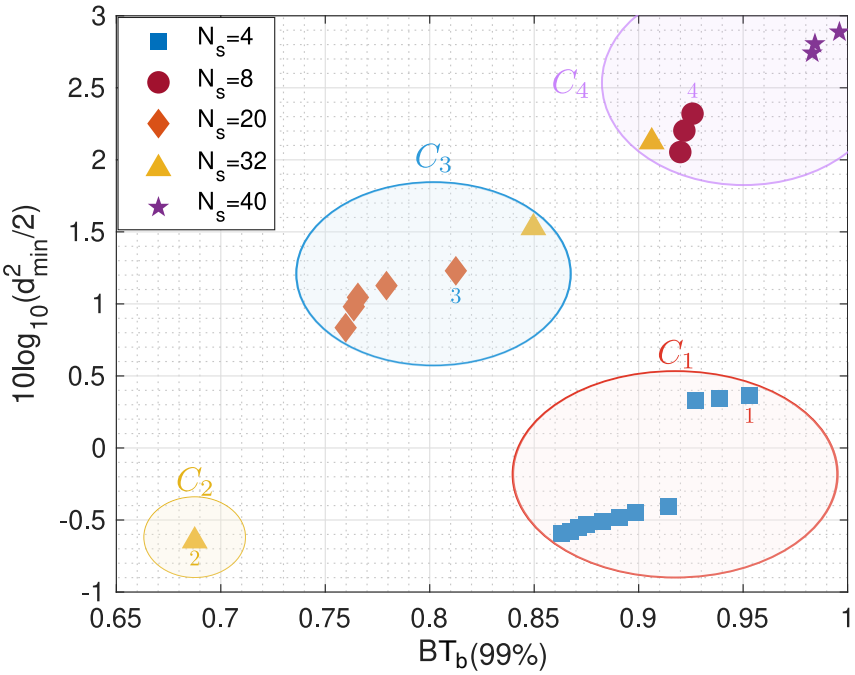

Figure 3.3 – Three Pareto optimum objective functions configurations for LSSB-FSK using B_{99}.

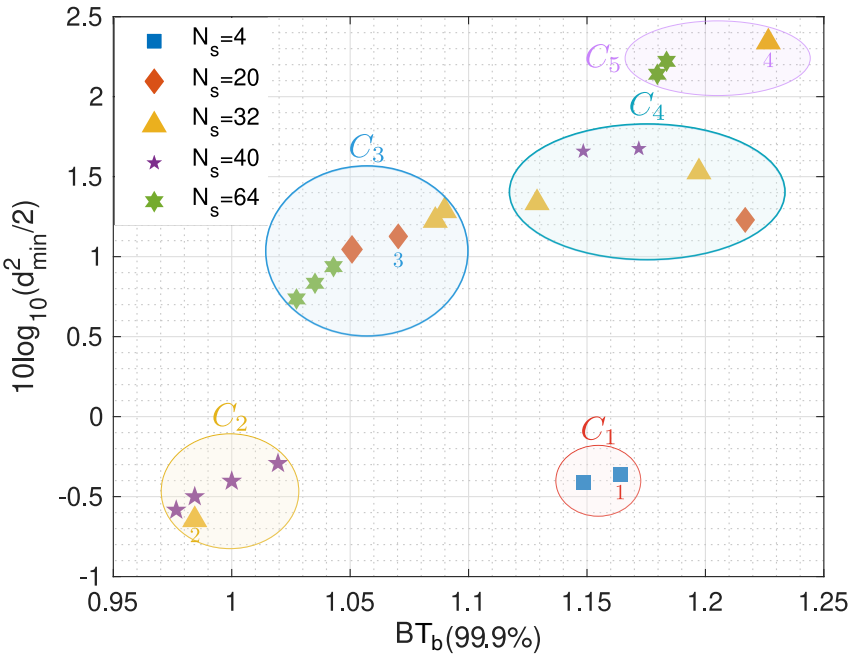

Figure 3.4 – Three Pareto optimum objective functions configurations for LSSB-FSK using B_{999}.

The index number presents the row in Table 3.4 and Table 3.5, respectively, for 99% and 99.9% normalized BW occupancy. Given later, these tables illustrate the parameters and the performance of the selected configurations. The results from these tables will be discussed in Section 3.3, for the sake of comparison as they are presented alongside other relevant results from other known CPM schemes.
In Fig. 3.4, we can see that we select only four configurations out of five, where configuration number 3 offers a remarkably better normalized BW occupancy than the configuration selected from the fourth cluster while maintaining almost the same energy performance (a slight difference of 0.1 dB). Therefore, we ignore the configuration from the cluster number 4.

3.3 Simulation results

This section presents the results obtained based on Section 1.4.1, 1.4.2, and 3.2. As this section is dedicated to illustrate SSB-FSK performance considering many metrics varying many parameters. We have chosen to do it sequentially for the sake of simplicity. Indeed, we first evaluate each metric separately and quantify the impact of all parameters on it: error probability performance in terms of $d_{\min}$ is reported in sub-section 3.3.1, and power spectrum performance is depicted in subsection 3.3.2. Second, we start to stack metrics together and evaluate performance when considered jointly: the interplay between $d^2_{\min}$ and BW is presented in sub-section 3.3.3. By taking further the complexity into account, new tradeoffs are revealed in sub-section 3.3.3. Finally, when synchronization advantage is suggested through the use of exclusively integer modulation indices, simulation results are given in sub-section 3.3.4, demonstrating the superiority of the SSB-FSK scheme among well-known CPM schemes.

3.3.1 SSB-FSK CPM error probability performance

Section 1.4.1 describes the effect of the parameters h, M, L on $d^2_{\min}$ for a variety of CPM schemes; the SSB-FSK is a pretty similar scheme compared to the ones presented in Section 1.4.1 (*unlimited time* CPM schemes with a symmetrical form with respect to zero). However, the pulse width w is a specific parameter introduced particularly for SSB-FSK signals. Therefore, it is interesting to study its effects on the $d^2_{\min}$.

Fig. 3.5 depicts the variations of the upper bound d^2_{B} as a function of the modulation index h for binary 5SSB-FSK, for pulse width $w = 0.1, 0.3, 0.5, 0.7, 0.9, 1.1, 1.3$. Consequently, we can quantify the double effect of both parameters h and w on the error probability performance of SSB-FSK, which are presented in three points:

— We obtain a better upper bound d^2_{B} using a narrow pulse width w, e.g., $w = 0.1$ for low modulation index region h, e.g., for $h \approx 0.5$. Therefore, for small modulation index h, it is always better to use small pulse width w.

— We show that for higher modulation index h, a higher pulse width w is preferred, e.g., for $h \approx 1.5$, we obtain the best d^2_{B} for $w = 1.3$. This behavior is very similar to the effect of increasing the pulse length L, which is explained in detail in [1, ch.3, p.75-76].

— In contrast to the second point, it is not always better to use higher pulse width w for higher modulation index h, where we notice that d^2_{B} with $w = 0.9$ is better than $w = 1.3$, for the same $h \approx 1.9$.

Based on the previous points, we cannot draw a general trend for the effects of the pulse width w on the upper bound d^2_{B} performance.
Besides, the impact of pulse width w on the upper bound d^2_B can be seen directly from Fig. 2.11, where it is evident that the tails of the frequency pulse $g(t)$ go up with the increase of pulse width w, which means an increase in inter-symbol interference (ISI). Fortunately, when the ISI is appropriately compensated at the receiver side, this can increase the redundant information (increase in memory effect). Hence, this introduces sizable gains in the upper bound d^2_B values.

Fig. 3.6 illustrates the performance of minimum normalized squared Euclidean distance d^2_{min} as a function of h for binary 5SSB-FSK with pulse width $w = 1.3$. This configuration ($L = 5$ and $w = 1.3$) is chosen related to the *Pareto optimum* analysis results given in the previous Section (it is Config. A also given in Table 3.2 row 1). Moreover, the results are illustrated for different observation symbol intervals $N = 5, 10, 15, 30$. In addition, the GMSK is also shown as x mark, and the $d^2_{\mathrm{min-opt}}$ for binary B_{99} SSB-FSK (Table 3.2 row 1 or Config. A in Fig. 3.1) is also shown as a reference point. Fig. 3.6 shows that the most significant d^2_{min} value slightly higher than 5 can be reached, for $h = 1.61$ and $N = 30$: this is almost the absolute optimum without considering any other metric, and it is denoted by $d^{2\,(\mathrm{abs})}_{\mathrm{min\text{-}opt}}$ (this is visible in Fig. 3.1, it is one of the extreme points at the upper right quarter of the plane). Compared to GMSK, we obtained a gain of roughly 4.83 dB. Note that this configuration, leading to $d^{2\,(\mathrm{abs})}_{\mathrm{min\text{-}opt}}$, offers very poor BW performance (this is also visible

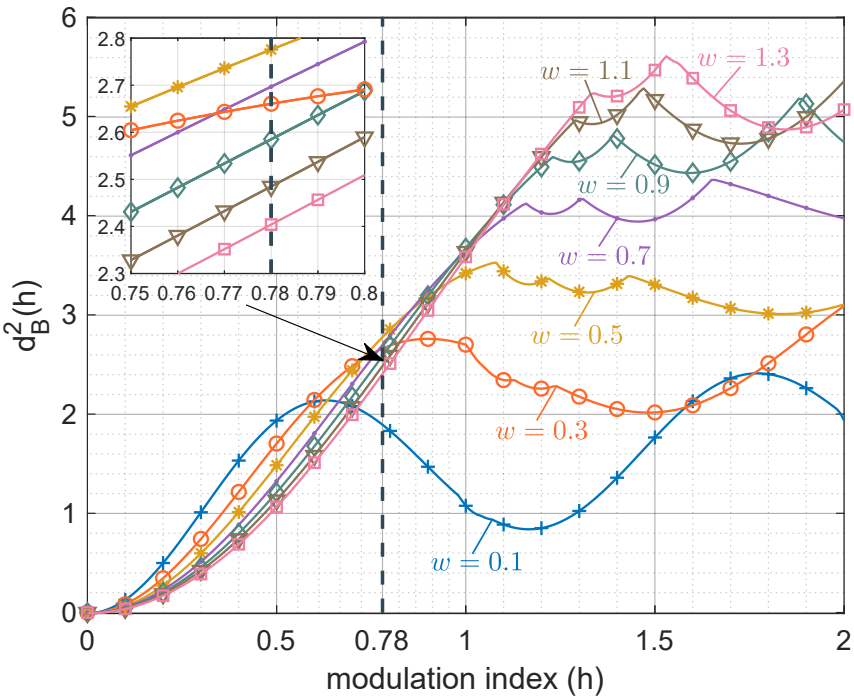

Figure 3.5 – Effect of pulse width w on the upper bound (d_B^2) as a function of modulation index h for binary 5SSB-FSK.

in Fig. 3.1). That is why in Table 3.2, we have chosen the modulation index $h = 0.78$ (Config. A), which is shown as a reference point in the figure. This result, which is different from $d^{2\,(\text{abs})}_{\text{min-opt}}$, is obtained because we consider the normalized bandwidth BW occupancy alongside the minimum normalized squared Euclidean distance d^2_{min}. We can notice the decrease of modulation index h (from $h = 1.61$ to $h = 0.78$), resulting in a smaller normalized bandwidth BW occupancy. As a consequence, the energy consumption gain compared to GMSK decreases to 1.36 dB. We can also observe that, for certain specific modulation indices h, d^2_{min} cannot reaches the upper bound d_B^2, especially for modulation index $h = 3/2$. This effect appears for all CPM schemes, called weak modulation indices, and it was previously presented in Section 1.4.2, in Fig. 1.9.

3.3.2 SSB-FSK CPM power spectrum performance

Similar to Section 3.3.1, the parameters' effects are already detailed . Therefore, we present only the effect of parameter w on the PSD of the SSB-FSK signals. Moreover, in this section, we also present the effect of h on the SSB-LOSS.

Fig. 3.7 illustrates the PSD of binary 5SSB-FSK for different pulse width $w = 0.3, 0.7, 1.3$

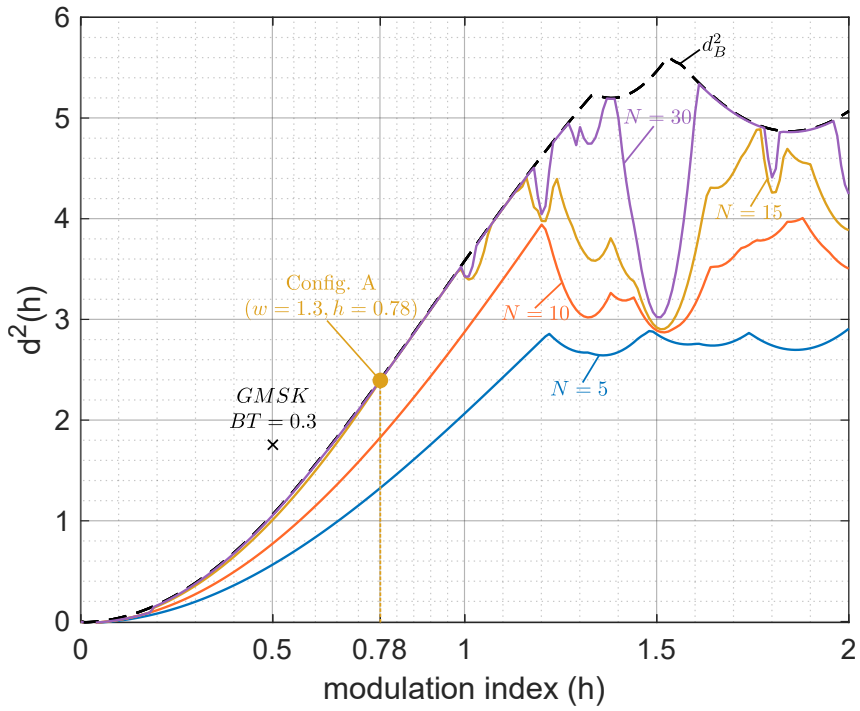

Figure 3.6 – Minimum normalized squared Euclidean d^2_{min} distance as a function of modulation index h for binary 5SSB-FSK with $w = 1.3$.

as a function of the frequency, with $h = 0.78$. The choices of the parameters ($L = 5$ and $w = 1.3$) are based on the first row of Table 3.2 (Config. A in Fig. 3.2), also used in Fig. 3.5 and Fig. 3.6 to depict the effects of the pulse width w on the d^2_{min}.
In this part, we show the effects of the pulse width w on the PSD. To clarify the selection of pulse width $w = 1.3$ in our optimization solution, we added to Fig. 3.7 two more plots for different pulse widths $w = 0.3, 0.7$. The effect of the pulse width w on the PSD is summarized in these three points:

— Increasing w accentuates the exponential decay of the SSB-FSK PSD. [20] (Section 2.4.2).
— Increasing the pulse width w narrows the power spectral density, particularly in the frequency interval of width $1/T_s$, which is primarily evident when we compare the plots of pulse width $w = 0.3$ and the others.
— Based on the closeup figure made around $h = 0.78$ in Fig. 3.5, we can see that increasing w, in this particular region, does not decrease d^2_B that much (consequently d^2_{min}).

From these observations, it is clear that increasing the pulse width w reduces the normal-

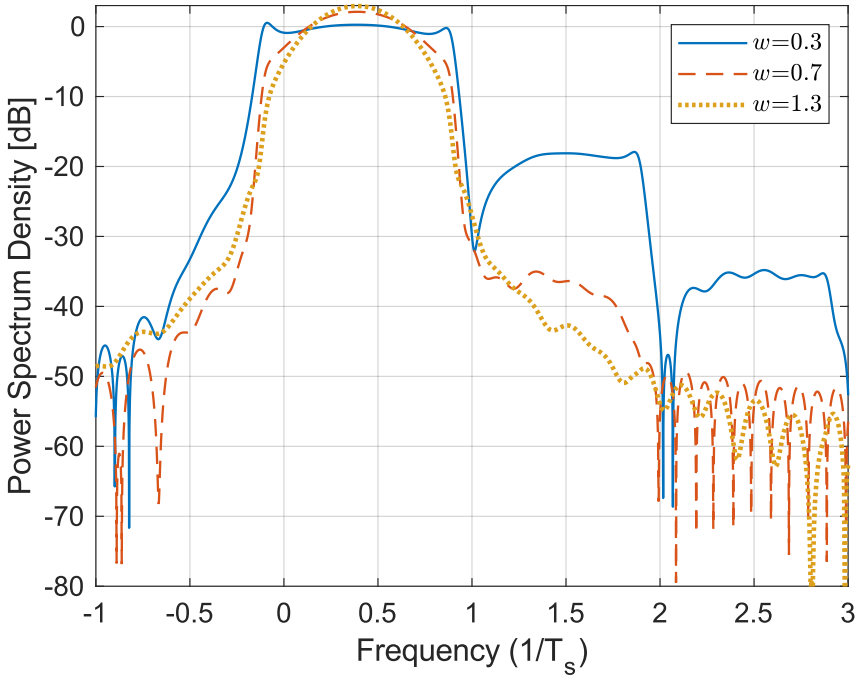

Figure 3.7 – Power spectral density of binary 5SSB-FSK with $h = 0.78$ and for $w = 0.3, 0.7, 1.3$

ized bandwidth BW occupancy, improves the adjacent-channel interference, and maintains approximately the same d^2_{min}, based on the modulation index h selected.
In general, we cannot increase the pulse width w indefinitely. For instance, from Fig. 3.5, we can see that increasing the pulse width w reduces d^2_{min}, especially for low modulation index h. Accordingly, the choice of parameters is a trade off aiming to optimize not only d^2_{min}, but also the normalized bandwidth BW occupancy.

Fig. 3.8 represents the PSD of the binary 12SSB-FSK, for $w = 0.8$ and different $h = 0.5, 0.8$ and 1.04. In this part, we show the effect of the modulation index h on the SSB-LOSS. As in the previous part, we used the parameters obtained from the optimization Section 3.2, i.e., the first row from Table 3.3, which corresponds to Config. A′ in Fig. 3.2 (the result of the *Pareto optimum* for B_{999}). In this particular context, we notice that we obtain the lowest SSB-LOSS. It is evident that increasing the modulation index h increases the normalized bandwidth BW occupancy. It is especially visible for the frequency region between 0 and $1/T_s$. On the other hand, the modulation index h has the inverse effect on the SSB-LOSS: for $h = 0.5$, we obtain an SSB-LOSS of 2.06%, and for $h = 0.8$, the SSB-LOSS decreases to 1.63%, and then for $h = 1.04$ it reached the lowest value with an SSB-LOSS of 0.366%. However, for different parameters, e.g., 6SSB-FSK and pulse width

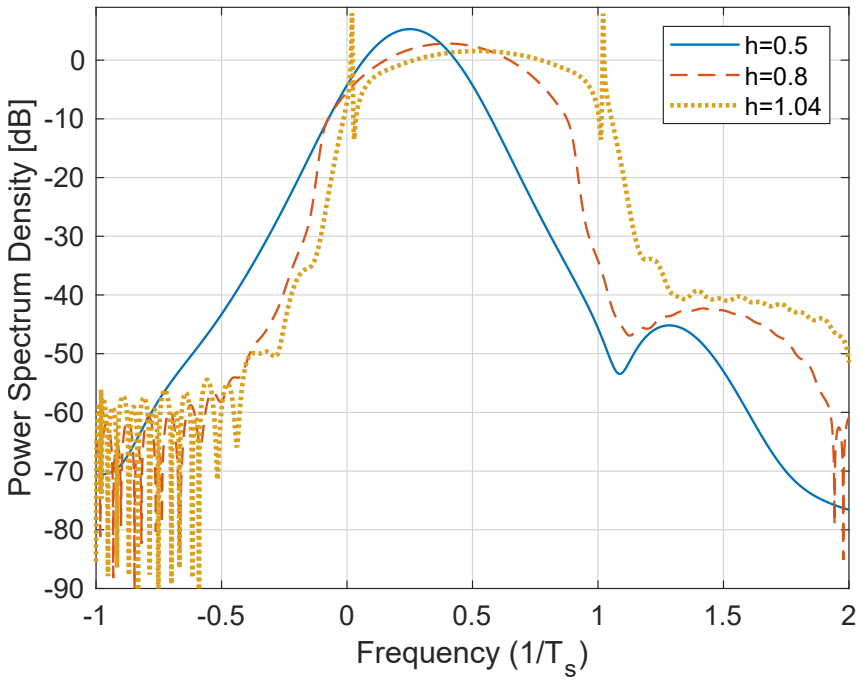

Figure 3.8 – Power spectral density of binary 12SSB-FSK with $w = 0.8$ and $h = 0.5, 0.8, 1.04$.

$w = 0.37$, increasing the modulation index will increase the SSB-LOSS. Therefore, it is impossible to generalize the effect of the modulation index h on the SSB-LOSS. Otherwise, it is always true that taking an integer modulation index h will reduce the SSB-LOSS; this decrease is due to the spectral lines, which take a part of the transmitted power. This observation is due to selecting a modulation index h around an integer (≈ 1). Even if these spikes seem undesirable because a part of the transmitted power is wasted, they could be of great interest for synchronization purposes [1, Ch. 9, Sec. 1][61].

3.3.3 Single-Sideband CPM energy-bandwidth comparison

In this section, through figures 3.9 and 3.10, we show comparison plots between SSB-FSK and other CPM schemes. We used SSB-FSK parameters based on the results obtained from the optimization study given in Section 3.2. The plots are characterized by the SSB normalized bandwidth occupancy in the x-axis (BW) and $10\log_{10}(d^2_{\min}/2)$ for the y-axis (energy). Moreover, we divided this section into two parts; one illustrates the occupied BW as 99% of the power inside BT_b. The other illustrates 99.9% of the power in the BT_b (Note that the 99.9% is a more significant measure compared to the 99%; therefore, 99.9%

curves and configurations are located on the right side compared to 99%). The curves and configurations with better performance are located toward the upper left side. For each BW part, we will always start with a general comparison between the optimum curves obtained for SSB-FSK and those obtained for CPM schemes, where the optimum curves do not consider the complexity (N_s). Then, we move on to a more detailed comparison, where we also consider the configurations with optimized complexity and evaluate how much they are biased from the optimum curves. The optimum curves for SSB-FSK are the same *Pareto optimum* curves obtained from Section 3.2.3, and they are presented with the same notation $P_{\mathrm{opt-max}}$, followed by the modulation level M (e.g., $P_{\mathrm{opt-max-4}}$, for $M = 4$). For each of the optimum curves, the optimum normalized minimum squared Euclidean distance $d^2_{\mathrm{min-opt}}$ and the optimum normalized bandwidth BW occupancy BW_{opt} are also presented in the plots, denoted by Config. A and Config. B for B_{99}, respectively. Likewise, they will be denoted by Config. A$'$ and Config. B$'$ for B_{999}. A subscription is used to refer to the modulation level, e.g., Config. A_2 refers to Config. A for the binary case.

A next step in the following discussion is to include the complexity as a third performance metric along side the energy efficiency and the bandwidth occupancy in order to be able to select efficient SSB-FSK schemes with reasonable receiver complexity. Therefore, we chose to superimpose the configurations obtained from Section 3.2.4 (by taking into account the metric N_s), presented as triangular markers with an index number, to Pareto optimum curves. Similar to Section 3.2.4, the index number presents the row in Table 3.4 and Table 3.5, for 99% and 99.9% normalized BW occupancy, respectively. For a fair comparison with other CPM schemes, we present the RC curves for different modulation levels M and pulse lengths L. The legends of the RC-based schemes are given starting with the pulse type followed by the modulation level M and the pulse length L (e.g., RC-2-3 is the raised cosine pulse for modulation level $M = 2$ and pulse length $L = 3$). For the RC curve, we also present the configurations with $N_\mathrm{s} < 64$ (similar to Section 3.2.4, configurations with $N_\mathrm{s} > 64$ are considered as highly complex systems).

Each configuration related to the RC pulse is shown as star marker with an index number. Similar to SSB-FSK, the index number presents the row in Table 3.4 and Table 3.5, respectively, for 99% and 99.9% normalized BW occupancy. Finally, the configuration of GMSK with $BT = 0.3$ is also shown as an “X" marker in Fig. 3.9 and Fig. 3.10. The GMSK has a complexity $N_\mathrm{s} = 16$.
Note, all configurations located outside the region of the energy-bandwidth comparison are not considered (y-axis < -2 dB for 99% and 99.9%, the x-axis > 1 and > 1.25 for

99% and 99.9%, respectively). Therefore, we can observe that there are no configuration for some of the RC curve.

3.3.3.1 99% Bandwidth occupancy

Fig. 3.9 illustrates the performance for B_{99} of SSB-FSK signals compared to LRC for different modulation levels M. Starting with the SSB-FSK curves, the $P_{\text{opt}-\text{max}}$ for all modulation levels M outperforms the GMSK, where we obtain an energy consumption gain of 1.35, 3.03, and 2.67 dB for Config. A_2, Config. A_4, and Config. A_8 for approximately the same normalized bandwidth BW occupancy, respectively. Similarly, we obtain a normalized bandwidth BW occupancy gain of 0.125, 0.26, and 0.233 for Config. B_2, Config. B_4, and Config. B_8 for almost the same energy consumption, respectively. Compared to the binary RC, the $P_{\text{opt}-\text{max}-2}$ outperforms the binary 3RC; however, we obtain the same performance compared to binary 6RC. On the other hand, the $P_{\text{opt}-\text{max}-4}$ and $P_{\text{opt}-\text{max}-8}$ outrun the binary RC for all cases. Likewise, for $M = 4$, using the $P_{\text{opt}-\text{max}-4}$, we obtain almost the same performance as quaternary 3RC. Similarly, for $M = 8$, we obtain a slightly better performance using $P_{\text{opt}-\text{max}-8}$ compared to 8-ary 3RC. However, for all normalized bandwidth occupancies, the $P_{\text{opt}-\text{max}-4}$ outperforms the $P_{\text{opt}-\text{max}-8}$, meaning that increasing the modulation level M will not always increase the performance. Besides, we can highlight the effect of increasing the modulation level M, especially between $M = 2$ and $M = 4$; we obtain an energy consumption gain of 1.68 dB between Config. A_2 and Config. A_4 for the same normalized bandwidth occupancy. Similarly, considering now the normalized bandwidth occupancy, we obtain a gain of 0.135 between Config. B_2 and Config. B_4 for almost the same energy consumption.

When the complexity is taken into account inside our configurations selection process, a more intelligible reading of Fig. 3.9 is given through Table 3.4. It is clear that configurations “4" (2SSB-FSK) and “7" (3RC) have the highest energy performance, where configuration “4" (2SSB-FSK) is slightly better in terms of energy performance. From a bandwidth occupancy point of view, apart from configuration “2" (2SSB-FSK), which is clearly distinguished by the lowest normalized BW occupancy, all other configurations perform pretty similarly. From a complexity point of view, configurations “1" (1SSB-FSK) and “4" (2SSB-FSK) stand out by offering the optimal detection with the lowest number of states. Configuration “1" (1SSB-FSK) has lower complexity ($N_\text{s} = 4$) compared to configuration “4" (1SSB-FSK) ($N_\text{s} = 8$) at the price of a vast decrease in the energy efficiency. Finally, if we consider all performance metrics together, it is evident from Table 3.4, that

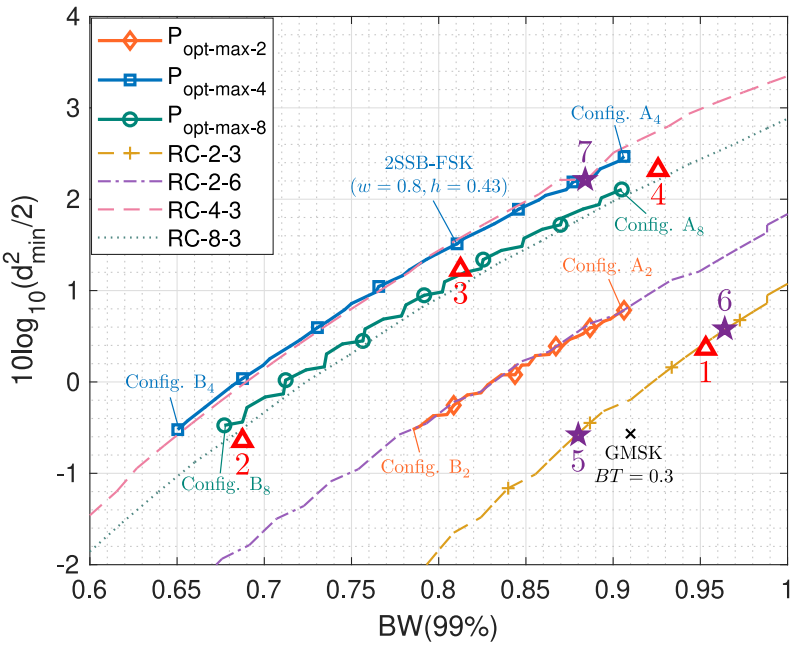

Figure 3.9 – Energy-Bandwidth plot for LSSB-FSK and LRC for different modulation level $M = 2, 4, 8$ using B_{99}. GMSK is presented as an“x" mark.

configuration “4" (1SSB-FSK) presents the best tradeoff.
Overall, these comparisons reveal that if we consider each metric alone (energy, normalized BW occupancy, receiver complexity) or consider all metrics together, we will always obtain the best configuration from the SSB-FSK scheme.

3.3.3.2 99.9% Bandwidth occupancy

As in the previous part, in Fig. 3.10, we compare SSB-FSK $P_{\text{opt}-\max}$ curves to GMSK (shown as x mark in the plot). We achieve a gain of 2.8 dB, 2.3 dB, and 2.4 dB for Config. A'_2, Config. A'_4, and Config. A'_8, respectively, at nearly the same normalized bandwidth BW occupancy. Likewise, we obtain a gain of 0.19, 0.227, and 0.226, for Config. B'_2, Config. B'_4, and Config. B'_8, respectively, at almost the same energy consumption. Config. C′ is reported for the sake of comparison, and it is clearly an interesting operating point as discussed in the optimization study given in Section 3.2. Besides, the $P_{\text{opt}-\max}$ for different modulation levels M outperforms the binary RC for pulse length $L = 3$ and 6. However, the pulse length L used in $P_{\text{opt}-\max-2}$ is always larger than or equal to 6, especially for Config. A'_2 where we have a pulse length $L = 12$. With $L = 12$, we have a disastrous impact on the receiver complexity. The solution to treat the complexity problem is to

Index	Modulation Type	d^2_{min}	BW	States (N_s)
1	1SSB-FSK ($M = 8, h = 0.25, w = 0.7$)	2.175	0.953	4
2	2SSB-FSK ($M = 8, h = 0.25, w = 0.5$)	1.724	0.687	32
3	2SSB-FSK ($M = 4, h = 0.4, w = 0.5$)	2.654	0.8125	20
4	2SSB-FSK ($M = 4, h = 0.5, w = 1$)	3.412	0.925	8
5	3RC ($M = 2, h = 0.5$)	1.75	0.88	16
6	3RC ($M = 2, h = 0.6$)	2.286	0.964	40
7	3RC ($M = 2, h = 0.5$)	3.33	0.884	64

Worst Best

Table 3.4 – Performance of LSSB-FSK and LRC configurations with the lowest complexity for 99% normalized BW occupancy.

use some other configurations with lower complexity N_s at the cost of some performance drop. For modulation level $M = 4$, we note a different behavior compared to the last part. In the B_{99}, we obtained the same performance using $P_{\mathrm{opt-max-4}}$ and quaternary 3RC. However, for B_{999}, the quaternary 3RC outruns the $P_{\mathrm{opt-max-4}}$ and $P_{\mathrm{opt-max-8}}$ for all configurations. Unlike what we noticed for the quaternary case, we do not have unique behavior for the binary case. For instance, the $P_{\mathrm{opt-max-2}}$ outperforms the $P_{\mathrm{opt-max-4}}$ for all $BW \geq 1$ and outperforms the $P_{\mathrm{opt-max-8}}$ for all $BW \geq 1.01$. Moreover, it also has a similar or better performance than the quaternary 3RC for points defined on the B_{999} plot for $1 \leq BW \leq 1.05$.

When comparisons have to be made also considering the receiver complexity, we have to rely on the results summarized in Table 3.5. Note that configuration “0" is out of comparison; it does not come from our optimization process, but it is given only to illustrate the study case given in the original proposal in [19, 18] (Chapter 2). We observe that configuration “4" (6SSB-FSK) has the absolute highest energy performance. Nevertheless, “6" (3RC) is also considered an energy efficient scheme as it offers a slightly lower energy performance. From a bandwidth occupancy point of view, apart from configuration “2" (2SSB-FSK), which offers the lowest normalized BW occupancy, the standard deviation of the normalized BW occupancy of the remaining configurations is relatively small. Therefore, our choice will not highly rely on this metric. When considering the receiver complexity, only configuration “1" (2SSB-FSK) stands out by achieving an extremely low

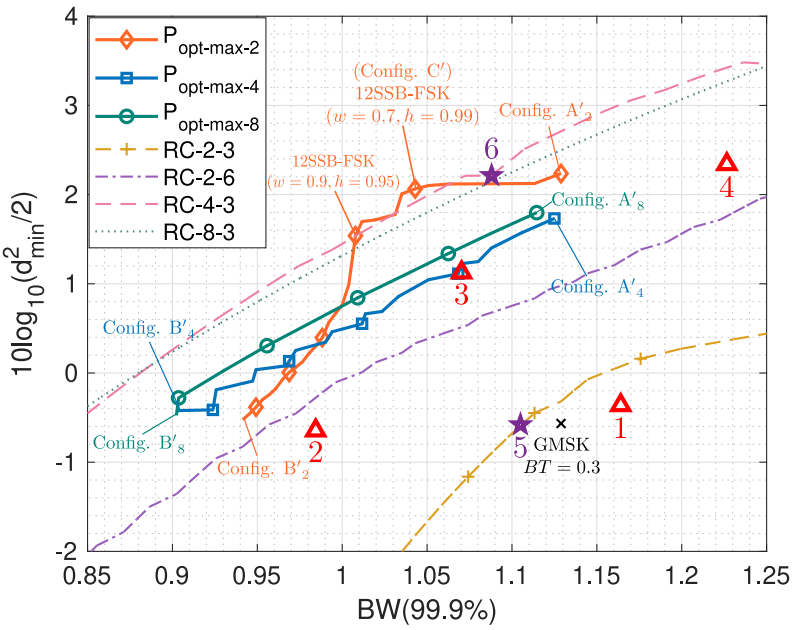

Figure 3.10 – Energy-Bandwidth plot for LSSB-FSK and LRC for different modulation level $M = 2, 4, 8$ using B_{999}. GMSK is presented as an “x" mark.

receiver complexity.

Like the last part, if we consider each metric alone, the best configuration will be a SSB-FSK scheme type. Nevertheless, in terms of combined metrics evaluation, it is hard to consider a unique configuration since “3" (2SSB-FSK), “4" (6SSB-FSK), and even “6" (3RC) show different reasonable tradeoffs between complexity and performance. Finally, compared to configuration “0", which is the study case from the original proposal in [19, 18], it is clear that configuration “4" (6SSB-FSK) outperforms the original proposal. More precisely, “4" (6SSB-FSK) offers a better spectrum occupancy whereas maintaining a better energy consumption performance (≈ 2.56 dB). Moreover, “4" (6SSB-FSK) presents a huge decrease in complexity ($N_s = 32$) in comparison to ($N_s = 2048$). This is achieved at the price of a slight SSB-LOSS of roughly 0.3, compared to the original scheme.

3.3.4 Integer modulation index synchronization advantage

In [1, Ch. 9, Sec. 1] and [61], the authors show an advantage of using integer modulation index h for synchronization. Based on the results obtained from Section 3.3.3.2, configuration “4" (6SSB-FSK) has an integer modulation index $h = 1$, and it is one of the best configurations obtained for B_{999}. Usually, CPM schemes with integer h are avoided

Index	Modulation Type	d^2_{min}	BW	States (N_s)
0	12SSB-FSK (original proposal) ($M = 2, h = 1, w = 0.37$)	1.9	2.06	2048
1	2SSB-FSK ($M = 2, h = 0.5, w = 0.6$)	1.84	1.164	4
2	2SSB-FSK ($M = 8, h = 0.25, w = 0.5$)	1.724	0.984	32
3	2SSB-FSK ($M = 4, h = 0.4, w = 0.6$)	2.6	1.07	20
4	6SSB-FSK ($M = 2, h = 1, w = 1.1$)	3.43	1.226	32
5	3RC ($M = 2, h = 0.5$)	1.75	1.105	16
6	3RC ($M = 4, h = 0.5$)	3.33	1.088	64

Worst Best

Table 3.5 – Performance of LSSB-FSK and LRC configurations with the lowest complexity for 99.9% normalized BW occupancy.

due to their weak performance [1] (Section 1.4.2), which is not the case for configuration "4" (6SSB-FSK). Since we present a comparison between SSB-FSK and RC in Section 3.3, it is interesting to show how the RC scheme behaves when operating with an integer h. In Fig. 3.11, we present the *Pareto optimum* RC plot with modulation index $h = 1$ for all pulse lengths $1 \leq L \leq 12$ and modulation levels $M = \{2, 4, 8\}$. Integer modulation indices $h > 1$ are not considered since they show a poor normalized BW occupancy. From Fig. 3.11 we can observe that configuration "4" (6SSB-FSK) presents a gain of 0.9 dB and slightly lower normalized BW occupancy 0.04 compared to the best configuration presented in the *Pareto optimum* for RC ($L = 5$, $M = 4$, $h = 1$). In terms of complexity, the two configurations have the same number of state $N_\mathrm{s} = 32$. Note that, all configurations shown on the *Pareto optimum* curve (other than the selected configuration of RC) have $N_s > 128$ except the first configuration located at the lower-left corner has a $N_s = 2$ (at the expense of poor performance).

3.4 Concluding remarks and design directives

We have selected the best parameter combinations from the optimization methods to obtain the optimal performance of the SSB-FSK scheme. Based on the parameters chosen from the optimization solution, we achieved a better spectrum occupancy, a gain in error probability performance, and a massive decrease in complexity compared to the

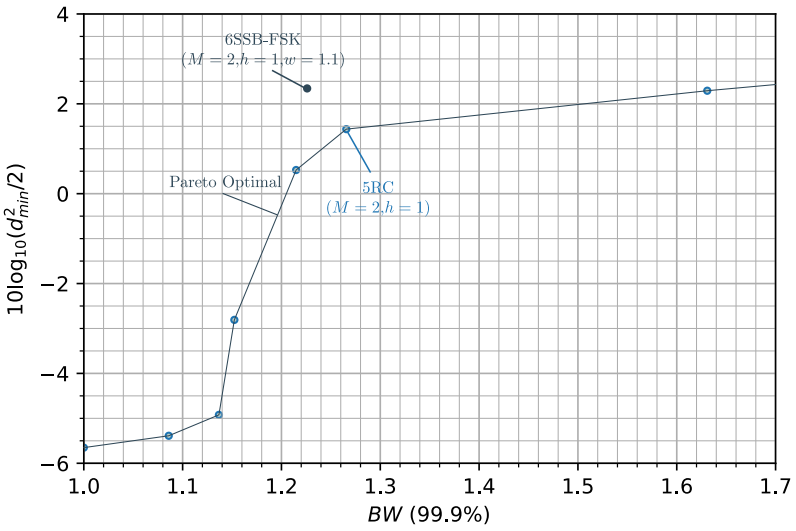

Figure 3.11 – *Pareto optimum* plot of RC with modulation index $h = 1$ in comparison to configuration “4" for B_{999}.

original SSB-FSK proposal [19, 18] (Chapter 2). Our optimization method leads to practical tradeoffs through certain parameter combinations. These tradeoffs differ because they prioritize performance metrics differently. The choice depends on the target application and, consequently, the resources we want to allocate. Finally, we have applied an energy-bandwidth comparison, where we achieved a similar or better performance compared to certain robust CPM modulations. In general, the SSB-FSK has the advantage of being more flexible than RC. For instance, it has been proven that this new waveform is highly tunable, able to provide the most suitable configuration responding to the designer requirements (energy, bandwidth, or complexity). In the B_{99} case, we showed that the configurations obtained from SSB-FSK modulation outperform the RC and GMSK in energy-bandwidth and receiver complexity in any position in the defined comparison region. It is always possible to find a SSB-FSK configuration that outperforms the RC. For B_{999}, the answer cannot be binary or clear-cut, but a less clear-cut analysis has been made, offering several possible tradeoffs.

Nevertheless, the B_{999} analysis allows us to define one SSB-FSK configuration combining excellent performance and advantage in synchronization since it operated with an integer modulation index. This, in particular, offers to SSB-FSK scheme the potential to go beyond what has been achieved with well known CPM schemes (e.g., RC and GMSK). Moreover, we showed that using an integer h with RC will never exceed the SSB-FSK results. Overall, it is clear that the SSB-FSK is not always the best scheme, and it heavily

depends on the parameters. Therefore, selecting the best CPM schemes heavily relies on the target application.

3.5 Conclusion

In this chapter, we optimized the SSB-FSK parameters to provide very efficient transmissions. To exploit all its potential, we investigated the error probability based on the derivation of the minimum Euclidean distance as a function of the modulation index, pulse width, and pulse length. We explored the spectrum of SSB-FSK by quantifying its signal power bandwidth occupancy using a numerical method. We addressed the receiver complexity aspects. These metrics have been used in two different optimization methods to illustrate the full potential of this waveform alongside well-known CPM schemes. In the next chapter, we will focus on the sub-optimum Viterbi-based demodulation scheme using pulse amplitude modulation (PAM) decomposition to offer more sizable complexity reduction. The aim will be to explore other possible configurations offering further possible gains to go beyond what has been achieved with well-known CPM schemes.

Chapter 4

Simplified Receivers For Binary SSB-FSK Using PAM Decomposition

Contents

4.1 Introduction

In the previous chapter, we presented a complete study of the SSB-FSK performance regarding error probability, spectral efficiency, SSB property, and complexity. We investigated the error probability based on the derivation of the minimum Euclidean distance. We explored the spectrum of the SSB-FSK by quantifying its signal power bandwidth occupancy using a numerical method. We estimated the complexity from the number of states required by the Viterbi algorithm (VA) to implement the MLSD optimal receiver. Finally, we used these metrics in two different optimization methods to illustrate the full potential of this waveform. Based on this work, we learned that the SSB-FSK has the advantage of being highly tunable and can go beyond what has been achieved with well-known CPM schemes (e.g., RC and GMSK). This work allowed us to determine some interesting configurations, some with acceptable receiver complexity and others requiring more work to design sub-optimal receivers to reduce their high complexity. Therefore, this chapter aims to reduce the receiver complexity of the SSB-FSK signals using a suboptimal receiver without affecting the performance. The SSB-FSK signals studied in this work is retrieved from the previous chapter for the specific binary case ($M = 2$).
A variety of methods have been suggested to decrease the receiver complexity [1] [56]. We are particularly interested in using the pulse amplitude modulation (PAM) decomposition of CPM signals. Therefore, in this chapter, a reduced-complexity receiver based on the PAM decomposition is designed and analyzed for binary non-antipodal SSB-FSK.

4.1.1 Related works on CPM PAM decomposition

The first connection between linear modulations and CPM was addressed by Laurent [35]. Laurent showed that any binary non-integer single-h CPM could be presented by a superposition of PAM pulses. He also showed that using a reduced number of PAM pulses or even only keeping the main pulse can often approximate very well the CPM signal. Mengali and Morelli followed [40] by extending the PAM decomposition of CPM to M-ary signaling. Then, Huang *et al.* provided the PAM decomposition for the particular case of CPM schemes with integer modulation index [30]. Soon after, Perrins and Rice [49], and Wylie-Green [60] proposed a generalization of this decomposition to include multi-h CPM schemes. Moreover, Perrins and Rice also developed a PAM decomposition for ternary CPM [50], which was revisited and simplified by Othman *et al.* [47].
Following Laurent's PAM decomposition, Kaleh [32] derived a suboptimal MLSD receiver

in AWGN channel using the PAM decomposition. He also showed that with a considerable decrease in the number of matched filters, the suboptimal PAM-based could reach the optimal MLSD receiver. Moreover, Kaleh provided a boundary for the performance of the suboptimal PAM-based receiver. However, Perrins and Rice [52] showed a lack of accuracy in Kaleh bound. Therefore, they derived an exact performance bound for the suboptimal PAM-based receiver in AWGN based on the pairwise error probability. This performance bound has been used to design reduced complexity PAM-based receivers for some CPM schemes [51].

The rest of the chapter is organized as follows: we presented the equivalent PAM representation of SSB-FSK signals for integer and non-integer modulation indices in Section 4.2. In Section 4.4, we developed a simple algorithm to decide on the number of PAM pulses required to attain a specific performance bound. The algorithm is generic; it can provide the results for any parameter combinations. In Section 4.5, we applied the PAM decomposition alongside the algorithm developed on the binary SSB-FSK results retrieved from the previous chapter. In Section 4.6, we showed that the simplified PAM-based receiver could reach a similar bit error rate (BER) performance compared to the optimal receiver with a considerable decrease in complexity. Finally, conclusions are drawn in Section 5.7.

4.2 PAM representation of SSB-FSK signal

In this section, we proposed to apply the same approach given in [35, 30] for the PAM decomposition of CPM signals with integer/non-integer modulation indices. To do so, we had to rewrite the SSB-FSK signal in a way that we could retrieve the same initial assumptions considered in the derivations presented in [35] and [30]. Hence, the signal $s(t,\alpha)$ given in (1.1) and (2.11) is strictly equivalent to

$$\begin{aligned} s(t,\alpha) &= e^{j2\pi\tilde{h}\sum_{i=-\infty}^{+\infty}\alpha_i\phi_0(t-iT_\mathrm{s})} \\ &= \underbrace{e^{j2\pi h\sum_i \tilde{\alpha}_\mathrm{i}\phi_0(t-iT_\mathrm{s})}}_{s_1(t,\tilde{\alpha})}\underbrace{e^{j2\pi h\sum_i \phi_0(t-iT_\mathrm{s})}}_{s_2(t)} \end{aligned} \tag{4.1}$$

where $\tilde{\alpha}_i = 2\alpha_\mathrm{i} - 1 \in \{-1, 1\}$.

According to (4.1), the baseband SSB-FSK signal $s(t,\alpha)$ could be viewed as a product of two independent signals: $s_1(t,\tilde{\alpha})$, depending on the antipodal coded information symbols $\tilde{\alpha}$, and $s_2(t)$ a *deterministic* signal that does not carry any information.

4.2.1 PAM decomposition of SSB-FSK with non-integer modulation index

For non-integer modulation indices, we followed the derivations given by Laurent in [35], where $s_1(t, \tilde{\alpha})$ can be reformulated as

$$s_1(t, \tilde{\alpha}) = \sum_{k=0}^{Q-1} \sum_{n} b_{k,n} c_k(t - nT_\mathrm{s}) \tag{4.2}$$

where $Q = 2^{L-1}$ is the number of pulses required for an exact representation of the signal. The PAM pulse $c_k(t)$ is defined as:

$$c_k(t) = \prod_{i=0}^{L-1} u(t + iT_\mathrm{s} + \beta_{k,i} LT_\mathrm{s}), \quad 0 \leq t \leq D_k T_\mathrm{s}. \tag{4.3}$$

The function $u(t)$ is given by

$$u(t) = \begin{cases} \sin(2\pi h \phi_0(t)), & 0 \leq t \leq LT_\mathrm{s} \\ u(2LT_s - t), & LT_\mathrm{s} < t \leq 2LT_\mathrm{s} \\ 0, & \text{otherwise.} \end{cases} \tag{4.4}$$

Note that the parameters $\beta_{k,i}$ can only take the values 0 or 1, and are obtained from the equality

$$k = \sum_{i=1}^{L-1} 2^{i-1} \beta_{k,i}, \quad 0 \leq k \leq Q - 1. \tag{4.5}$$

Additionally, D_k is the k-th pulse duration, defined as

$$D_k = \min_i \{L(2 - \beta_{k,i}) - i\}, \quad 0 \leq i \leq L - 1. \tag{4.6}$$

Finally, the mapping between the *pseudo-symbols* and the information data α_i follows the expression

$$b_{k,n} = \exp\left\{ jh\pi \left[\sum_{m=-\infty}^{n} \tilde{\alpha}_m - \sum_{i=0}^{L-1} \tilde{\alpha}_{n-i} \beta_{k,i} \right] \right\}. \tag{4.7}$$

4.2.2 PAM decomposition of SSB-FSK with integer modulation index

For integer modulation indices, we follow the derivations given by Huang *et al.* [30], stating that the signal $s_1(t,\tilde{\alpha})$ can be represented as

$$s_1(t,\tilde{\alpha}) = \sum_n J^n \left[h_0(t-nT) + \sum_{k=1}^{2^{L-1}} B_{k,n} h_k(t-nT) \right] \tag{4.8}$$

where $J = \cos(h\pi)$. The PAM pulses $h_0(t)$ and $h_k(t)$ are defined as

$$\begin{aligned} h_0(t) &= \prod_{i=-L+1}^{0} \cos\phi_0(t-iT), \quad 0 \le t \le T \\ h_k(t) &= \prod_{i=1}^{L-1} \cos\phi_0(t-iT) \prod_{i=0}^{L-1} \left[(1-\beta_{k,i}) \cos\phi_0(t+iT) \right. \\ &\quad \left. + \beta_{k,i} \sin\phi_0(t+iT) \right], \quad 0 \le t \le L_k T. \end{aligned} \tag{4.9}$$

The parameters $\beta_{k,i}$ are determined by the equality

$$2k-1 = \sum_{i=0}^{L-1} 2^i \beta_{k,i}, \quad 1 \le k \le 2^{L-1}. \tag{4.10}$$

Additionally, L_k is the k-th pulse duration, defined as

$$L_k = L - \max_{\beta_{k,i} \neq 0} i. \tag{4.11}$$

Finally, the mapping follows the expression

$$B_{k,n} = \prod_{i=0}^{L-1} \left(1 - \beta_{k,i} + \beta_{k,i} j \tilde{\alpha}_{n-i} \right). \tag{4.12}$$

We will always refer to these two PAM decomposition methods with the same notations, v_k, ρ_k, and ℓ_k, for the PAM pulse, the pseudo symbols, and the pulse duration, respectively. In Table 4.1 we present a summary of the notations used.

From what we presented in this section, we could deduce that the PAM decomposition is only applied on the $s_1(t,\tilde{\alpha})$ signal since it contains the complete transmitted information. Thus, the first step on the receiver side is to extract $s_1(t,\tilde{\alpha})$ from $s(t,\alpha)$ by

Table 4.1 – General notations for the PAM decomposition methods.

Definitions	General notations	PAM non-integer modulation index	PAM integer modulation index
PAM pulse	v_k	c_k	h_k
Pseudo symbols	ρ_k	$b_{k,n}$	$B_{k,n}$
Pulse duration	ℓ_k	D_k	L_k

discarding $s_2(t)$, which presents no difficulty since $s_2(t)$ is a deterministic periodic signal with no information. Besides, to make sure that we have no degradation in BER performance after discarding $s_2(t)$, in Appendix. C, we showed that $s_1(t,\tilde{\alpha})$ and $s(t,\alpha)$ have the same error probability performance, using the union bound and the minimum Euclidean distance ($d^2_{\min}$).

4.3 Reduced-Complexity receiver for SSB-FSK

First, we have to recall that the transmitted signal $s(t,\alpha)$ (4.1) is composed of two parts: one information-dependent component $s_1(t,\tilde{\alpha})$, and one information-independent component $s_2(t)$. However, so as to use the PAM decomposition, we need to process only $s_1(t,\tilde{\alpha})$. Therefore, after extracting $s_2(t)$ from the received signal $r(t)$, the input of the proposed detector is expressed as

$$r_1(t) = s_1(t,\tilde{\alpha}) + \tilde{n}(t), \tag{4.13}$$

where $\tilde{n}(t)$ is an equivalent noise resulting from extracting the signal $s_2(t)$, which remains Gaussian (see Appendix E). Using the PAM decomposition presented in Section 4.2, we obtained a Viterbi-like receiver based on the PAM decomposition by inserting $s_1(t,\tilde{\alpha})$ (4.2)/(4.8) (non-integer/integer modulation index h) into (1.19) to get the recursion [32]:

$$\lambda_{n+1}(\hat{E}_n) = \lambda_n(\hat{S}_n) + \underbrace{\mathrm{Re}\left\{\sum_{k=0}^{N} \overline{Z}_{k,n}\rho^*_{k,n}\right\}}_{\lambda(n)}, \tag{4.14}$$

where

$$\overline{Z}_{k,n} = \int_{nT_\mathrm{s}}^{(n+\ell_k)T_\mathrm{s}} r_1(t)v_k(t-nT_\mathrm{s})dt. \tag{4.15}$$

The maximum number of PAM pulses N is given by:

$$N = \begin{cases} Q-1, & \text{(non-integer } h\text{)}, \\ 2^{L-1}, & \text{(integer } h\text{)}. \end{cases} \tag{4.16}$$

The number of states for the PAM-based detector is [51]

$$N_s' = pM^{L'-1}, \tag{4.17}$$

where

$$\begin{cases} L' = L + 1 - \ell_{\min}, \\ \ell_{min} = \min\limits_{k} \ell_k, \quad 0 \leq k \leq N_0. \end{cases} \tag{4.18}$$

From (4.14) and (4.18), we simplified the receiver complexity (number of states and matched filters) by considering a fewer number of pulses [32]. Based on the selection of the number of pulses, the performance and the complexity of the PAM-based receiver may vary. Therefore, it is essential to define thresholds between the number of PAM pulses (complexity) and the performance. In the next section, we will present an algorithm inspired by the methods used in [51] to obtain these thresholds.

4.4 Decision on the number Of PAM pulses

This section discusses how to select the number of PAM pulses for a targeted error probability P_e. In Fig. 4.1, we presented a flowchart for the associated algorithm used to select the number of PAM pulses. The algorithm depends on two important factors: the PAM pulses obtained from the Mean-Square approximation and the performance bounds of the MLSD and the PAM-based receivers.

4.4.1 PAM mean-square approximation

Laurent showed in [35] that the signal power is unevenly distributed between the PAM pulses, and for most cases, almost all the power is concentrated in the first few pulses. We will refer to these pulses as the *main pulses*. Laurent obtained a good approximation of

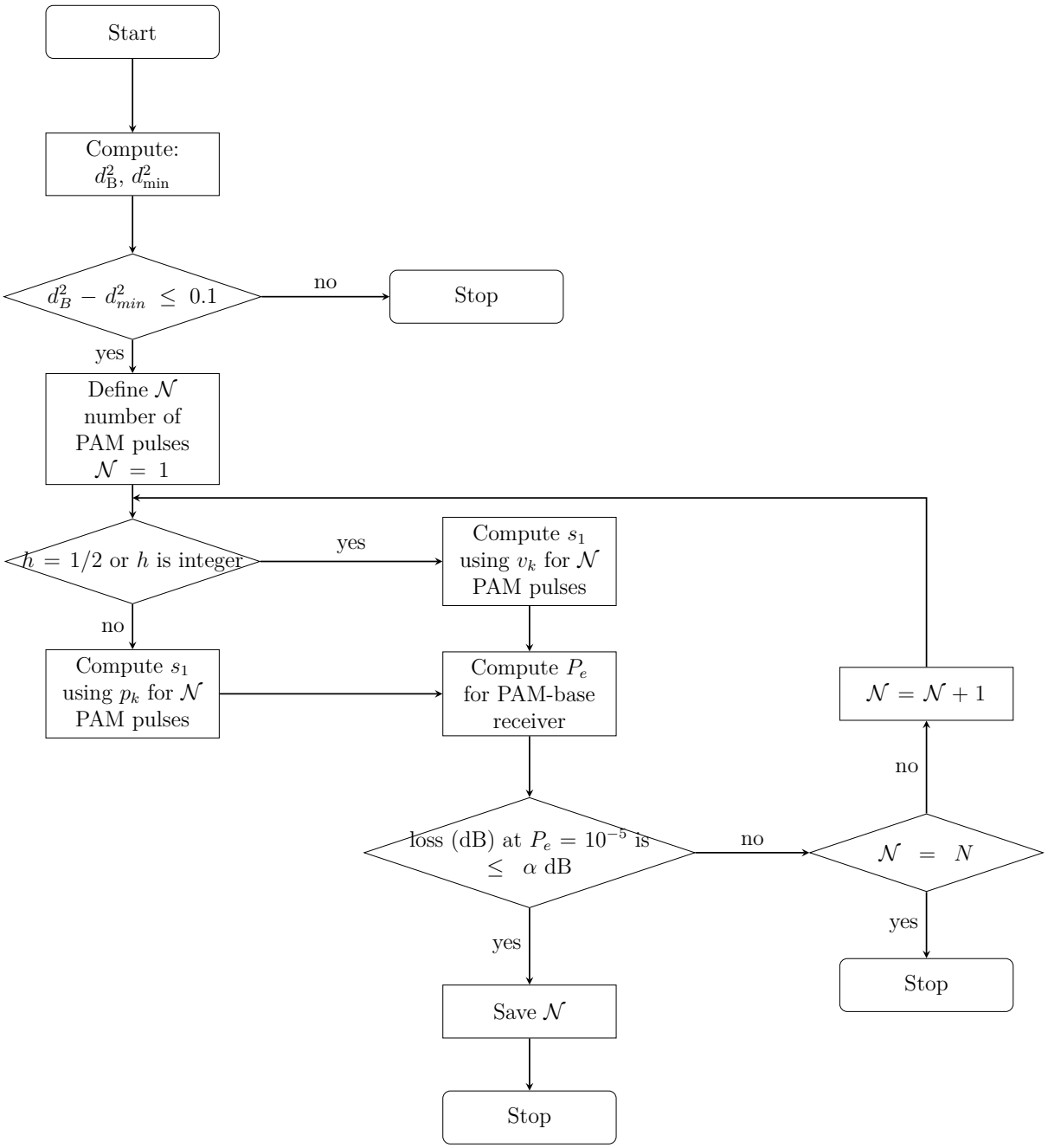

Figure 4.1 – Flowchart of the algorithm used to select the number of PAM pulses required for a specific SNR difference α dB between the optimal MLSD receiver performance bound and the PAM-based receiver performance bound for $P_e = 10^{-5}$.

the original CPM signals using only the main pulses ($\mathcal{N}$) instead of ($N = Q - 1$) pulses. Following Laurent's derivation, Mengali *et al.* [40] showed that a better approximation of the original CPM signals can be obtained using an optimum PAM pulse $p_k(t)$ instead of $v_k(t)$. This optimum pulse $p_k(t)$ is given by minimizing the mean-square error (MSE) with respect to the original signal. The optimum pulse $p_k(t)$ is given by:

$$\begin{aligned} p_k(t) = v_k(t) + \sum_{i=\mathcal{N}}^{N-1} \sum_{m} w_{k,i}(m) v_i(t - mT), \\ 0 \leq k \leq \mathcal{N} - 1, \end{aligned} \tag{4.19}$$

where $w_{k,i}(m)$ are weights whose calculations are detailed in Appendix B.
Furthermore, in [40], it was shown that for a modulation index $h = \frac{1}{2}$, using $p_k(t)$ or $v_k(t)$ has the same performance in approximating the original signal, which means that $v_k(t)$ is already optimal in the MSE sense.
In Table 4.2, we present the MSE between the original signal and the approximated one using $v_k(t)$ ($\hat{\sigma}$) and $p_k(t)$ ($\tilde{\sigma}$), for three CPM schemes with a different number of main pulses ($\mathcal{N}$). We can observe from the last two columns that we have similar results between ($\hat{\sigma}$) and ($\tilde{\sigma}$). Therefore, we deduced that also for integer modulation index $h = 1$, $p_k(t)$ and $v_k(t)$ have similar performance in approximating the original signal.
As a consequence, we can find in Fig. 4.1 a decision box that selects the PAM pulse $p_k(t)$ or $v_k(t)$ based on the modulation index value h.

Table 4.2 – The MSE between the original signal and the approximated one for integer modulation index $h = 1$.

CPM scheme	Number of main pulses $\mathcal{N}$	$\hat{\sigma}$ (dB)	$\tilde{\sigma}$ (dB)
6SSB-FSK ($w = 1.1$)	2	-2.644	-2.643
	4	-11.927	-11.927
3RC	1	-12.083	-12.082
3REC	1	-3	-3

4.4.2 Performance bound of the PAM-based receiver

The performance of the PAM-based receiver can be computed using the pairwise error probability union bound given in [52]. The union bound for binary single h schemes is

presented in the form

$$P_e \approx \frac{W(\gamma_{\min})}{2^R} \sum_{(i,j)\in\gamma_{min}} Q\left(\sqrt{\frac{E_b}{N_0}} d'(i,j)\right), \tag{4.20}$$

where γ_{min} (different from zero) is the difference sequence $(\alpha_i - \alpha_j)$ corresponding to the modified minimum distance (d'), and R is the span of observation symbols. The function $W(\gamma_{\min})$ is the Hamming weight of the difference vector γ_{min}. The modified minimum distance d' is given by [59]:

$$d^{'}(i,j) = \frac{1}{\sqrt{2E_b}} \frac{d_1(\alpha_j,\alpha_i) - d_1(\alpha_i,\alpha_i)}{\sqrt{d_2(\alpha_i,\alpha_j)}} \tag{4.21}$$

where

$$d_1(\alpha_j,\alpha_i) = \int |\tilde{s}(t;\alpha_j) - s(t;\alpha_i)|^2 dt \tag{4.22}$$

$$d_1(\alpha_i,\alpha_i) = \int |\tilde{s}(t;\alpha_i) - s(t;\alpha_i)|^2 dt \tag{4.23}$$

$$d_2(\alpha_i,\alpha_j) = \int |\tilde{s}(t;\alpha_i) - \tilde{s}(t;\alpha_j)|^2 dt \tag{4.24}$$

with $\tilde{s}(t)$ the approximated signal using $\mathcal{N}$ PAM pulses.

Remark:
The modified Euclidean distance (d') is only an upper bound of the normalized minimum Euclidean distance $(d^2_{\min})$ for the PAM-based receiver. Moreover, it is also known from the analysis of the union bound for the optimal receiver that the minimum normalized Euclidean distance $d^2_{\min}$ will never reach the upper bound d^2_{B} for several modulation indices h (weak modulation index h, see Fig. 1.9). These weak modulation indices h have the same effect on the PAM-based receiver. Due to the high computational efforts on obtaining the exact minimum Euclidean distance $(d^2_{\min})$ for PAM-based receiver [1, ch.8], we will always use the upper bound (d') to presents the performance of PAM-based receiver. To ensure that this upper bound (d') is optimal, we first computed the minimum Euclidean distance $(d^2_{\min})$ and the upper bound (d^2_{B}) for the optimal receiver (see Section 1.4.1, for the algorithm used to compute $d^2_{\min}$ and d^2_{B}). We calculated the difference between the two obtained minimum Euclidean distances. If the difference is slight (≤ 0.1), we assumed that the normalized minimum Euclidean distance $(d^2_{\min})$ could reach the upper

Table 4.3 – The minimum Euclidean distance, the 99.9% bandwidth occupancy, and the complexity (number of states and matched filters) of *L*SSB-FSK studied cases for an optimum MLSD receiver.

Waveform characteristics	d^2_{min}	BW (99.9%)	States (N_s)	Matched filters
6SSB-FSK ($w = 1.1, h = 1$)	3.43	1.226	32	64
2SSB-FSK ($w = 0.6, h = 0.5$)	1.84	1.164	4	8

bound (d^2_{B}), which means that the upper bound (d^2_{B}) can present the minimum euclidean distance (d^2_{min}) for the optimal receiver (tight upper bound). Consequently, d' can present the minimum Euclidean distance (d^2_{min}) for the PAM-based receiver. Therefore, we can find in Fig. 4.1 a decision box, which computes the difference between the normalized minimum Euclidean distance (d^2_{min}) and the upper bound (d^2_{B}), to tests if it exists an upper bound d' that reaches the error probability P_e.

4.5 Case studies for SSB-FSK

We present in this section some case studies for several SSB-FSK schemes, which are showed in Table 4.3. The parameters selection for these schemes was conducted in the previous chapter using the *Pareto optimum* multi-objective optimization.

In Fig. 4.2, we showed how the performance bound for the PAM-based receiver approaches the optimal MLSD performance bound using the algorithm (Fig. 4.1) with ($\alpha < 0.5$) for the configuration 6SSB-FSK from Table 4.3. The plot for $\mathcal{N} = 0$ is not presented, wherefrom (4.8) $v_0(t)$ ($h_0(t)$) does not carry any information, which means a flat performance bound. Therefore, $v_0(t)$ is not considered in $\mathcal{N}$ as one of the required pulses for the PAM-based receiver. From Fig. 4.2, we noted that increasing the number of PAM pulses $\mathcal{N}$ sometimes induces a wide leap toward the optimal bound (especially noted between $\mathcal{N} = 3$ and $\mathcal{N} = 4$). Nevertheless, this is not a general trend: after $\mathcal{N} = 4$ increasing $\mathcal{N}$ has a slight increase towards the optimal bound. Then, it is possible to define different thresholds between the required number of PAM pulses (complexity $\mathcal{N}$) and the performance. The performance is computed in terms of SNR required to reach a specific error probability.

Fig. 4.3 presents the different PAM pulses for the case study presented in Fig. 4.2.

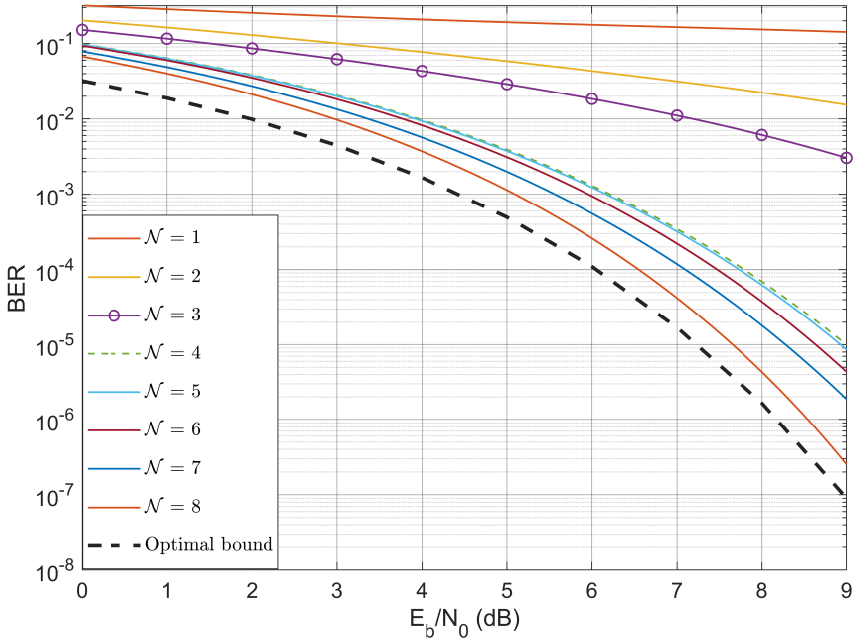

Figure 4.2 – Applying the algorithm (Fig. 4.1) on the first configuration 6SSB-FSK, to obtain the required number of PAM pulses $\mathcal{N}$.

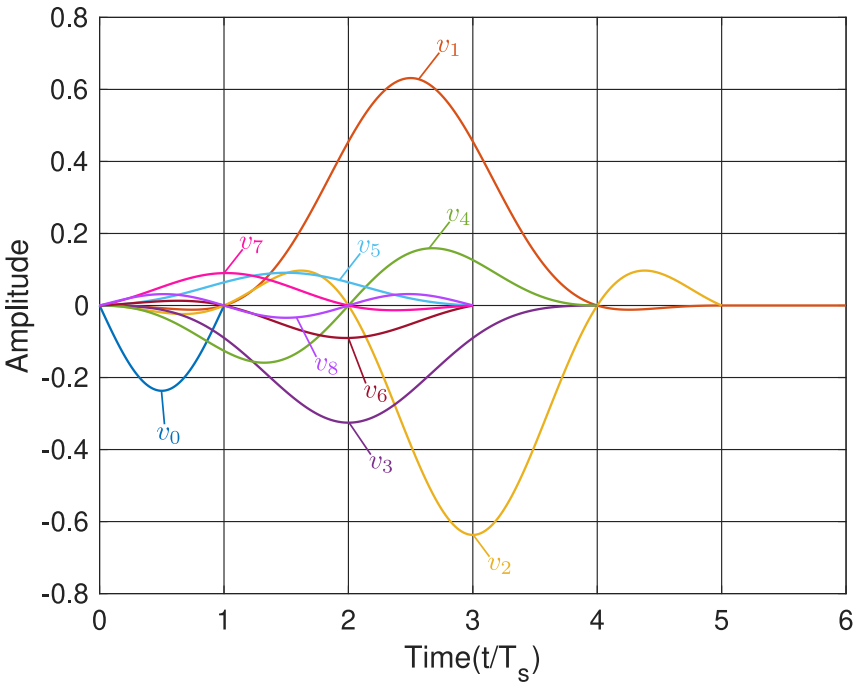

Figure 4.3 – The PAM pulses from (0-8) for the configuration 6SSB-FSK using Huang PAM decomposition.

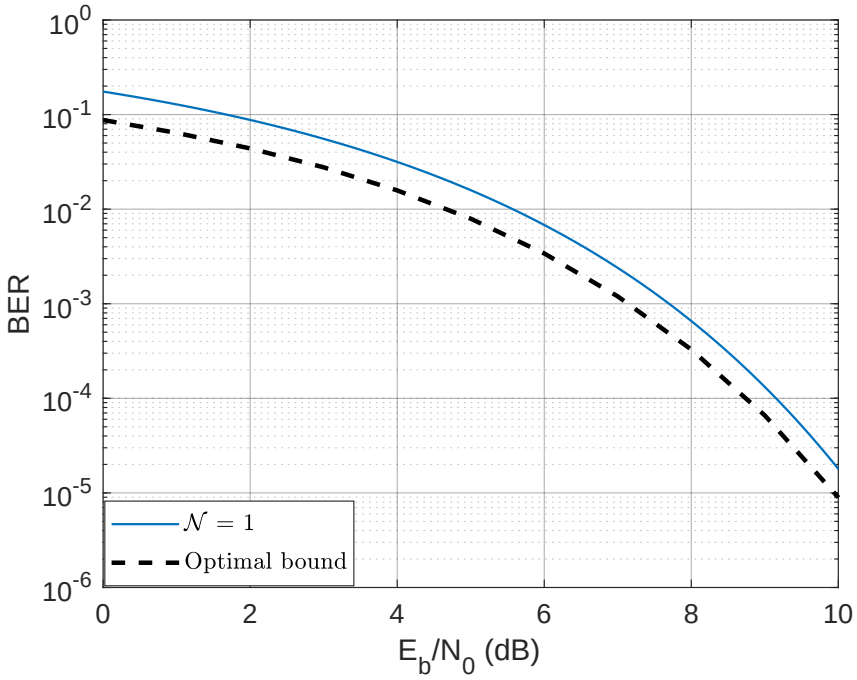

Figure 4.4 – Applying the algorithm (Fig. 4.1) on 2SSB-FSK, the second configuration of Table 4.3, to obtain the required number of PAM pulses $\mathcal{N}$.

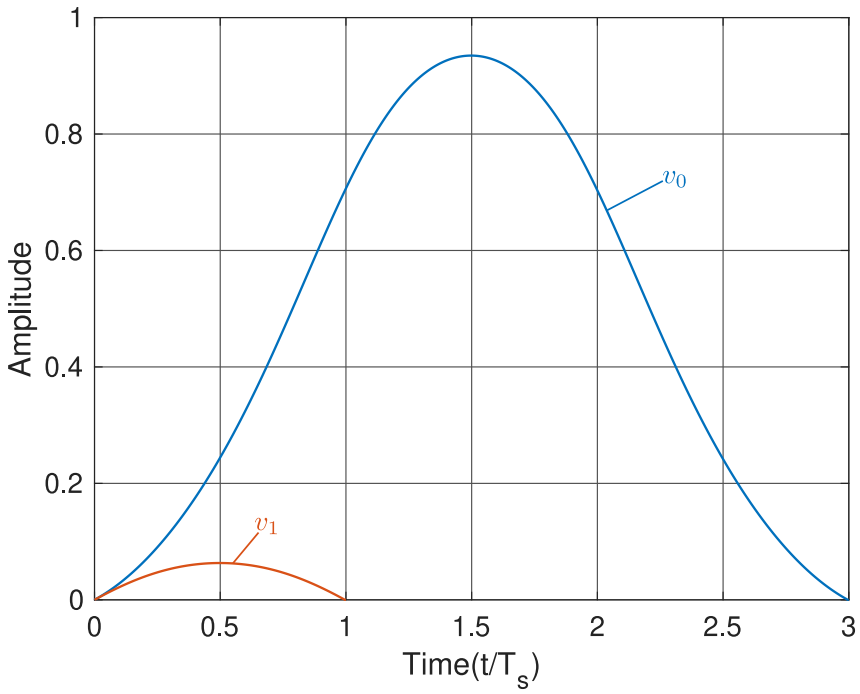

Figure 4.5 – The PAM pulses for the configuration 2SSB-FSK using Laurent PAM decomposition.

Similarly, in Fig. 4.4 we showed the performance bound for the PAM-based receiver approaches the optimal MLSD performance bound using the algorithm (Fig. 4.1) with ($\alpha < 0.5$) for the configuration 2SSB-FSK from Table 4.3. We observe that using only one pulse $\mathcal{N} = 1$ leads to the optimal bound. This observation can be explained from Fig. 4.5, where most of the signal energy is contained in $v_0(t)$.

4.5.1 Linear detector

Based on the observation of Fig. 4.4, we conclude that we only need one pulse to reach the optimal MLSD bound. For this reason, it is interesting to decrease the complexity at the receiver side by applying a linear detector on the received signal instead of the PAM Kaleh receiver. The complex envelope (4.2) of the received signal for 2SSB-FSK can be presented as

$$r_1(t) = \sum_{k=0}^{1} \sum_{n} \rho_{k,n} v_k(t - nT_s) + n(t). \tag{4.25}$$

Since we want to only use the main pulse $v_0(t)$, the sampled matched filter output $\lambda(n)$ (4.14) can be written as

$$\begin{aligned} \lambda(n) &= \mathrm{Re} \int_{-\infty}^{\infty} r_1(t) \sum_{n} \rho_{0,n}^{*} v_0(t - nT) dt = \mathrm{Re} \sum_{n} \rho_{0,n}^{*} \overline{Z}_{0,n} \\ &= \sum_{n} \rho_{0,2n} \,\mathrm{Re}\left\{\overline{Z}_{0,2n}\right\} + \mathrm{Im}\left\{\rho_{0,2n+1}\right\} \mathrm{Im}\left\{\overline{Z}_{0,2n+1}\right\} \end{aligned} \tag{4.26}$$

Based on (4.26), the metrics $\lambda(n)$ used by the symbol-by-symbol detector to estimates $\hat{\rho}_n$ turn into

$$\lambda(n) = \begin{cases} \rho_{0,n} Re\left\{\overline{Z}_0(n)\right\}, & n \text{ even} \\ \mathrm{Im}\left\{\rho_{0,n}\right\} \mathrm{Im}\left\{\overline{Z}_0(n)\right\}, & n \text{ odd} \end{cases} \tag{4.27}$$

where

$$\overline{Z}_0(n) = \int_{-\infty}^{\infty} r_1(t) v_0(t - nT) dt. \tag{4.28}$$

The pseudo-symbols expressions associated with the PAM waveforms are given by (see Appendix D for more details):

$$\begin{cases} \rho_{0,n} = \rho_{0,n-1} j\tilde{\alpha}_n \\ \rho_{1,n} = \rho_{0,n-2} j\tilde{\alpha}_n. \end{cases} \tag{4.29}$$

Now placing $r_1(t)$ from (4.25) into (4.28) to obtain the necessary statistics used to compute

the metrics $\lambda(n)$ (4.27), which are given by

$$\begin{aligned}\mathrm{Re}\left\{\overline{Z}_{0,2n}\right\} = &\left[\sum_m V_{00}(2mT_s)\rho_{0,2n-2m}\right. \\ &\left.+\sum_m V_{10}(2mT_s - T_s)\rho_{1,2n-2m+1}\right] \\ &+\mathrm{Re}\left\{w(2n)\right\}\end{aligned} \tag{4.30}$$

$$\begin{aligned}\mathrm{Im}\left\{\overline{Z}_{0,2n+1}\right\} = &\left[\sum_m V_{00}(2mT_s)\right. \\ &\left.+\sum_m V_{10}(2mT_s - T_s)\,\mathrm{Im}\left\{\rho_{1,2n-2m+2}\right\}\right] \\ &+\mathrm{Im}\left\{w(2n+1)\right\}\end{aligned} \tag{4.31}$$

where

$$V_{0k}(m) = \int v_k(t)v_0(t - mT_s)dt, \quad k \in \{0, 1\} \tag{4.32}$$

and

$$w(n) = \int \tilde{n}(t)v_0(t - nT)dt. \tag{4.33}$$

Expressions (4.30) and (4.31) show that $\overline{Z}_0$ is corrupted by noise and intersymbol interference (ISI) from the pseudo-symbols $\rho_{0,n}$ and $\rho_{1,n}$. To mitigate the interference caused by the pseudo-symbols, Khaleh in [32] proposed the use of a Wiener filter alongside the matched filter $v_0(t)$. The Wiener filter is derived based on the minimum mean square error (MMSE) criterion [53], and its coefficients are computed using the method introduced in [32]. In Fig. 4.6 we presented the coefficients of the Wiener filter C_k^{WF}.
Fig. 4.7 illustrates the PAM pulses $v_0(t)$ and $\tilde{v}_0(t)$, where $\tilde{v}_0(t)$ is a combination of the PAM pulse $v_0(t)$ and the Wiener filter coefficients C_k^{WF}, which is given by

$$\tilde{v}_0(t) = \sum_{k=-\infty}^{+\infty} C_k^{WF} v_0(-t + 2kT). \tag{4.34}$$

4.6 Simulation results

Fig. 4.8 shows a BER comparison between the optimal receiver and Kaleh's receiver for 6SSB-FSK. The 8 states receiver is near optimal, as the BER degradation does not

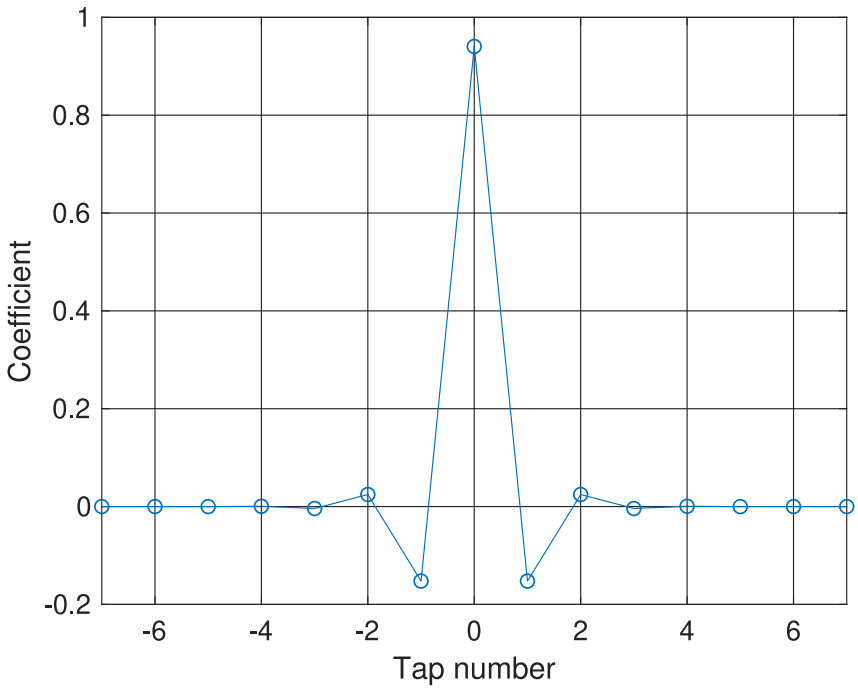

Figure 4.6 – Wiener filter coefficients ($E_b/N_0 = 10$dB) for the configuration 2SSB-FSK.

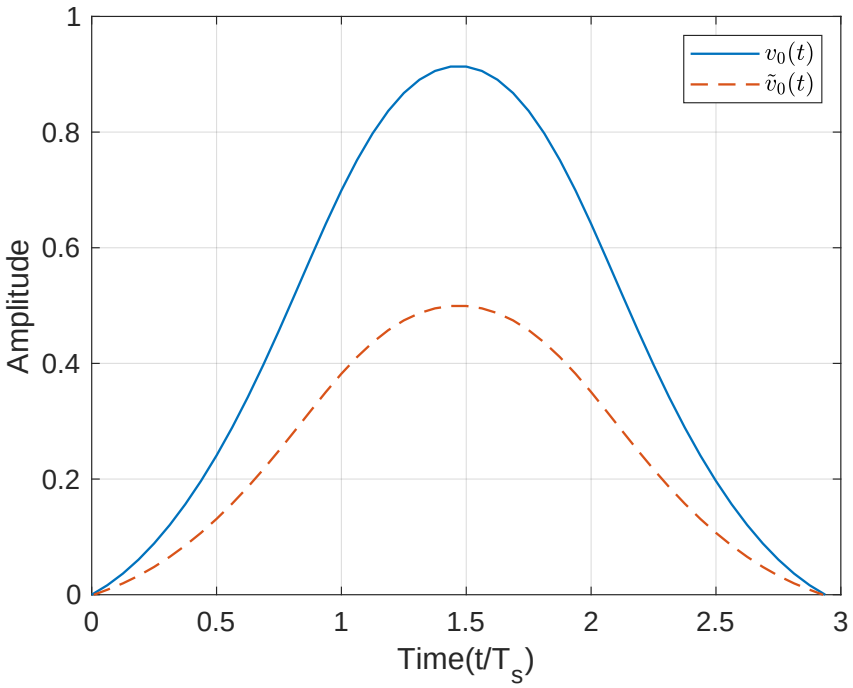

Figure 4.7 – Illustration of $v_0(t)$ and $\tilde{v}_0(t)$ for 2SSB-FSK.

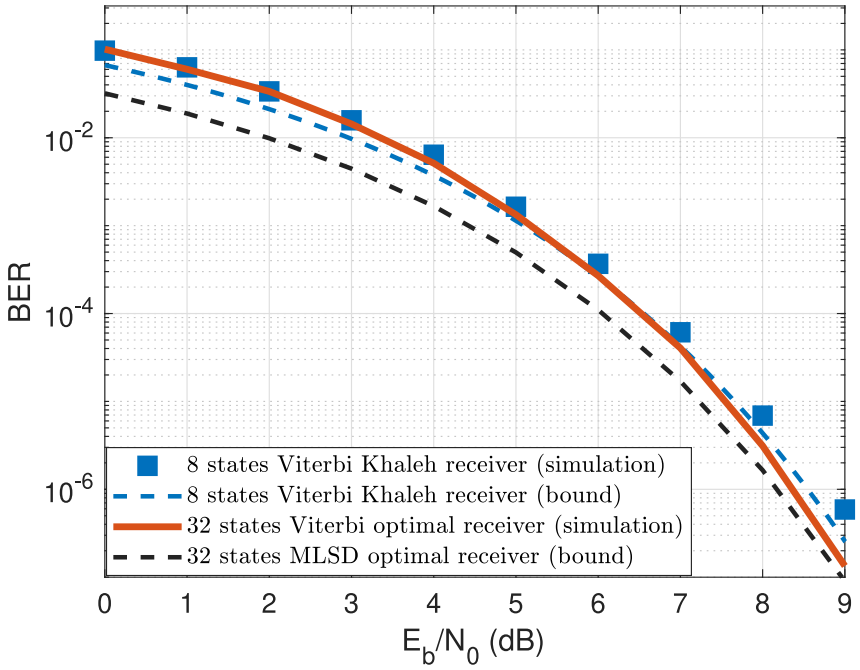

Figure 4.8 – BER performance of configuration 6SSB-FSK in AWGN channel.

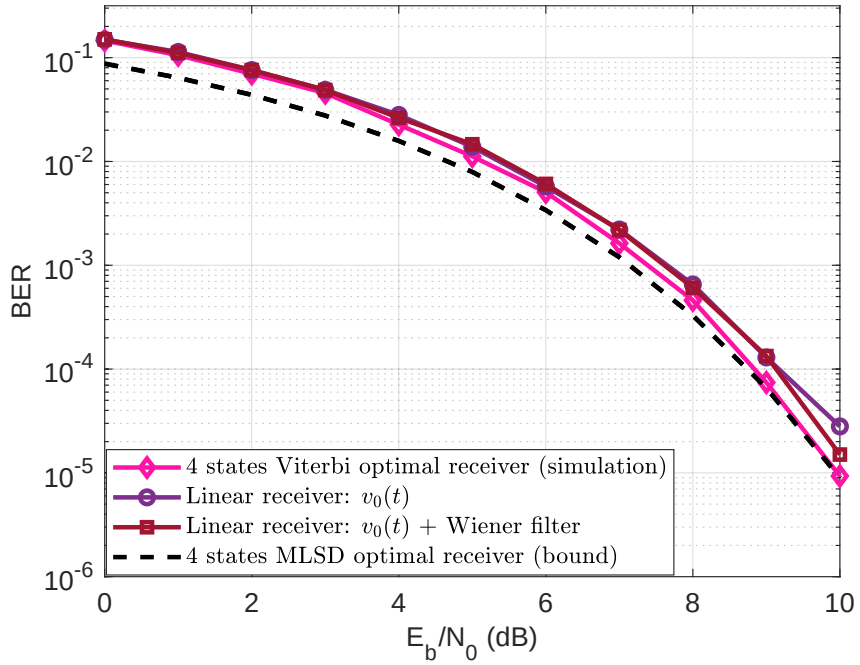

Figure 4.9 – BER performance of configuration 2SSB-FSK in AWGN channel.

exceed 0.1 dB at BER $=10^{-5}$. On the other hand, we obtain a vast decrease in complexity since we went from 32 to 8 for the number of states and 64 to 8 for the number of matched filters. We have also plotted the performance bounds showing a fair reflection of the BER performance, which confirms the results obtained from the algorithm (Fig. 4.1).
Fig. 4.9 presents a BER comparison between the optimal MLSD receiver and the linear receiver for the configuration 2SSB-FSK. The linear filter with Wiener filter reaches a BER $= 10^{-5}$ at a SNR slightly lower than the optimal MLSD bound with a loss equal ≈ 0.2 dB. Without the Wiener filter, the degradation increases to ≈ 0.4 dB.
From these results, we can conclude the importance of the PAM decomposition and the algorithm (Fig. 4.1) in reducing the complexity detection for the SSB-FSK signal.

4.7 Conclusion

In this chapter, we studied a suboptimal receiver for SSB-FSK CPM schemes using PAM decomposition. First, we obtained the linear PAM decomposition of the non-antipodal integer/non-integer modulation index h SSB-FSK. Using the linear PAM decomposition, we proposed a suboptimal receiver. Due to the flexibility of the PAM decomposition, we developed an algorithm with many performance capabilities and with different complexity reductions. One of the most important contribution of this chapter is to reduce the complexity at the receiver side using Khaleh and linear receivers based on the PAM decomposition, with slight but very acceptable decrease in performance.
Following the heavy challenges for designing a powerful simplified SSB-FSK receiver, it is interesting to tackle some other receiver challenges, such as *synchronization*. Therefore, in the next chapter, we target some of the synchronization issues for SSB-FSK signals and how to handle them using the data-aided solution mainly.

Chapter 5

Training Sequence Design For Burst Mode Single Side Band CPM Synchronization

Contents

5.1 Introduction

We focalized on three significant keys in the previous two chapters: error probability, spectral efficiency, and complexity to qualify the SSB-FSK waveform. However, no argument was made about the synchronization, despite being a necessary block in the demodulation process for complete information detection. Therefore, this chapter addresses a synchronization solution for the SSB-FSK, specifically in burst-mode transmission.
In burst-mode transmission, typically, a fixed data sequence is added to each burst to synchronize the receiver quickly and precisely, given that the receiver already knows this data sequence. In literature, we refer to this data sequence as a *preamble* or *training sequence*. It is called a training sequence because the receiver takes advantage of Data Aided (DA) preamble to estimate the synchronization parameters, such as symbol timing, frequency offset, and carrier phase [39]. In this chapter, we are interested in the training sequence design for DA synchronization of burst mode SSB-FSK using the Cramér-Rao bound (CRB) [53]. In DA synchronization, the performance of the estimator may depend on the training sequence used; hence, a good training sequence design is essential. In the recent years, Hosseini and Perrins (Hosseini *et al.*) derived an optimal training sequence for joint estimation of symbol timing, frequency offset, and carrier phase using CRB for different CPM modulations [26, 29, 28]. Since the SSB-FSK is a novel scheme, the original studies by Hosseini *et al.* do not show any comparison between ordinary CPM and the SSB-FSK. Moreover, in a recent analysis on the SSB-FSK [33] (Chapter 3), we showed that the SSB-FSK has the potential to outperform some well-known CPM schemes regarding bit error rate, bandwidth occupations, and complexity. Therefore, it is interesting to study the synchronization performance of the SSB-FSK and compare it to other CPM schemes. By adopting (Hosseini *et al.*) solution and based on the CRB criteria, in this chapter, we make the following steps:

— First, we derive the CRBs for the SSB-FSK scheme based on (Hosseini *et al.*) derivation.
— Second, we showed that for SSB-FSK, it is not possible to obtain a single optimum sequence to minimize simultaneously the CRBs for symbol timing, frequency offset, and carrier phase. Instead, we showed that we need a different optimum sequence for each estimated parameter.
— Third, based on the second step, we choose to minimize the sum of all CRBs, rather than minimizing each CRB parameter simultaneously.

— Finally, we determine a general optimum training sequence that minimizes the sum of all CRBs for any binary SSB-FSK modulation and for different sequence lengths. We refer to this training sequence as the optimum sequence.

The rest of this chapter is structured as follows. In Section 5.2, we derived the CRBs for SSB-FSK signals for a known preamble sequence. In Section 5.3, we derived the optimum preamble sequences via empirical analysis. In Section 5.4, we confirm our previously obtained solution using the *Genetic Algorithm* approach. Section 5.6 presents a CRBs comparison between the optimum sequence suggested by Hosseini *et al.* for GMSK and the SSB-FSK. Moreover, we also showed a performance comparison between the optimum sequence achieved for SSB-FSK and a random sequence. Finally, conclusions are drawn in Section 5.7.

5.2 CRBs and the optimal sequence design for SSB-FSK synchronization

The optimal sequence design is based on minimizing the CRBs for the joint estimation of frequency offset, timing error, and phase error. In [28], the authors derived closed-form expressions for the CRBs when the CPM signal is transmitted over additive white Gaussian noise (AWGN) channel. The complex envelope of the received signal is given by

$$r(t) = \sqrt{\frac{E_s}{T_s}} e^{j(2\pi f_d t + \theta)} e^{j\phi(t-\epsilon;\alpha)} + w(t) \tag{5.1}$$

where f_d is the frequency offset, θ is the unknown carrier phase, ϵ is the time offset, and $w(t)$ is the complex baseband AWGN with zero mean and power spectral density N_0. We set $\mathbf{u} = [f_d, \theta, \epsilon]^T$ as the vector of the unknown but deterministic parameters which are to be jointly estimated at the receiver. Regardless of the estimation method used for the estimation of the parameters, in general it is interesting to obtain a lower bound on the variance estimated error as a performance metric. In this study, we suppose that the estimated parameters $\hat{\mathbf{u}}$ are unbiased. Based on this supposition, we can compute the CRB as a lower bound on the error covariance $C_{\hat{\mathbf{u}}}$ for the joint estimation of $\mathbf{u}$ [28] ,

$$\mathrm{CRB}(\mathbf{u}_i|\alpha) = \left[I(\mathbf{u})^{-1}\right]_{i,i} \leq E\left\{(\hat{u}_i - u_i)^2\right\} = [\mathbf{C}_{\hat{\mathbf{u}}}]_{i,i}\,. \tag{5.2}$$

The CRBs in function of the information sequence α can be obtained through the

Fisher information matrix (FIM) $I(\mathbf{u})$. The elements of the (FIM) are given by [28]

$$I(\mathbf{u})_{i,j} = -\frac{2}{N_0}\int_0^{T_0} Re\left[\frac{\partial r(t,\mathbf{u},\alpha)}{\partial u_i}\frac{\partial r^*(t,\mathbf{u},\alpha)}{\partial u_j}\right]dt, \tag{5.3}$$

where $T_0 = L_0 T_s$ is the duration of the transmitted symbols in seconds and L_0 is the length of the training sequence.
Based on the development given in [28] (see Appendix. F),

$$I(u) = \frac{1}{T_s}\left(\frac{E_s}{N_0}\right)\begin{bmatrix} \frac{8\pi^2 T_0^3}{3} & 2\pi T_0^2 & -8\pi^2\tilde{h}A \\ 2\pi T_0^2 & 2T_0 & -4\pi\tilde{h}B \\ -8\pi^2\tilde{h}A & -4\pi\tilde{h}B & 8\pi^2\tilde{h}^2 C \end{bmatrix} \tag{5.4}$$

where the variables A, B, and C are, where g(t) denotes the frequency pulse

$$A = \sum_{i=0}^{L_0-1}\alpha_i\int_0^{T_0} t g\left(t - iT_s - \epsilon\right)dt \tag{5.5}$$

$$B = \sum_{i=0}^{L_0-1}\alpha_i\int_0^{T_0} g\left(t - iT_s - \epsilon\right)dt \tag{5.6}$$

$$C = \sum_{i=0}^{L_0-1}\sum_{j=0}^{L_0-1}\alpha_i\alpha_j\int_0^{T_0} g\left(t - iT_s - \epsilon\right)g\left(t - jT_s - \epsilon\right)dt. \tag{5.7}$$

Finally, the CRBs equations for frequency offset, carrier phase and symbol time are respectively given by

$$\left[I_{\mathbf{N}}^{-1}\right]_{1,1} = \frac{3T_s}{2\pi^2 L_0^3\frac{E_s}{N_0}} \times \frac{CL_0 - \frac{B^2}{4}}{CL_0 - \frac{B^2}{4} - \frac{3}{4L_0^2}\left(BL_0 - 4A\right)^2} \tag{5.8}$$

$$\left[I_{\mathbf{N}}^{-1}\right]_{2,2} = \frac{2T_s}{L_0\frac{E_s}{N_0}} \times \frac{CL_0^3 - 3A^2}{CL_0^3 - 3A^2 - \left(BL_0 - 3A\right)^2} \tag{5.9}$$

$$\left[I_{\mathbf{N}}^{-1}\right]_{3,3} = \frac{T_s}{\frac{E_s}{N_0}} \times \frac{L_0^3}{8\pi^2\tilde{h}^2\left(CL_0^3 - B^2L_0^2 + 6ABL_0 - 12A^2\right)}. \tag{5.10}$$

According to [28], the training sequence that minimizes the CRB for symbol timing is the solution to

$$\arg\max_{\alpha} C \quad \textbf{subject to} \quad A = B = 0. \tag{5.11}$$

Moreover, the condition $A = B = 0$ also minimizes the CRBs of frequency offset and

phase error estimations. Based on these conditions, the solution of (5.11) for the $M = 2$ antipodal case is [28]

$$\overbrace{-1,\ldots,-1}^{L_0/4},\overbrace{1,\ldots,1}^{L_0/2},\overbrace{-1,\ldots,-1}^{L_0/4}. \tag{5.12}$$

It is clear from (5.5),(5.6), and (5.12) that the number of 1's and -1's are equal to respect the condition in (5.11) ($A = B = 0$). However, an issue arises with the proposed sequence due to the constraints on SSB-FSK symbols, where antipodal coding is not allowed. Hence, optimum sequences are different for each of the synchronization parameters. Therefore, after obtaining the optimal sequence for each parameter, we aim to find a sub-optimum sequence for the estimation of all the parameters together. In this study, we aim to obtain the lowest covariance estimated error for the whole system. Therefore, we choose to minimize the sum of the CRBs as our objective function, supposing that all estimated parameters have the same priority. However, based on the case study, the CRBs can be weighted differently depending on the estimated parameter importance, and other objectives can be established.
To obtain the best training sequence for each parameter, we used a brute force algorithm with $L_0 = 16$ on 12SSB-FSK with $w = 0.37$ and $h = 1$, which are the same parameters used in [19] (Chapter 2). The results obtained are presented in Table 5.1.

Table 5.1 – Training sequences for partial response binary 12SSB-FSK ($w = 0.37$ and $h = 1$), with 16 bits data-added and $\frac{E_s}{N_0} = 1$. The first three rows present the optimum preamble sequences respectively for: symbol time, frequency offset, and phase carrier. The last row presents the sub-optimum preamble for joint estimation of all three parameters.

Partial response SSB-FSK binary case (L =12)			
Training sequence	CRB_ϵ	CRB_{f_d}	CRB_θ
1 1 1 1 1 1 1 0 0 0 0 0 0 0 0 0	0.0043	3.8837e-05	0.1378
0 0 1 0 0 0 0 0 0 0 0 0 0 0 0 0	0.0314	3.7105e-05	0.1298
1 0 1 0 1 1 1 1 0 1 0 1 1 0 0 0	0.0107	6.9213e-05	0.1250
0 0 1 1 1 1 1 1 0 0 0 0 0 0 0 0	0.0056	4.74e-05	0.1252

Table.5.1 shows three different sequences in the first three rows that minimize symbol time, frequency offset and carrier phase CRBs, respectively. However, to save throughput

we can not send three different preamble. Therefore, we need a unique sequence that can minimize all CRBs at the same time. Thus, we apply a new computer search, but this time we search for the sequence that minimizes the sum of CRBs and not each one separately. The sequence is presented in the last row in Table.5.1. We can see that this sequence slightly increases every single CRB. However it increases the overall performance of all CRBS together (it's best to achieve a unique trade-off). This sequence is presented as a sub-optimum preamble for all CRBs.

Since, it is not possible to find an optimum training sequence that minimizes each CRB parameter. In the next parts, we assume that our objective is to find a training sequence that minimizes the sum of all CRBs, and we will refer to it as the optimum sequence and not sub-optimum.

In the next section, we aim to solve two problems that arose in this part:

— For higher L_0, we cannot apply a brute force method to find the optimal training sequence due to the massive increase in the searched space (2^{L_0}).

— There is no general training sequence form, where for each SSB-FSK configuration (L,h, and w), we get a different training sequence that minimizes the sum of the CRBs. For this reason, the solution presented in [27] should be repeated for each training sequence from each SSB-FSK parameters combination. Therefore, to obtain a general solution in the same way shown in [27], we need a general training sequence form relevant to all SSB-FSK configurations.

5.3 Optimum sequence design for SSB-FSK

In this section, we will achieve the solution subsequently in three steps:

1. First, we obtain the optimum training sequence using a brute force method for $L_0 = 20$ and for three different SSB-FSK configurations. The modulation parameters were selected from [33] (Chapter 3), for $M = 2$, and from the original SSB-FSK proposed in [19] (Chapter 2).
2. Based on the trend that would appear from the first step results and those obtained in the previous section, we will propose a general training sequence form.
3. Finally, we take advantage of heuristic search algorithms to confirm that our proposed sequence is the optimal one.

Table 5.2 – Optimum Training sequences for different partial response binary SSB-FSK, with $L_0 = 20$.

SSB-FSK parameters	Training Sequence
12SSB_FSK ($w = 0.37$, $h = 1$)	00001111111000000000
6SSB_FSK ($w = 1.1$, $h = 1$)	00000001111111000000
2SSB_FSK ($w = 0.6$, $h = 0.5$)	00000000111111110000

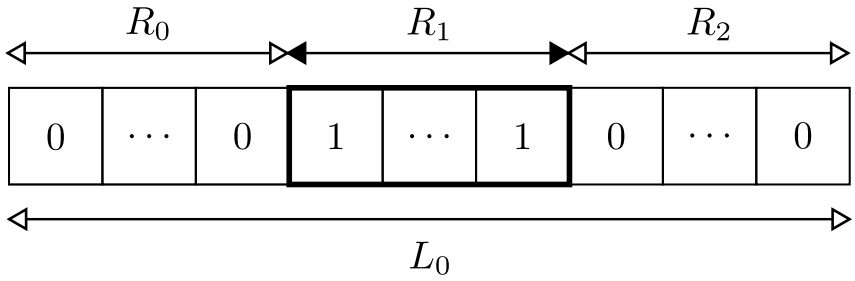

Figure 5.1 – The generalized optimum sequence that minimizes the sum of CRBS for SSB-FSK modulation.

Table. 5.2 presents three different optimum training sequences with length $L_0 = 20$ that minimize the sum of CRBs for three different SSB-FSK configurations. We can observe a specific pattern from the different training sequences, where there are always a set of ones between a set of zeroes. Likewise, in the previous section, for 12SSB-FSK, $w = 0.37$ and $h = 1$ with $L_0 = 16$, we can see a similar behavior (Table 5.1 last row). Based on this observation, we propose in Fig. 5.1, an optimum sequence that minimizes the sum of CRBs for any SSB-FSK modulation and for any training sequence length L_0; R_0 and R_2 exhibit the number of zeros on the left and the right side of the sequence respectively, and R_1 is the number of ones in between. Using the new proposed sequence, we can reduce the searched space using the brute force approach from 2^{L_0} to only $L_0(L_0 + 1)/2$, which leads to a huge reduction in brute force complexity from $\mathcal{O}(2^n)$ to $\mathcal{O}(n^2)$.
With the new proposed sequence, we are now able to provide a solution to the issues mentioned before; however, our results need confirmation since they are only based on empirical analysis. Therefore, in the next section, we will confirm our approach using the well-known search method: the *Genetic Algorithm* (GA) [43].

5.4 Genetic algorithm search

The Genetic Algorithm (GA) is a type of heuristic search algorithm that mimics the natural selection law (evolution) in the search process. This algorithm was created to resolve problems where the solution space is so vast that a brute force approach is not possible (take too long). Moreover, GAs are chromosome-like data structures (binary vector) that indicate potential solutions to a particular problem, such as our optimization problem. Since, as previously stated, a brute force approach is a limitation in our work, and that the parameter optimized (α) for our objective functions (CRBs) is already binary data (do not need encoding), it motivated us to apply the GA in our optimization. The GA has different parameters that interact non-linearly with each others. Therefore, one should find the best parameter combination, which experimentally depends on the problem. In this work, we used the same parameters as in [28], and shown in Table.5.3. Moreover, we simulated each GA scenario 200 times with different initial populations to ensure that the GA does not stick to a local minimum.
Using the GA, we were able to obtain the same optimum training sequence as the one suggested in Fig. 5.1, for $L_0 = \{16, 24, 32\}$, and for the three different SSB-FSK modulations. These results confirm our proposed training sequence scheme and the GA's effectiveness in a large search space (2^{32}). Moreover, we ran the GA for sequence length L_0 from 16 to 128. The ratio between the GA and our proposed sequence is showed in Fig.5.3. We observe that the CRB ratio is always equal or higher to 1, which means that the GA could not find a better sequence than the one found by our supposed training sequence for the three different SSB-FSK configurations. Moreover, the ratio grow with the increase of the sequence length L_0 because the search space becomes huge that the GA converges to a local minimum. Even so, the GA results confirm the accuracy of the supposed optimum sequence.

Note:
Our assumption was based on empirical analysis and GA to confirm that hypothesis, similar to what was done in [28]. However, this does not provide a definite proof that the proposed sequence is the optimum in general for all SSB-FSK schemes.

Table 5.3 – Genetic algorithm parameters.

GA Parameters	
Population size	50
Crossover probability	0.8
Mutation probability	0.02
Maximum number of generations	200

5.5 CRB for random training sequence

Following the determination of the optimal sequence, it's interesting to compare the CRB estimation performance of the optimum sequence with a random training sequence. This necessitates computing the true CRBs while treating the training sequence as an unwanted parameter. For the CPM signal, it is known that the computation of the true CRBs is quite complicated [28]. So far in (5.2), we considered a conditioned estimation based on known training sequence α, which also creates conditioned CRBs. Nevertheless, one can obtain a lower bound on the *unconditional* estimation of any of the parameters by averaging both sides of (5.2) with respect to α [28]

$$E_r\left[(\hat{\epsilon}-\epsilon)^2\right] \geq E_\alpha[\text{CRB}(\epsilon \mid \alpha)] \tag{5.13a}$$

$$E_r\left[(\hat{f}_d-f_d)^2\right] \geq E_\alpha[\text{CRB}(f_d \mid \alpha)] \tag{5.13b}$$

$$E_r\left[(\hat{\theta}-\theta)^2\right] \geq E_\alpha[\text{CRB}(\theta \mid \alpha)]. \tag{5.13c}$$

We refer to the right side of the above equations (5.13a) as the unconditional CRBs for the time offset, frequency offset, and phase offset, respectively. Since, in our study the optimum training sequence is obtained for the sum of the CRBs, we will also take the sum of the unconditional CRBs, which is given by

$$\begin{aligned}\text{UCRB} =& E_\alpha[\text{CRB}(\epsilon \mid \alpha)] + E_\alpha[\text{CRB}(f_d \mid \alpha)] + E_\alpha[\text{CRB}(\theta \mid \alpha)] = \\ & E_\alpha\left\{I_{33}^{-1} + I_{22}^{-1} + I_{11}^{-1}\right\}.\end{aligned} \tag{5.14}$$

Fig. 5.2 provides a performance comparison between the optimum training sequence versus a random sequence illustrated as a ratio between the unconditional CRB (UCRB) and the sum of CRBs using the optimum training sequence for three different SSB-FSK modulations. We obtain the values of the UCRBs numerically via Monte-Carlo simulations. The ratio between the UCRB and the sum of CRBs is showed in dB, which can be

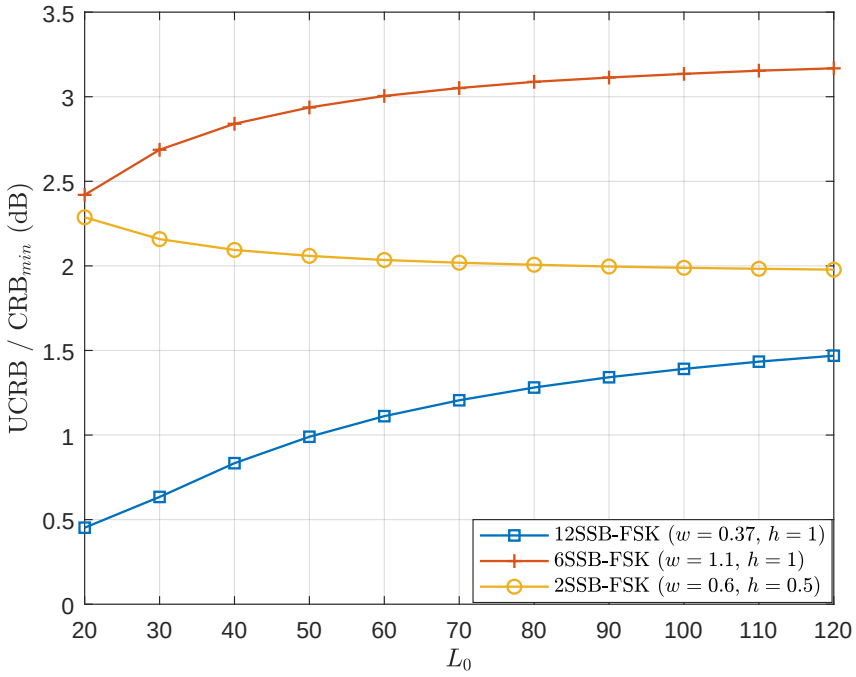

Figure 5.2 – The ratio of the UCRB to the sum of CRBs with the optimum sequence for three different SSB-FSK modulations.

interpreted as a performance gain between the optimum sequence and a random sequence. We can observe from Fig. 5.2 that for 12SSB-FSK and 6SSB-FSK, the performance gain is increasing as L_0 increases and converges to a limit for longer sequence lengths. We can observe a similar behavior with 2SSB-FSK, but this time with a decrease rate in function of L_0. The result for 2SSB-FSK is similar to the results obtained in [28] for other CPM signals. Based on [28] this decline is because a random training sequence becomes less likely to be one of the worst sequences with the increases of the sequence length L_0. From this explanation, we can also conclude that for the other two curves (12SSB-FSK and 6SSB-FSK), the number of poor sequences increases with the increase of L_0 till it converges to a limit where the number of poor sequences is approximately the same. However, a general interpretation is hard to obtain because of the high number of parameters in the SSB-FSK scheme, which may play a significant role in increasing (decreasing) the number of poor sequences with the increase of L_0. Nevertheless, for all three different SSB-FSK modulations, we obtained a performance gain compared to the random sequences. This emphasizes the importance of using a DA estimator that is based on the optimum training sequence.

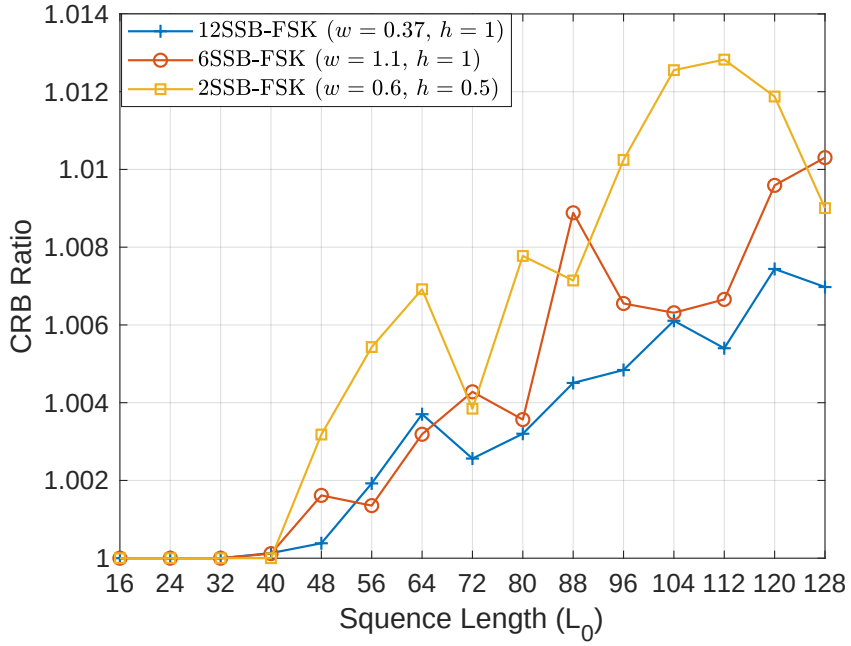

Figure 5.3 – The ratio of the sum of CRBs obtained from GA search to the proposed sequence for different training sequences lengths and SSB-FSK schemes. The proposed sequence has an equal or lower CRBs in all cases.

5.6 Simulation results

The results for the symbol timing, frequency offset, and carrier phase CRBs using our optimum sequence for different SSB-FSK schemes and $L_0 = 32$ are shown in Fig. 5.4, Fig. 5.5, and Fig. 5.6. Moreover, the CRBs for GMSK using the suggested optimum sequence by Hosseini *et al.* are also shown for comparison. For symbol timing in Fig. 5.4, the GMSK shows better performance than the 2SSB-FSK, with a very slight difference. But, the 12SSB-FSK and the 6SSB-FSK offer a better performance than the GMSK with a gap of ≈ 4 dB for the same CRB value.

For the frequency offset, in Fig. 5.5, the GMSK gives a better performance compared with all SSB-FSK configurations. The performance gap between the GMSK and the SSB-FSK can be approximated around 1 dB for the same CRB value. Unlike the CRBs for symbol timing and the frequency offset, the CRBs for the carrier phase in Fig. 5.6 show similar performance for all different SSB-FSK schemes and the GMSK.

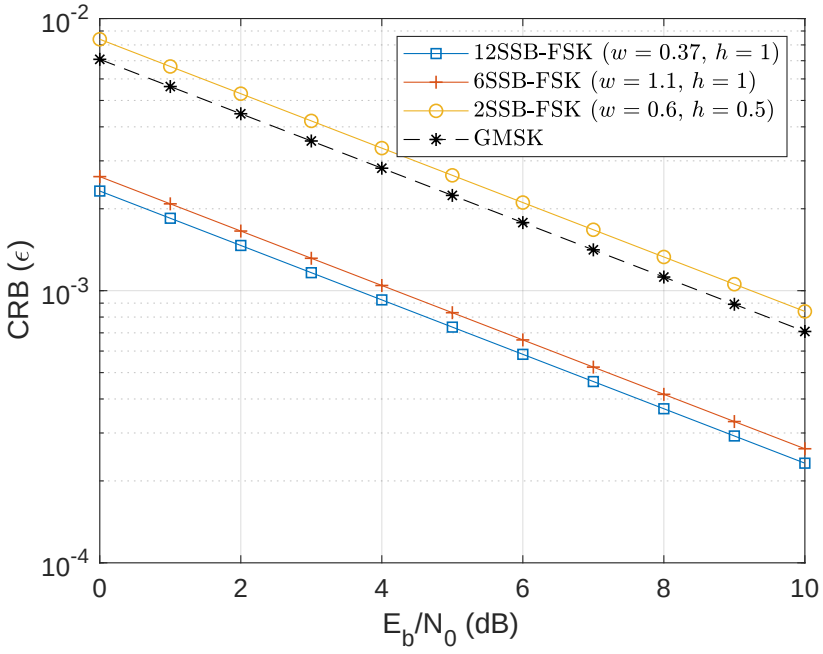

Figure 5.4 – Optimum symbol timing CRBs for three different SSB-FSK modulations with $L_0 = 32$. The optimum sequence suggested by Hosseini *et al.* for GMSK is also shown for comparison.

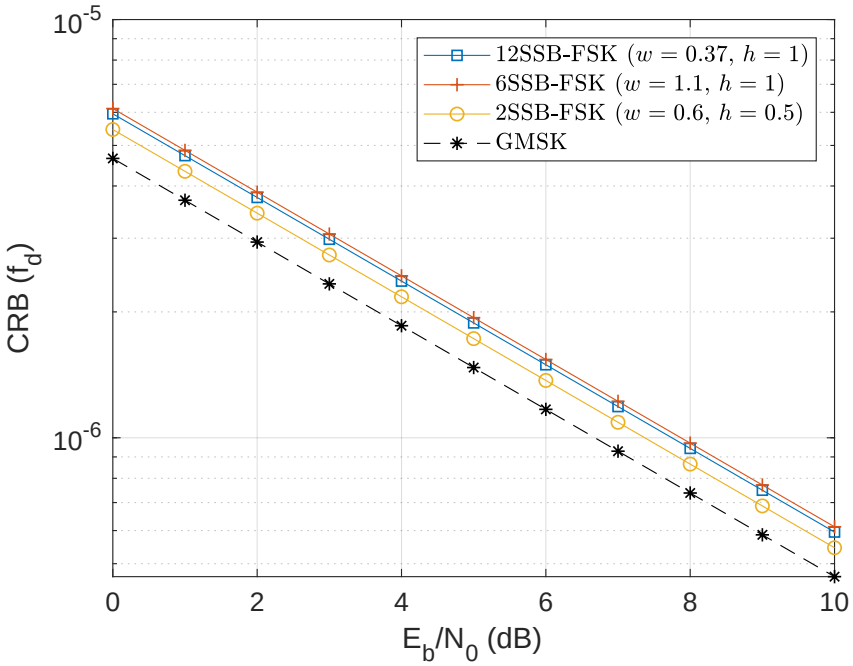

Figure 5.5 – Optimum frequency offset CRBs for three different SSB-FSK modulations with $L_0 = 32$. The optimum sequence suggested by Hosseini *et al.* for GMSK is also shown for comparison.

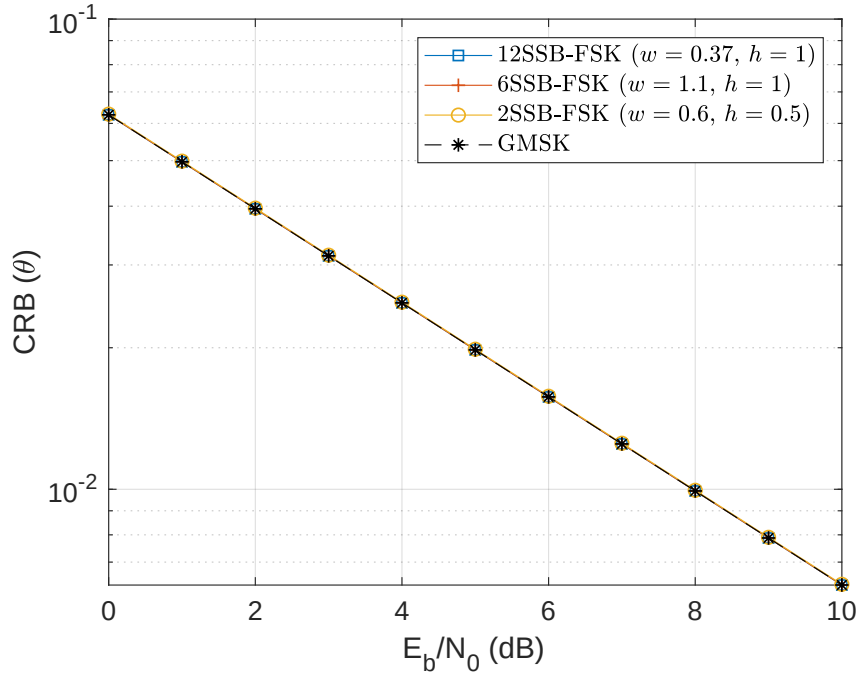

Figure 5.6 – Optimum carrier phase CRBs for three different SSB-FSK modulations with $L_0 = 32$. The optimum sequence suggested by Hosseini *et al.* for GMSK is also shown for comparison.

5.7 Conclusion

We proposed in this chapter a general training sequence that minimizes the sum of CRBs for joint estimation of symbol timing, frequency offset, and carrier phase for SSB-FSK modulation. Our approach to obtain the optimum sequence was first based on using empirical analysis to find a general training sequence pattern. Then, this unique structure found was validated using the GA computer search. We were able to show that the proposed sequence is the same or better than the result obtained from the GA for three different SSB-FSK modulations. Moreover, CRBs comparison between the optimum sequence suggested by Hosseini *et al.* for GMSK and the SSB-FSK was also shown. Furthermore, we compared the performance of the optimum sequence achieved for SSB-FSK with a random sequence using the UCRB. It was shown that using the optimum sequence, we obtain a significant gain for different training sequence lengths.

Conclusions & Perspectives

Conclusions

In this thesis, we have investigated a new CPM scheme called SSB-FSK that can directly generate single side band signals. To exploit all the potential of the signal, the investigation focuses upon four main features: the probability of error (signal energy), the bandwidth occupancy, the receiver complexity, and the synchronization. This investigation aims to characterizes a new CPM scheme which outperforms the conventional CPM schemes.
Based on this study, we were able to suggest new SSB-FSK configurations with different advantages depending on the required application.

In chapter 1, we introduced the CPM signal. We began by presenting the signal model of the CPM signal, and some of the most common applications of CPM modulation. Then we presented all the notions about CPM signals, such as MLSD optimal receiver, minimum Euclidean distance, and bandwidth occupancy. These notions are later used as fundamental basis and tools for the following chapters.

Chapter 2 presented the SSB-FSK signal model, its origin from quantum physics, and an analytical expression for the spectrum for the particular integer modulation index. Furthermore, we gave a spectrum and BER comparison between SSB-FSK and GMSK, and we showed that GMSK could provide better spectral performance than SSB-FSK since SSB-FSK is a tunable waveform and, with standard parameter values, was not yet fully exploited to its potential. Finally, we proposed a an approach to decrease the complexity of the MLSD detector for conventional CPM schemes by rearranging the signal model in the same manner that the SSB-FSK signal is defined. This approach is similar to the solution founded by Rimoldi.

In chapter 3, we fully exploited the SSB-FSK performance. We evaluated the performance using the error probability, the bandwidth occupancy, and the receiver complexity.

Since we considered different performance metrics, we employed the multi-objective optimization "Pareto optimal" to achieve potential SSB-FSK schemes *that outperform* conventional CPM schemes, mainly in the case of integer modulation indexs combining good performance and synchronization advantage.

Chapter 4 investigated suboptimal receivers for SSB-FSK scheme with modulation level $M = 2$. The SSB-FSK schemes considered in this chapter were obtained from the previous chapter (chapter 3) results. The suboptimal receivers were achieved using the linear PAM decomposition alongside Khaleh and linear receivers to minimize the receiver complexity, with a small but acceptable performance loss. The PAM pulses were derived from an algorithm we developed.

Finally, in chapter 5, an optimal generic training sequence that minimizes the sum of Cramér-Rao bounds (CRBs) is designed for the synchronization of symbol timing, frequency offset, and carrier phase for the SSB-FSK scheme. The optimal sequence was confirmed using the genetic algorithm for three different SSB-FSK configurations. In addition, using the unconditional Cramér-Rao bound (UCRB), we evaluated the performance of the optimal sequence with a random sequence. For various training sequence durations, it was shown that using the optimal sequence yielded a substantial decrease in the sum of CRBs bounds.

Perspectives

Despite the present wide variety of available waveforms (single carrier, multi-carrier, ...) used to adapt to many different situations, there is still room to investigate new original waveforms. The current work on the new CPM waveform called SSB-FSK is not yet complete. Further optimization is required to obtain the full potential at reception. Below are few directions which may be worth pursuing.

Spectral Lines (spikes)

1- Synchronization

In chapter 3, we revealed a new SSB-FSK configuration ($h = 1$, $L = 6$, $w = 1.1$ and $M = 2$), with good performance and show sharp spectral lines offering an advantage

for synchronization. The presence of the spectral lines is due to the integer modulation index $h = 1$. Therefore, further investigations on taking advantage of the spectral lines for synchronization is required. In [1, Ch. 9, Sec. 1] and [61], the authors showed some studies which can be helpful to build a full synchronization system using the spectral lines.

2- On–off keying using spectral lines

The simplest type of amplitude-shift keying (ASK) modulation is the on-off keying (OOK), where it encodes digital data as the presence or absence of a carrier wave [2]. A binary one is represented by the presence of a carrier for a specified period. In contrast, a binary zero is represented by the absence of a carrier for the same duration. We can employ the spectral lines of any CPM schemes with integer modulation index h similarly to the OOK but in the frequency domain. A binary one is presented with the appearance of spectral lines, whereas the absence of the spectral lines represents a binary zero. The appearance or disappearance of the spectral lines does not affect the transmitted information, wherein chapter 4, Section 4.2.2 we showed that $h_0(t)$ the PAM pulse responsible for the appearance of the spikes does not contain any information. Therefore, further investigation is required since we cannot identify a literature method that uses spectral lines in such way to send information. The primary purpose of the spectral lines OOK is to send additional information and consequently increase the spectral efficiency. In addition, as we mentioned in the previous point, the SSB-FSK configuration ($h = 1$, $L = 6$, $w = 1.1$ and $M = 2$) has the best performance between all CPM schemes that have spikes in the spectrum (integer modulation index). Therefore, alongside the spikes OOK, the SSB-FSK is much more competitive regarding other CPM schemes.

Symbol Timing, carrier phase, and frequency synchronization of burst-mode SSB-FSK

In chapter 5, we designed an optimal generic training sequence for the synchronization of symbol timing, frequency offset, and carrier phase for the SSB-FSK scheme. In [27], Hosseini *et al.* present a feedforward data-aided (DA) maximum likelihood algorithm for joint estimation of frequency offset, symbol timing, and carrier phase in burst-mode CPM signals for AWGN channel. The proposed approach takes advantage of the optimized preamble of [28], which jointly minimizes the Cramer-Rao bounds CRBs for all three synchronization parameters. Similar to the approach illustrated [27], we can take advantage

of the optimal training sequence designed for the SSB-FSK scheme to jointly estimate symbol timing, frequency offset, and carrier phase.

Appendix A

Appendix for chapter 1: Derivation details of the normalized minimum Euclidean distance

In this appendix, we detail how (1.25) was obtained from (1.24), similarly to the derivation given in [1, ch.2, p.26-p.28] and [53, ch.4, p.251-p.252].
The carrier modulated signal corresponding to the real part of (1.1) is expressed as

$$s(t,\alpha) = \sqrt{\frac{2E}{T_s}}\cos[w_0 t + \phi(t;\alpha)] \tag{A.1}$$

where $E_\mathrm{s} = 2E$ is the energy per transmitted symbol and w_0 is the carrier frequency. To simplify the derivation, the carrier frequency w_0 is assumed much larger than $2\pi/T_\mathrm{s}$. We suppose that the two signals $s(t,\alpha_i)$ and $s(t,\alpha_j)$ differ over an interval N. The Euclidean distance between the two signals over the interval N is defined as [53]

$$\begin{aligned}&\int_0^{NT_\mathrm{s}} [s(t,\alpha_i) - s(t,\alpha_j)]^2 dt = \\ &\int_0^{NT_\mathrm{s}} s(t,\alpha_i)^2 dt + \int_0^{NT_\mathrm{s}} s(t,\alpha_j)^2 dt \\ &- 2\int_0^{NT_\mathrm{s}} s(t,\alpha_i)s(t,\alpha_j)\, dt.\end{aligned} \tag{A.2}$$

Since both signals are constant envelope with energy E over an interval T_s (we obtain E by integrating the square of (A.1) over an interval T_s), the second line of (A.2) can be

expressed as

$$\int_0^{NT_s} s(t,\alpha_i)^2 dt + \int_0^{NT_s} s(t,\alpha_j)^2 dt = 2NE. \tag{A.3}$$

Using the trigonometric function $\cos(a)\cos(b) = \frac{1}{2}(\cos(a-b) + cos(a+b))$ and assuming large carrier frequency, the third line in (A.2) can be presented as

$$\begin{aligned} &2\int_0^{NT_s} s(t,\alpha_i)s(t,\alpha_j)\ dt = \\ &2\frac{2E}{T_s}\int_0^{NT_s} \cos[w_0 t + \phi(t;\alpha_i)]\cos[w_0 t + \phi(t;\alpha_j)] = \\ &\frac{2E}{T_s}\int_0^{NT_s} \cos[\phi(t;\alpha_i) - \phi(t;\alpha_j)]dt. \end{aligned} \tag{A.4}$$

From (A.3) and (A.4), we can present (A.2) in the form

$$2NE - \frac{2E}{T_s}\int_0^{NT_s} \cos\Delta\phi(t)dt, \tag{A.5}$$

where $\Delta\phi(t)$ denotes the phase difference between the two signals. Here E is the energy obtained for an interval and not for a data bit. Therefore, for a fair comparison between many modulation schemes with different modulation levels M, E has to be normalized to obtain the energy per data bit E_b. The normalization of E is defined as

$$E = \log_2 M E_b. \tag{A.6}$$

Placing (A.5) and (A.6) in (1.24), we obtain (1.25).

Appendix for chapter 4: The detailed computation of the weights $w_{k,i}(m)$

This appendix presents the computation of the weights in (4.19) [40]. Let's introduce the autocorrelation of the PAM pseudo symbols $A_{k,i}(l) = E\left\{a_{k,n}a^*_{i,n+l}\right\}$, and $A_{k,i}(f)$ its spectrum, where the discrete fourier transform (DFT) of $A_{k,i}(f)$ is given by

$$A_{k,i}(f) = \sum_{l} A_{k,i}(l)e^{-j2\pi lfT}. \tag{B.1}$$

Now let's present $A(f)$ a matrix with a size $\mathcal{N} \times \mathcal{N}$, and $B(f)$ a matrix with a size $\mathcal{N} \times (N - \mathcal{N})$, where

$$\begin{aligned} &A(f) = \{A_{i,j}(f)\}, \quad 0 \le i, j \le \mathcal{N} - 1 \\ &B(f) = \{A_{i,j+\mathcal{N}}(f)\}, \ 0 \le i \le \mathcal{N} - 1, \ 0 \le j \le N - \mathcal{N} - 1. \end{aligned} \tag{B.2}$$

Next part presents the steps to obtain the weights. First we compute $C(f) = \{\mathcal{C}_{i,j}(f)\}$ a $\mathcal{N} \times (N - \mathcal{N})$ matrix which is given by

$$\mathbf{C}(f) = \mathbf{A^{-1}}(f) \times \mathbf{B}(f). \tag{B.3}$$

Second we compute the matrix $W(f) = \{\mathcal{W}_{i,j}(f)\}$ which it is related to $C(f)$ By

$$\begin{aligned} \mathcal{W}_{i,j}(f) &= \mathcal{C}_{i,j-\mathcal{N}}(f) \\ 0 \le i \le \mathcal{N} - 1, \quad &\mathcal{N} \le j \le N - 1. \end{aligned} \tag{B.4}$$

Finally, the weight $w_{k,i}(m)$ is computed using the inverse DFT of (B.4), i.e.

$$w_{k,i}(n) = T \int_{-1/2T}^{1/2T} \mathcal{W}_{k,i}(f) e^{j2\pi nfT} df. \tag{B.5}$$

Appendix C

Appendix for chapter 4: Equivalent bit error rate

In this appendix, we show that $s_1(t,\tilde{\alpha})$ and $s(t,\tilde{\alpha})$ have the same error probability performance using the union bound and the minimum Euclidean distance. First, let us show the union bound as presented in Section. 1.4.1 for any CPM signal

$$P_e \sim Q\left(\sqrt{d^2_{\min}\frac{E_b}{N_0}}\right), \tag{C.1}$$

To prove that the two signals $s_1(t,\tilde{\alpha})$ and $s(t,\tilde{\alpha})$ have the same error probability, we need to prove that they have the same minimum Euclidean distance d^2_{min}.

Based on Section. 1.4.1, the general form of the normalized squared Euclidean distance for any CPM signals is given as

$$d^2(\gamma) = \log_2 M\Big\{N - \frac{1}{T_\mathrm{s}}\int_0^{NT_\mathrm{s}} \cos[\phi(t,\gamma_N)]dt\Big\}. \tag{C.2}$$

Based on (C.2), it is proved that $s_1(t,\tilde{\alpha})$ and $s(t,\tilde{\alpha})$ have the same $d^2_{\min}$ if they have the same phase difference trajectories $\phi(t,\gamma_N)$. The phase difference trajectories for $s(t,\tilde{\alpha})$ is

$$\phi(t,\gamma) = 2\pi\tilde{h}\sum_i \gamma_i\phi_0(t-iT_\mathrm{s}), \tag{C.3}$$

where the difference sequence γ can take the values $\gamma = \{0,\pm 1\}$ (see equation (2.18)) for the binary case ($M=2$).
Similarly, the phase difference trajectories for $s_1(t,\tilde{\alpha})$ is

$$\tilde{\phi}(t,\tilde{\gamma}) = 2\pi h\sum_i \tilde{\gamma}_i\phi_0(t-iT_\mathrm{s}) \tag{C.4}$$

and the difference sequence $\tilde{\gamma}$ for binary case ($M=2$) can take the values $\tilde{\gamma} = \{0,\pm 2\}$

(see equation (1.26)).

As result, we could easily deduce that $\phi(t, \gamma)$ and $\tilde{\phi}(t, \tilde{\gamma})$ are equal. As we proved that the two modulations had the same phase difference trajectories, we showed that they had the same minimum normalized Euclidean distance $d^2_{\min}$, and consequently, the same error probability.

Appendix D

Appendix for chapter 4: Computing the pseudo symbols

D.1 Computing $\rho_{0,n}$ for 2SSB-FSK

Based on (4.7), we retrieve

$$\rho_{0,n} = \exp\left(j\pi h \sum_{m=0}^{n} \tilde{\alpha}_m\right) = \rho_{0,n-1} J^{\tilde{\alpha}_n} \tag{D.1}$$

where

$$J = e^{j\pi h}. \tag{D.2}$$

Since we have $h = 1/2$, we can replace $J^{\tilde{\alpha}_n}$ by $j\tilde{\alpha}_n$, and finally we obtain

$$\rho_{0,n} = \rho_{0,n-1} j\tilde{\alpha}_n. \tag{D.3}$$

$$\begin{aligned} p_{0,n} &\in \{1, -1\}, \quad n \text{ even} \\ p_{0,n} &\in \{j, -j\}, \quad n \text{ odd}. \end{aligned} \tag{D.4}$$

D.2 Computing $\rho_{1,n}$ for 2SSB-FSK

Similar to $\rho_{0,n}$, we have

$$\begin{aligned}\rho_{1,n} &= \exp\left(j\pi h \sum_{m=0}^{n} \tilde{\alpha}_m - \tilde{\alpha}_{n-1}\right) \\ &= \exp\left(j\pi h \sum_{m=0}^{n-2} \tilde{\alpha}_m + \tilde{\alpha}_n\right) \\ &= \rho_{0,n-2} J_n^{\tilde{\alpha}} \\ &= \rho_{0,n-2} j\tilde{\alpha}_n.\end{aligned} \tag{D.5}$$

$$\begin{aligned}p_{1,n} &\in \{j, -j\}, \quad n \text{ even} \\ p_{1,n} &\in \{1, -1\}, \quad n \text{ odd.}\end{aligned} \tag{D.6}$$

Appendix E

Appendix for chapter 4: Gaussian noise proof

This appendix presents the proof of $\tilde{n}(t)$ being a Gaussian noise.
Let's suppose that the time period T_s is unity, we can express the periodic term $s_2(t)$ in its exponential Fourier series c_n :

$$e^{-j\varphi(t)} = \sum_n c_n e^{jn2\pi t}, \tag{E.1}$$

where $\varphi(t) = 2\pi h \sum_i \phi_0 (t - iT_s)$, and c_n obey the the unitary relation $\sum_n c_n^* c_{n+k} = \delta_{k,0}$. The original AWG noise can be written as $\mathrm{n(t)} = \int_{-\infty}^{+\infty} df n(f) e^{j2\pi ft}$ where $n(f)$ is a Gaussian variable whose variance does not depend on frequency (white noise). The transformed noise $\tilde{n}(t) = n(t)e^{-j\varphi(t)}$ has therefore Fourier components:

$$\tilde{n}(f) = \sum_n c_n n(f - n). \tag{E.2}$$

Based on (E.2), $\tilde{n}(f)$ is a sum of independent Gaussian variables each multiplied by a deterministic term (c_n), this therefore a Gaussian variable. In addition, according to the unitary of c_n and as $< n(f)n(f - n) >= n(f)^2\delta_{n,0}$, the variance of $\tilde{n}(f)$ is frequency independent.
In conclusion the transformed noise $\tilde{n}(t)$ is arbitrary white noise with same intensity than the original noise.
Moreover, in Fig. E.1 we present the probability distribution of the received signal $r(t)(f_1(x))$ and $r_2(t)(f_2(x))$, where $r_2(t)$ is the received signal after extracting $s_2(t)$. We can observe that $f_1(x)$ and $f_2(x)$ are similar Gaussian distributions with zero mean. The simulation in Fig. E.1 was achieved using 10^5 information symbols.

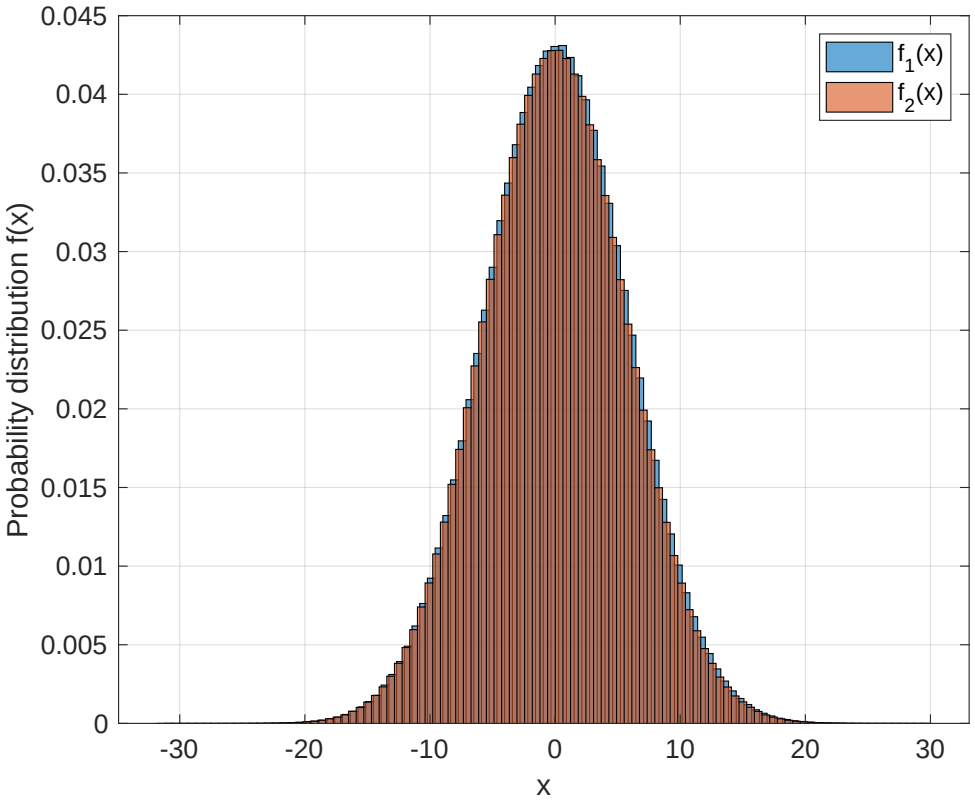

Figure E.1 – Probability distribution of the received signal $r(t)(f_1(x))$ and $r_2(t)(f_2(x))$.

Appendix F

Appendix for chapter 5: The development of the Fisher information matrix (FIM)

In this appendix we give the development of the FIM matrix. Based on (5.3), the FIM requires three partial derivatives:

$$\frac{\partial r(t,u,\alpha)}{\partial f_d} = j2\pi t\sqrt{\frac{E_s}{T_s}}e^{j(2\pi f_d t+\theta)}e^{j\phi(t-\epsilon;\alpha)} \tag{F.1a}$$

$$\frac{\partial r(t,u,\alpha)}{\partial \theta} = j\sqrt{\frac{E_s}{T_s}}e^{j(2\pi f_d t+\theta)}e^{j\phi(t-\epsilon;\alpha)} \tag{F.1b}$$

$$\frac{\partial r(t,u,\alpha)}{\partial \epsilon} = j\frac{\partial \phi(t-\epsilon;\alpha)}{\partial \epsilon}\sqrt{\frac{E_s}{T_s}}e^{j(2\pi f_d t+\theta)}e^{j\phi(t-\epsilon;\alpha)}. \tag{F.1c}$$

To obtain the FIM elements, we substitute the above equations and there conjugate in (5.3). Below, we gave the FIM elements:

$$I_{11} = \frac{8\pi^2 T_0^3}{3T_s}\left(\frac{E_s}{N_0}\right) \tag{F.2a}$$

$$I_{12} = I_{21} = \frac{2\pi T_0^2}{T_s}\left(\frac{E_s}{N_0}\right) \tag{F.2b}$$

$$I_{22} = \frac{2T_0}{T_s}\left(\frac{E_s}{N_0}\right) \tag{F.2c}$$

$$I_{13} = I_{31} = \frac{4\pi\left(\frac{E_s}{N_0}\right)}{T_s}\int_0^{T_0} t\frac{\partial \phi(t-\epsilon;\alpha)}{\partial \epsilon}dt \tag{F.2d}$$

$$I_{23} = I_{32} = \frac{2\left(\frac{E_s}{N_0}\right)}{T_s}\int_0^{T_0} \frac{\partial \phi(t-\epsilon;\alpha)}{\partial \epsilon}dt \tag{F.2e}$$

$$I_{33} = \frac{2\left(\frac{E_s}{N_0}\right)}{T_s}\int_0^{T_0} \left[\frac{\partial \phi(t-\epsilon;\boldsymbol{\alpha})}{\partial \epsilon}\right]^2 dt \tag{F.2f}$$

From the above equations, we notice that the FIM elements for the frequency offset and carrier phase, i.e. $I11$, $I12$, $I21$, $I22$, do not depend on either the training sequence or the SSB-FSK parameters [h, L, and $\phi_0(t)$]. Actually, they only depend on the signal to noise ration (SNR), the duration of the transmitted symbols T_0, and symbol duration. On the contrary, $I13$, $I31$, $I23$, $I32$, and $I33$, they depend on the SSB-FSK parameters, due to the presence of $\phi(t;\alpha)$.
The derivative of the SSB-FSK phase for the training sequence α and symbol timing ϵ is

$$\frac{\partial\phi(t-\epsilon;\alpha)}{\partial\epsilon} = -\sum_{i=0}^{L_0-1} 2\pi h\alpha_i g\left(t-iT_s-\epsilon\right). \tag{F.3}$$

Substituting (F.3) in (F.2d), (F.2e) and (F.2f), the five FIM elements related to the symbol timing become

$$I_{13}(u) = I_{31}(u) = -\frac{8\pi^2 h\left(\frac{E_s}{N_0}\right)}{T_s}\sum_{i=0}^{L_0-1}\alpha_i\int_0^{T_0} tg\left(t-iT_s-\epsilon\right)dt \tag{F.4a}$$

$$I_{23}(u) = I_{32}(u) = -\frac{4\pi h\left(\frac{E_s}{N_0}\right)}{T_s}\sum_{i=0}^{L_0-1}\alpha_i\int_0^{T_0} g\left(t-iT_s-\epsilon\right)dt \tag{F.4b}$$

$$I_{33}(u) = \frac{8\pi^2 h^2\left(\frac{E_s}{N_0}\right)}{T_s}\times\sum_{i=0}^{L_0-1}\sum_{j=0}^{L_0-1}\alpha_i\alpha_j\int_0^{T_0} g\left(t-iT_s-\epsilon\right)g\left(t-jT_s-\epsilon\right)dt. \tag{F.4c}$$

Finally, we can conclude the FIM as

$$I(u) = \frac{1}{T_s}\left(\frac{E_s}{N_0}\right)\begin{bmatrix} \frac{8\pi^2T_0^3}{3} & 2\pi T_0^2 & -8\pi^2\tilde{h}A \\ 2\pi T_0^2 & 2T_0 & -4\pi\tilde{h}B \\ -8\pi^2\tilde{h}A & -4\pi\tilde{h}B & 8\pi^2\tilde{h}^2C \end{bmatrix}. \tag{F.5}$$

BIBLIOGRAPHY

[1] John B Anderson, Tor Aulin, and Carl-Erik Sundberg, *Digital phase modulation*, Springer Science & Business Media, 2013.

[2] DARRELL L Ash, « A comparison between OOK/ASK and FSK modulation techniques for radio links », *in*: *RF Monothilics Inc, Dallas, TX, USA, Tech. Rep* (1992).

[3] T. Aulin and C. Sundberg, « An easy way to calculate power spectra for digital FM », *in*: *IEE Proceedings F - Communications, Radar and Signal Processing* 130.*6* (Oct. 1983), pp. 519–526, ISSN: 0143-7070, DOI: 10.1049/ip-f-1.1983.0082.

[4] Tor Aulin, Nils Rydbeck, and C-E Sundberg, « Continuous phase modulation-Part II: Partial response signaling », *in*: *IEEE Transactions on Communications* 29.*3* (1981), pp. 210–225.

[5] Alan Barbieri, Dario Fertonani, and Giulio Colavolpe, « Spectrally-efficient continuous phase modulations », *in*: *IEEE Transactions on Wireless Communications* 8.*3* (2009), pp. 1564–1572, DOI: 10.1109/TWC.2009.080679.

[6] *Bluetooth Core Specification*, Core Specification Working Group, 2019.

[7] David Bonacci, Raoul Prévost, Jean-Pierre Millerioux, Julia LeMaitre, M Coulon, and JY Tourneret, « Advanced concepts for satellite reception of AIS messages », *in*: *Proc. Toulouse Space Show* (2012), pp. 25–28.

[8] Enrico Casini, Dario Fertonani, and Giulio Colavolpe, « Advanced CPM receiver for the NATO tactical narrowband waveform », *in*: *2010 - MILCOM 2010 MILITARY COMMUNICATIONS CONFERENCE*, 2010, pp. 1725–1730, DOI: 10.1109/MILCOM.2010.5680230.

[9] Periklis Chatzimisios, Christos Verikoukis, Ignacio Santamaria, Massimiliano Laddomada, and Oliver Hoffmann, *Mobile Lightweight Wireless Systems: Second International ICST Conference, Mobilight 2010, May 10-12, 2010, Barcelona, Spain, Revised Selected Papers*, vol. 45, Springer, 2010.

[10] Jeonghoon Choi, Joon Ho Cho, and James S. Lehnert, « Continuous-Phase Modulation for DFT-Spread Localized OFDM », *in*: *IEEE Open Journal of the Communications Society* 2 (2021), pp. 1405–1418, DOI: 10.1109/OJCOMS.2021.3089690.

[11] Giulio Colavolpe, Guido Montorsi, and Amina Piemontese, « Spectral efficiency of linear and continuous phase modulations over nonlinear satellite channels », *in*: *2012 IEEE International Conference on Communications (ICC)*, 2012, pp. 3175–3179, DOI: 10.1109/ICC.2012.6363984.

[12] Robert C. Daniels and Robert W. Heath, « 60 GHz wireless communications: Emerging requirements and design recommendations », *in*: *IEEE Vehicular Technology Magazine* 2.*3* (2007), pp. 41–50, DOI: 10.1109/MVT.2008.915320.

[13] R Dorf, M Simon, L Milstein, Z Wan, L Milstein, and M Simon, *Digital Communications: Fundamentals and Applications*, 2013, ISBN: 9788131720929.

[14] J Dubois, T Jullien, F Portier, P Roche, A Cavanna, Y Jin, W Wegscheider, P Roulleau, and DC Glattli, « Minimal-excitation states for electron quantum optics using levitons », *in*: *Nature* 502.*7473* (2013), p. 659.

[15] ETSI, *3rd Generation Partnership Project; Technical Specification Group Radio Access Network; GSM/EDGE Modulation (Release 16)*, 2019.

[16] ETSI, *Digital Enhanced Cordless Telecommunication (DECT); Ultra low Energy (ULE); Machine to Machine Communications; Part 1: Home Automation Network (phase 1)*, 2013.

[17] ETSI, *Digital Video Broadcasting (DVB); Second Generation DVB Interactive Satellite System (DVB-RCS2); Part 2: Lower Layers for Satellite standard*, 2019.

[18] H. Farès, C. Glattli, Y. Louët, C. Moy, J. Palicot, and P. Roulleau, « New binary single side band CPM », *in*: *2017 24th International Conference on Telecommunications (ICT)* (May 2017), pp. 1–5, ISSN: null, DOI: 10.1109/ICT.2017.7998261.

[19] Haïfa Farès, D. Christian Glattli, Yves Louët, Jacques Palicot, Christophe Moy, and Preden Roulleau, « From quantum physics to digital communication: Single sideband continuous phase modulation », *in*: *Comptes Rendus Physique* 19.*1* (2018), pp. 54–63, ISSN: 1631-0705.

[20] Haifa Farès, D Christian Glattli, Yves Louet, Jacques Palicot, Preden Roulleau, and Christophe Moy, « Power Spectrum density of Single Side band CPM using Lorenztian frequency pulses », *in*: *IEEE Wireless Communications letters* 6.*6* (2017), pp. 786–789.

[21] US Air Force, *Interoperability and Performance Standards for Data Modems*, tech. rep., STD-188-110A, 1991.

[22] G. D. Forney, « The viterbi algorithm », *in*: *Proceedings of the IEEE* 61.*3* (Mar. 1973), pp. 268–278, ISSN: 1558-2256, DOI: 10.1109/PROC.1973.9030.

[23] D.C. Glattli and P. Roulleau, « patent WO2016124841 A1 », *in*: (2016).

[24] L Greenstein, « Spectra of PSK signals with overlapping baseband pulses », *in*: *IEEE Transactions on Communications* 25.*5* (1977), pp. 523–530.

[25] Trevor Hastie, Robert Tibshirani, and Jerome Friedman, *The elements of statistical learning: data mining, inference, and prediction*, Springer Science & Business Media, 2009.

[26] E. Hosseini and E. Perrins, « The Cramér-Rao bound for data-aided synchronization of SOQPSK », *in*: *MILCOM 2012 - 2012 IEEE Military Communications Conference*, 2012, pp. 1–6, DOI: 10.1109/MILCOM.2012.6415593.

[27] E. Hosseini and E. Perrins, « Timing, Carrier, and Frame Synchronization of Burst-Mode CPM », *in*: *IEEE Transactions on Communications* 61.*12* (2013), pp. 5125–5138, DOI: 10.1109/TCOMM.2013.111613.130667.

[28] Ehsan Hosseini and Erik Perrins, « The Cramer-Rao bound for training sequence design for burst-mode CPM », *in*: *IEEE Transactions on Communications* 61.*6* (2013), pp. 2396–2407.

[29] Ehsan Hosseini and Erik Perrins, « Training sequence design for data-aided synchronization of burst-mode CPM », *in*: *2012 IEEE Global Communications Conference (GLOBECOM)*, 2012, pp. 2234–2239, DOI: 10.1109/GLOCOM.2012.6503447.

[30] Xiaojing Huang and Yunxin Li, « The PAM decomposition of CPM signals with integer modulation index », *in*: *IEEE Transactions on Communications* 51.*4* (2003), pp. 543–546.

[31] T Jullien, P Roulleau, B Roche, A Cavanna, Y Jin, and DC Glattli, « Quantum tomography of an electron », *in*: *Nature* 514.*7524* (2014), p. 603.

[32] Ghassan Kawas Kaleh, « Simple Coherent Receivers for Partial Response Continuous Phase Modulation », *in*: *IEEE Journal on Selected Areas in Communications* 7.*9* (1989), pp. 1427–1436, ISSN: 07338716, DOI: 10.1109/49.44586.

[33] Karim Kassan, Haïfa Farès, D. Christian Glattli, and Yves Louët, « Performance vs. Spectral Properties for Single-Sideband Continuous Phase Modulation », *in*: *IEEE Transactions on Communications* 69.*7* (2021), pp. 4402–4416, DOI: 10.1109/TCOMM.2021.3073792.

[34] Karim Kassan, Haïfa Farès, D. Christian Glattli, and Yves Louët, « Simplified Receivers for Generic Binary Single Side Band CPM Using PAM Decomposition », *in*: *IEEE Access* 9 (2021), pp. 115962–115971.

[35] Pierre Laurent, « Exact and approximate construction of digital phase modulations by superposition of amplitude modulated pulses (AMP) », *in*: *IEEE Transactions on Communications* 34.*2* (1986), pp. 150–160.

[36] Leonid S Levitov, Hyunwoo Lee, and Gordey B Lesovik, « Electron counting statistics and coherent states of electric current », *in*: *Journal of Mathematical Physics* 37.*10* (1996), pp. 4845–4866.

[37] Mouna Ben Mabrouk, Marwa Chafii, Yves Louet, and Faouzi Bader, « A precoding-based PAPR reduction technique for UF-OFDM and filtered-OFDM modulations in 5G systems », *in*: *European Wireless 2017; 23th European Wireless Conference*, VDE, 2017, pp. 1–6.

[38] R Timothy Marler and Jasbir S Arora, « Survey of multi-objective optimization methods for engineering », *in*: *Structural and multidisciplinary optimization* 26.*6* (2004), pp. 369–395.

[39] Umberto Mengali, *Synchronization techniques for digital receivers*, Springer Science & Business Media, 2013.

[40] Umberto Mengali and Michele Morelli, « Decomposition of M-ary CPM signals into PAM waveforms », *in*: *IEEE Transactions on information theory* 41.*5* (1995), pp. 1265–1275.

[41] Malek Messai, « Application des signaux CPM pour la collecte de données à grande échelle provenant d'émetteurs faible cout », PhD thesis, Télécom Bretagne; Université de Bretagne Occidentale, 2015.

[42] Malek Messai, Karine Amis, and Frédéric Guilloud, « On the Optimization of a PSP-Based CPM Detection », *in*: *IEEE Transactions on Wireless Communications* 15.*3* (2016), pp. 2144–2154, ISSN: 15361276, DOI: 10.1109/TWC.2015.2498932.

[43] Melanie Mitchell, *An introduction to genetic algorithms*, MIT press, 1998.

[44] *Modulation (GSM 05.04) Digital Cellular Telecommunications System.* ETSI standard ETS 300959, 1998.

[45] P. Ngatchou, A. Zarei, and A. El-Sharkawi, « Pareto Multi Objective Optimization », *in*: *Proceedings of the 13th International Conference on, Intelligent Systems Application to Power Systems* (Nov. 2005), pp. 84–91, ISSN: null, DOI: 10.1109/ISAP.2005.1599245.

[46] Alan V Oppenheim, Alan S Willsky, and S Hamid, *Signals and systems, Processing series*, 1997.

[47] R. Othman, A. Skrzypczak, and Y. Louët, « PAM Decomposition of Ternary CPM With Duobinary Encoding », *in*: *IEEE Transactions on Communications* 65.*10* (2017), pp. 4274–4284.

[48] Rami Othman, « Study of reception techniques for aeronautical telemetry modulations », PhD thesis, CentraleSupélec, 2019.

[49] E. Perrins and M. Rice, « PAM decomposition of M-ary multi-h CPM », *in*: *IEEE Transactions on Communications* 53.*12* (2005), pp. 2065–2075.

[50] E. Perrins and M. Rice, « PAM representation of ternary CPM », *in*: *IEEE Transactions on Communications* 56.*12* (2008), pp. 2020–2024.

[51] Erik Samuel Perrins, « Reduced Complexity Detection Methods for Continuous Phase Modulation », *in*: (2005).

[52] Erik Perrins, Michael Rice, and Senior Member, « A New Performance Bound for PAM-Based CPM Detectors », *in*: 53.*10* (2005), pp. 1688–1696.

[53] John G Proakis and Masoud Salehi, *Digital communications*, vol. 4, McGraw-hill New York, 2008.

[54] Anchalee Puengnim, Nathalie Thomas, Jean-Yves Tourneret, and Josep Vidal, « Classification of linear and non-linear modulations using the Baum–Welch algorithm and MCMC methods », *in*: *Signal processing* 90.*12* (2010), pp. 3242–3255.

[55] B.E. Rimoldi, « A decomposition approach to CPM », *in*: *IEEE Transactions on Information Theory* 34.*2* (1988), pp. 260–270, DOI: 10.1109/18.2634.

[56] A. Svensson, C. Sundberg, and T. Aulin, « A Class of Reduced-Complexity Viterbi Detectors for Partial Response Continuous Phase Modulation », *in*: *IEEE Transactions on Communications* 32.*10* (1984), pp. 1079–1087.

[57] Afzal Syed, « Comparison of Noncoherent detectors for SOQPSK and GMSK in Phase Noise Channels », *in*: International Foundation for Telemetering, 2007.

[58] Range Commanders Council Telemetry Group, *Telemetry Standards, IRIG Standard 106-13 (Part 1)*, Secretariat, Range Commanders Council, White Sands Missile Range, New Mexico, 88002, 2013.

[59] Mason Wardle and Michael Rice, « PAM approach to weak CPM and its application to flight termination receivers », *in*: *IEEE Transactions on Aerospace and Electronic Systems* 44.*2* (2008), pp. 468–480, ISSN: 00189251, DOI: 10.1109/TAES.2008.4560200.

[60] M. P. Wylie-green, « A New PAM Decomposition for Continuous Phase Modulation », *in*: *2006 40th Annual Conference on Information Sciences and Systems*, 2006, pp. 705–710.

[61] Zhengguang Xu and Qifeng Wang, « Autocorrelation Function of Full-Response CPM Signals and Its Application to Synchronization », *in*: *IEEE Access* 7 (2019), pp. 133781–133786, ISSN: 21693536, DOI: 10.1109/ACCESS.2019.2941775.

[62] Richard Hsin Hsyong Yang, Chia Kun Lee, and Shiunn Jang Chern, « Continuous phase modulation (CPM) revisited: Using time-Limited phase shaping pulses », *in*: *IEICE Transactions on Communications* E96-B.*11* (2013), pp. 2828–2839, ISSN: 17451345, DOI: 10.1587/transcom.E96.B.2828.

DOCTORAT BRETAGNE LOIRE / MATHSTIC

CentraleSupélec

Titre : Performances d'une nouvelle modulation à phase continue (CPM) à bande latérale unique (SSB)

Mot clés : Modulation en phase continue (CPM), détection de séquence à maximum de vraisemblance, bande latérale unique (BLU), décomposition de Laurent, récepteur à complexité réduite, bornes de Cramér-Rao.

Résumé : Dans cette thèse, nous étudions la modulation par déplacement de fréquence à bande latérale unique (SSB-FSK), un schéma de modulation de phase continue (CPM) ayant, par essence, la caractéristique original du spectre à bande latérale unique (BLU). Tout d'abord, nous présentons l'origine du signal à partir de la physique quantique. Ensuite, nous proposons un détecteur de séquence à maximum de vraisemblance (MLSD) simplifié pour les schémas CPM conventionnels, basé sur le réarrangement montré dans le modèle de signal SSB-FSK. Pour exploiter pleinement les performances de la SSB-FSK, nous examinons la probabilité d'erreur du signal, l'occupation de la bande passante et la complexité du récepteur. Étant donné que différentes mesures de performance sont prises en compte, nous avons utilisé une optimisation multi-objectifs pour obtenir de nouveaux schémas SSB-FSK plus performants que les schémas CPM classiques. En outre, nous proposons une solution pour simplifier la complexité des signaux SSB-FSK en utilisant la décomposition de la modulation d'amplitude d'impulsion (PAM). Les impulsions PAM ont été obtenues à partir d'un algorithme que nous avons développé. En outre, nous proposons une séquence d'entraînement générique optimale pour l'estimation conjointe de la synchronisation des symboles, du décalage de fréquence et de la phase de la porteuse pour la synchronisation en mode burst. La séquence d'entraînement a été obtenue en utilisant les bornes de Cramér-Rao.

Title: Performance of a new single sideband (SSB) continuous phase modulation (CPM)

Keywords: Continuous phase modulation (CPM), maximum likelihood sequence detection (MLSD), single-sideband (SSB), Laurent decomposition, reduced-complexity receiver, Cramér-Rao bounds.

Abstract: In this PhD thesis, we investigate the single-sideband frequency shift keying (SSB-FSK), a continuous phase modulation (CPM) scheme having, by essence, the original feature of the single-sideband (SSB) spectrum. First, we present the origin of the signal from quantum physics. Then, we propose a simplified Maximum likelihood sequence detection (MLSD) detector for conventional CPM schemes based on the rearrangement shown in the SSB-FSK signal model. To fully exploit the SSB-FSK performance, we examine the signal error probability, bandwidth occupancy, and receiver complexity. Since different performance metrics are considered, we employed a multi-objective optimization to achieve new SSB-FSK schemes that outperform conventional CPM schemes. Moreover, we propose a solution to simplify the complexity of SSB-FSK signals using the pulse amplitude modulation (PAM) decomposition. The PAM pulses were achieved from an algorithm we developed. Furthermore, we offer an optimum generic training sequence for the joint estimation of symbol timing, frequency offset, and carrier phase for burst mode synchronization. The training sequence was obtained using the Cramér-Rao bounds.